

Capillary stamping for bioanalytics and spatial manipulation of protein-protein interactions in live cells

Dissertation

By Michael Philippi

Institute of Chemistry of New Materials and

Center of Cellular Nanoanalytics

Osnabrück

2021

Dissertation to partially fulfill the requirements for the degree of

‘Doctor rerum naturalium’

presented by Michael Philippi

to the Institute of Chemistry of New Materials and Center of Cellular Nanoanalytics
(CellNanOs) - University of Osnabrück

Reviewer #1: Prof. Dr. Martin Steinhart

Reviewer #2: Prof. Dr. Jacob Piehler

Acknowledgments

First and foremost, I would like to thank **Prof. Dr. Martin Steinhart** for the opportunity to join the project, the continuous support and especially for the help with the thesis.

I would also like to thank **Dr. Changjiang You** for his assistance, discussions and basically a complete introduction into the biochemical field.

Many thanks to **Prof. Dr. Jacob Piehler** for his support and the examination of my doctoral thesis.

I wish to thank **Prof. Dr. Andreas Hennig** and **Dr. Rainer Kurre** for being part of the examination board.

I would like to thank **Claudia Heß** and **Christine Schulz-Kölbel** for having a solution for most problems that came up in the lab, as well as **Barbara Gunkel** for her help, especially with administrative issues.

Because doing science alone is no fun, a big thanks to all my colleagues who helped me out with their knowledge or kept me entertained during tedious times; this is true for my former and present coworkers in the physical chemistry department and for the people in biophysics. My special gratitude to **Ruža Periz**, **Qaiser Ali Khan**, **Fernando Vázquez-Luna**, **Dr. Mercedes Runge**, **Jonas Klein**, **Marie Kappen** and **Dr. Michael Holtmannspötter**.

A thank you to the first colonists of the CellNanOs, which made the place habitable and a very nice and enjoyable working place. A special thanks to **Wladislaw Kohl**, who still does not want to share his formula for successful cell transfections but is otherwise very helpful in anything regarding practical biological work.

Many thanks to my colleague **Mykola Fomin** from the physics department for his nonstop sample preparation and **Lara Jorde** for her help with the graphene/TIRF-RfS experiments.

I would like to thank my collaboration partners **Christian P. Richter** for the MATLAB data analysis program, **Jannis Thien** and **Prof. Dr. Joachim Wollschläger** for the XPS expertise and **Dr. Domenik Liße** for providing reagents.

Last but not least, I want to thank my brother **Marco** for his help with my MATLAB problems and my parents **Bernd** and **Ulrike**, for their continuous, unconditional support.

Table of Contents

| | | |
|----------|--|-----------|
| 1 | Introduction | 1 |
| 2 | State of the Art | 3 |
| 2.1 | Patterning techniques for direct material transfer | 3 |
| 2.1.1 | Serial methods | 3 |
| 2.1.2 | Parallel methods | 6 |
| 2.2 | Patterned substrates for bioanalytics | 12 |
| 2.3 | Wnt signaling pathway | 15 |
| 2.4 | Optogenetics | 18 |
| 3 | Experimental | 20 |
| 3.1 | Materials | 20 |
| 3.2 | Characterization | 21 |
| 3.2.1 | Atomic force microscopy | 21 |
| 3.2.2 | Scanning electron microscopy | 21 |
| 3.2.3 | Water contact angle measurements..... | 21 |
| 3.2.4 | X-ray photoelectron spectroscopy | 22 |
| 3.2.5 | Total internal reflection fluorescence microscopy | 22 |
| 3.2.6 | Image analysis | 23 |
| 3.2.7 | Total internal reflection fluorescence - Reflectance interference spectroscopy | 24 |
| 3.2.8 | Matrix-assisted laser desorption/ionization | 24 |
| 3.2.9 | Ultraviolet-visible spectroscopy | 25 |
| 3.3 | Preparation and functionalization | 25 |
| 3.3.1 | Modification of glass substrates | 25 |
| 3.3.2 | Stamp synthesis of mesoporous silica stamps | 25 |
| 3.3.3 | Synthesis of functionalized bovine serum albumin | 26 |
| 3.3.4 | Dye functionalization of BSA | 26 |
| 3.3.5 | HaloTag-Ligand functionalization of BSA | 26 |
| 3.4 | Capillary stamping..... | 26 |

| | | |
|----------|---|-----------|
| 3.4.1 | Pre-stamping preparations of porous silica stamps..... | 26 |
| 3.4.2 | Heterocyclic silanes..... | 28 |
| 3.4.3 | Streptavidin-cyanine 5 | 28 |
| 3.4.4 | BSA-ATTO 647N..... | 28 |
| 3.4.5 | BSA-HTL..... | 29 |
| 3.4.6 | Poly(L-lysine)-poly(ethylene glycol)-biotin (PLL-PEG-bt) | 29 |
| 3.5 | Post-stamping treatments | 29 |
| 3.5.1 | Fluorescent labeling of heterocyclic silane patterns..... | 29 |
| 3.5.2 | Synthesis of PS brushes on cycloazasilane patterns | 29 |
| 3.5.3 | End-chain functionalization of PS brush | 30 |
| 3.5.4 | Immobilization of HaloTag-mEGFP protein on cycloazasilane patterns..... | 30 |
| 3.5.5 | HaloTag-dDARPin functionalization of BSA-HTL patterns..... | 30 |
| 3.5.6 | Fluorescent labeling of BSA-HTL/BSA-HTL-dDARPin patterns | 30 |
| 3.5.7 | Fluorescent labeling of PLL-PEG-bt | 31 |
| 3.6 | Cell culturing | 31 |
| 3.6.1 | Transformation..... | 31 |
| 3.6.2 | Transfection | 31 |
| 3.6.3 | Cell experiments..... | 32 |
| 3.6.4 | Protein labeling | 33 |
| 3.6.5 | Fixation..... | 33 |
| 3.6.6 | Immunostaining | 34 |
| 4 | Results and discussion..... | 35 |
| 4.1 | Substrate design – stamping of heterocyclic silanes and synthetic polymers..... | 35 |
| 4.1.1 | Stamping of heterocyclic silanes..... | 35 |
| 4.1.2 | Polystyrene brushes by surface-initiated polymerization | 42 |
| 4.1.3 | Biofunctionalization of cycloazasilane dot arrays with HaloTag-ligand..... | 44 |
| 4.1.4 | Stamping of biotinylated Poly-L-Lysine..... | 47 |
| 4.2 | Substrate design – stamping of proteins | 48 |

| | | |
|----------|---|-----------|
| 4.2.1 | Stamping of labeled streptavidin | 48 |
| 4.2.2 | Stamping and modification of BSA-HTL | 50 |
| 4.2.3 | Modification of BSA-HTL patterns with Designed Ankyrin Repeat Proteins..... | 60 |
| 4.2.4 | Stamping of BSA-HTL on graphene | 61 |
| 4.3 | Comparison of stamped dot arrays..... | 63 |
| 4.4 | Cellular interactions – proof of principle | 65 |
| 4.4.1 | Reorganization of membrane associated IFNAR2-receptor | 65 |
| 4.4.2 | Live-cell analysis of dDARPin modified HTL-BSA dot arrays..... | 68 |
| 4.4.3 | Protein binding on BSA-HTL-dDARPin patterns manipulated by optogenetics .. | 69 |
| 4.4.4 | Reorganization of signaling proteins complexes in the Wnt signaling pathway | 72 |
| 5 | Conclusion and outlook | 82 |
| 6 | References..... | 85 |
| 7 | Appendix..... | 93 |
| 7.1 | List of abbreviations | 93 |
| 7.2 | Publication list..... | 96 |
| 7.3 | <i>Curriculum vitae</i> | 97 |
| 7.4 | Declaration | 98 |

1 Introduction

Miniaturization of systems or components is a widespread general approach to increase efficiency in their application. In the field of electronics, Moore's law predicted that the number of transistors on a microchip doubles every two years^[1]; the prediction prevailed by continuously decreasing the featured transistor sizes. Similarly, efforts are made to shrink mechanical and optical parts for displays^[2], sensors^[3] and data storage systems^[4].

Micro/nanoscale features can be fabricated by top-down or bottom-up techniques^[5]. The more common and widely used top-down techniques include soft lithography^[6], photolithography^[7] or focused ion beam lithography^[8]. Since each method has its advantages and disadvantages, techniques are combined or further developed to match the benchmarks necessary for the desired application.

Soft lithography with poly(dimethoxysiloxane) (PDMS) stamps developed by Whitesides *et al.* in the nineties^[6] is used extensively in small scale laboratory experiments because of its easy handling and fabrication as well as a wide range of stampable molecules ranging from particles to DNA, proteins and silanes^[9]. Therefore, many adjustments were made to accommodate the drawbacks involving this method. Stamp surface functionalizations were introduced to increase the range of applicable inks (*e.g.*, oxygen plasma treatment^[10], PEGylation^[11]) and stamp reinforcement strategies by developing PDMS composite^[12] alternative stamp materials^[13] were employed. These strategies were mainly used to decrease the sizes which could be stamped. With the introduction of polymer pen lithography, Mirkin *et al.*^[14] combined microcontact printing (μ CP) with a serial lithography method (*e.g.*, dip-pen lithography^[15]) to gain better control over the spatial resolution and decrease the featured sizes below the 1 μ m mark. In 2018 Schmidt *et al.* developed capillary stamping with spongy mesoporous silica stamps^[16], which features a contiguous pore network. This method was compatible with various inks (particulate and molecular) notably based on organic solvents. However, the main advantage is the continuous pore network which allows ink supply during the stamping operations.

In this work, possible applications for capillary stamping will be explored further. The stamping method allows consecutive stamping cycles due to its porous stamp material, which acts as an ink reservoir and is compatible with a wide variety of inks, particulate and molecular. The feature dot array produced by capillary stamping lies in the few hundred-nanometer range and is combined with a nearest neighbor distance of $\approx 1.3 \mu$ m between each stamped dot (see Figure 1a). These length characteristics match the length scales of biomolecular organizations on living cells very well and are far enough apart to comfortably utilize standard diffraction-limited

microscopy. Depending on the type of patterned molecules, the dots will be used as initiation sites for further modifications or directly used as biorthogonal interaction partners for proteins of interest. The goal, therefore, will be to create a feasible platform for investigations of different types of protein-protein interactions by spatially controlling their involved biomolecules at the protein surface.

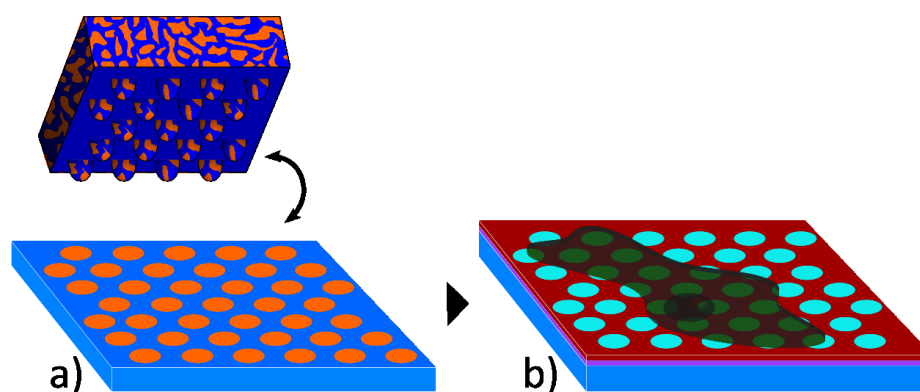


Figure 1: Illustration of capillary stamping and spatial reorganization of cell membrane receptors. a) depiction of infiltrated mesoporous silica stamp with a patterned surface. b) typical cell experiment with adapted pattern by membrane receptor.

In the first part of this work, different types of ink with functional molecules will be printed onto a glass surface and assessed toward their capability to enable an analysis of cellular interactions. Among the evaluated patterned surfaces are dot arrays generated with heterocyclic silanes, which react in a ring-opening reaction upon contact with hydroxyl-terminated surfaces^[17] and allow post-modifications of the stamped dot array. Similarly, functionalized proteins (*e.g.*, BSA-HTL) will be stamped from an aqueous solution and analyzed in regards to specific geometric descriptors and overall contrast between dot and background.

After the establishment of a robust patterning system by capillary stamping, the stamped substrates will be tested in a biologically inspired application. First, with the introduction of optogenetics, namely the photoactivatable iLID-system into HeLa cells, protein recruitment from the cytosol to the membrane-bound domains upon irradiation with light will be investigated. Second, the protein dot arrays will be used to investigate the canonical Wnt-signaling pathway. Therefore, the four involved proteins (Lrp6, Axin1, Dvl2, Fzd8) will be expressed in HeLa cells and studied for their ability to be co-recruited to the patterns. β -Catenin levels are measured *via* immunostaining with a primary dye-labeled antibody under different conditions to prove that the accumulated protein receptor concentrations are sufficient to activate the signaling pathway.

2 State of the Art

2.1 Patterning techniques for direct material transfer

Over the time several lithographic methods were established and proved to be an excellent way for surface patterning. Therefore, an abundance of techniques was developed and refined to match the desired requirements. One can choose from serial or parallel, mask-based or maskless techniques, each with its own advantages and disadvantages. Photolithography, a stable in the semiconductor industry, electron-beam lithography and nanoimprint lithography are just a few examples of different techniques widely used. Since this work focused on capillary stamping, a parallel maskless lithography method with a direct material transfer, in regards to a biological application, similar techniques are discussed in more detail in the following chapter.

2.1.1 Serial methods

Serial methods generate patterns pixel by pixel and stand in contrast to the parallel techniques, which creates a large number of features at the same time. Due to this fact, serial methods usually display a higher precision and smaller featured sizes without the need for masks or pre-formed structures. However, the processing time to pattern large-scale areas is longer and more complex machinery is necessary to run these methods. Focused ion beam (FIB) lithography^[18] or electron-beam lithography^[19] are good examples of such a technique; they are used to create structures and do not inherently transfer material to a surface. Dip-pen nanolithography (DPN), developed by Mirkin^[15] *et al.* in 1999, on the other hand, uses an atomic force microscope (AFM) cantilever to transfer adsorbed molecules onto a surface in a writing manner. In the publication, thiols were written onto a gold substrate, but the range of inks has increased a lot since then. DPN is used to create arrays in the nanometer regime with

deoxyribonucleic acid (DNA), proteins, lipids, viruses and bacteria as suitable biomolecules for patterning^[20]. In Figure 2, the writing process is displayed as a simple schematic.

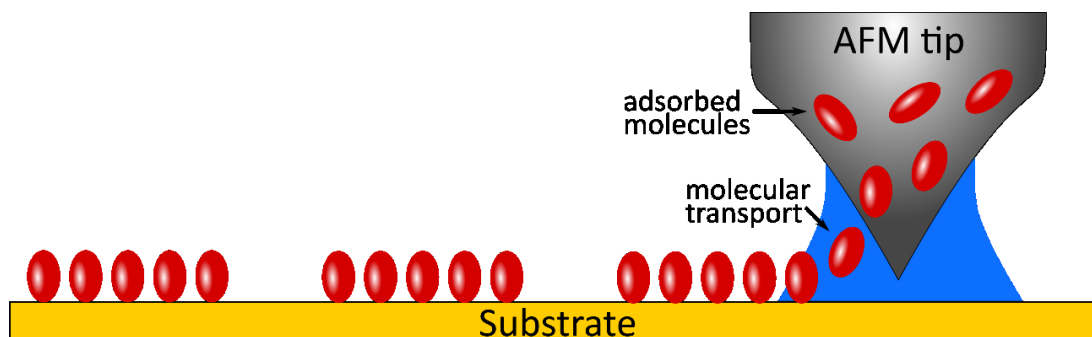


Figure 2: Illustration of DPN patterning process. Deposition of adsorbed molecules (red) on an AFM tip through a liquid bridge when contacting the surface. Illustration adapted from Piner *et al.*^[15].

It should also be noted that several variants of DPN were developed soon after, each using the AFM tip as a transmitter for a different force. Li^[21] *et al.* combined it with an electrochemical component for electrochemical deposition, Sheehan^[22] *et al.* utilized a heated AFM tip to melt octadecylphosphonic acid to subsequently pattern the surface and Liu^[23] *et al.* used the AFM cantilever to apply high shear forces on self-assembled monolayers. Although these variations made DPN more viable for a broader range of applications, the main drawback of a low-throughput method still remained. Large area cantilever arrays were utilized to solve this issue^[24] but did not prove feasible due to tedious alignment procedures and fragile tip arrays.

Other additive serial methods are inkjet printing (IJP) and aerosol jet printing (AJP). IJP utilizes small ink droplets which are deposited on the desired surface, while AJP atomizes the ink and redirects the ink aerosol onto the target surface^[25]. The most common ways to generate droplets for IJP are thermal and piezoelectric^[26]. The thermal approach heats up a resistive element in the ink dispensing unit, which vaporizes a small part of the ink and therefore creates pressure by the expansion of the gas phase ink. To offset the increase in pressure, a droplet is ejected

through the nozzle (Figure 3a). Similarly, the piezoelectric method creates pressure by squeezing the dispensing unit with a piezo element (Figure 3b).

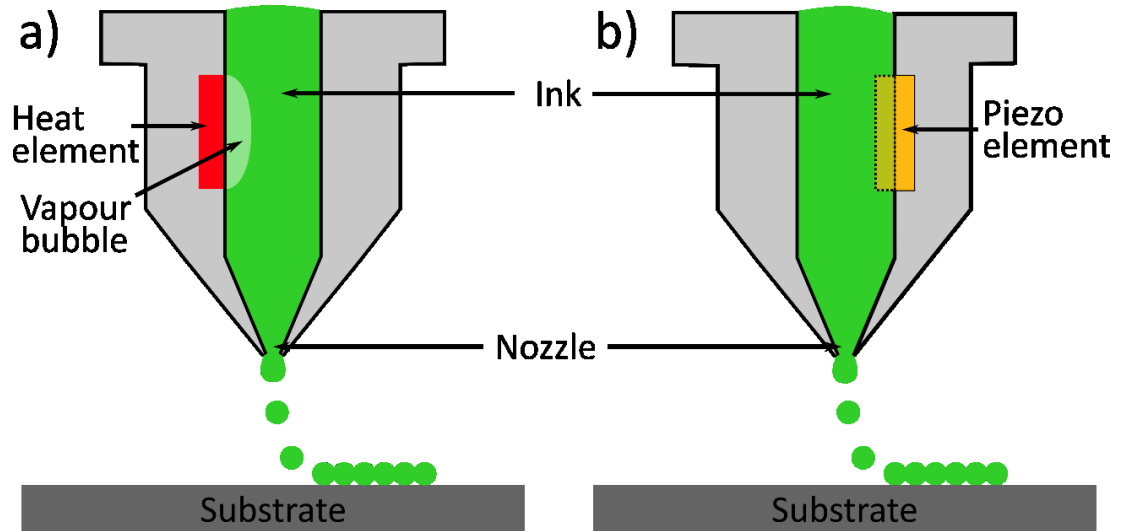


Figure 3: Schematic illustration of different inkjet printing systems. a) Thermal IJP. A heating element generates a vapor bubble inside the dispensing unit, and due to the generated pressure, ink drops are ejected through the nozzle. b) Piezoelectric IJP. The necessary force is generated by the mechanical actuation of the piezo element.

IJP generally is a very versatile technology able to print a large variety of different inks on suitable surfaces. Therefore it is not surprising that it has seen applications in the field of electronics^[27], sensor array fabrication^[28], tissue engineering^[29], chemistry^[30] and biology^[31]. Overall the technique is considered a low-cost, high-efficiency method for patterning large areas without the need for an additional mask and with a lot of flexibility in terms of inks and substrates^[32]. The resolution of the printed features is rather large at $\approx 12 \mu\text{m}$ without the aid of additional substrate modifications^[26]. The resolution was improved with the development of electrohydrodynamic printing^[33] but remains challenging. In recent years inkjet printing of 3D structures gained a lot of attraction^[34,35].

2.1.2 Parallel methods

2.1.2.1 Microcontact printing (μ CP)

μ CP is a parallel stamping technique designed to pattern large areas in one stamping cycle. It was developed by Whitesides *et al.* in the nineties^[6] and is used extensively in small-scale laboratory experiments.

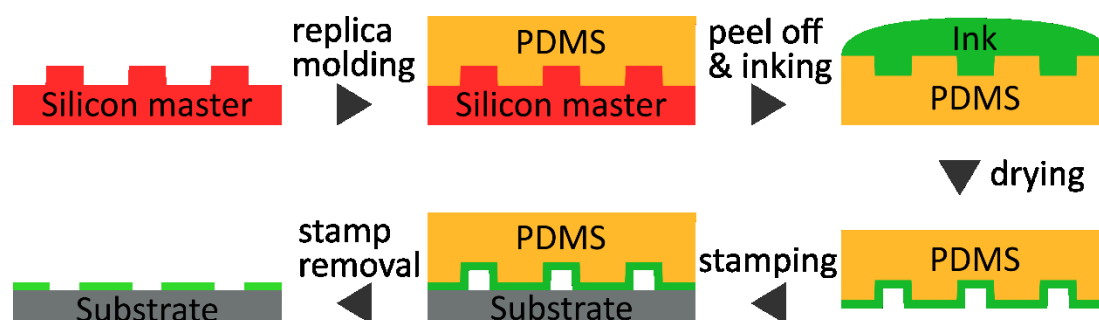


Figure 4: Illustration of a general μ CP procedure. A PDMS stamp is made by replica molding against a silicon master and inked. The dried stamp is then brought into contact with a substrate, thus patterning it.

In Figure 4, a general μ CP process with stamp fabrication is sketched. A PDMS pre-polymer is mixed with a curing agent and poured on top of a structured silicon master substrate. After curing, the flexible stamp is peeled off and the ink is added to the structured side. Subsequently, the excess ink is removed and the stamp is dried, usually in an air or nitrogen stream. The inked stamp is brought into contact with the substrate and the desired molecule is transferred to the substrate but only at the protruding contact elements of the stamp^[36]. A major strength of μ CP is the wide range of molecules, proteins and particles, which can be patterned with little or no modification to the stamp material. Kumar and Whitesides utilized alkythiols in ethanol or diethyl ether to print on gold surfaces due to the known formation of self-assembled monolayers (SAM) of thiols on gold^[37]. Particles^[38], polymers^[39] and molecules bearing functional groups for subsequent modification^[40] could all be patterned onto various substrates, *e.g.*, glass, gold or polystyrene. The hydrophobic surface of PDMS limits its use in combination with polar solvents like water and solutions like oxygen plasma treatment^[10], which turn the surface hydrophilic, reduce the overall re-usability of the stamp^[41]. It does, however, enable patterning from polar solvents and additional modifications with poly(ethylene glycol) (PEG) chains^[11] diminished the drawback. Consequently, DNA^[42], antibodies^[43] and proteins^[44] could be patterned on the desired surface and enabled investigations into a variety of different biomolecular/chemical questions. However, classical μ CP with PDMS stamps is prone to collapse and sagging of the stamp when patterning features fall below a specific aspect ratio of the contact elements^[45].

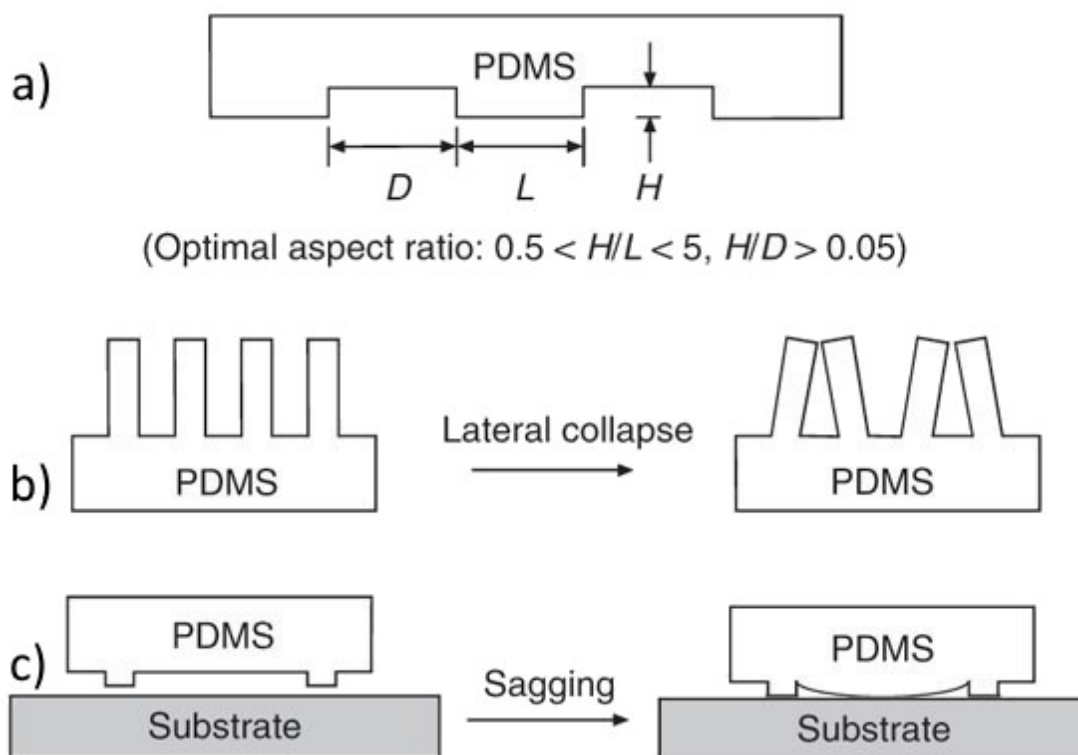


Figure 5: Schematic of the optimal aspect ratio for standard PDMS stamps and modes of failure. a) Optimal aspect ratio depending on the height and length of the contact elements and the distance in between each of them. b) Lateral collapse of the contact elements when the ratio between H/L exceeds >5 . c) Sagging of recessed structures with aspect ratios < 0.5 . Schematic taken from Qin *et al.*^[45].

To receive optimal stamping results, an aspect ratio of 0.5-5 between the height (H) and the length (L) of the contact elements should be kept in combination with a ratio of less than 0.05 between the distance (D) of two contact elements and H (Figure 5a). If the ratio H/L exceeds > 5 , the structure is prone to lateral collapse during stamping (Figure 5b) and for ratios < 0.5 , sagging of the bulk PDMS stamp occurs (Figure 5c). To overcome this problem, several improvements and adaptations to the stamp were developed. With a hard PDMS layer for the contact elements and a softer backing layer, sizes down to 80 nm could be achieved^[46]. Likewise, changing the material from PDMS to polyolefins^[47] or poly(urethane acrylate)^[48] helped to scale down feature sizes.

2.1.2.2 Polymer pen lithography

Polymer pen lithography (PPL) developed in 2008^[14] tries to overcome the drawbacks of DPN by replacing the fragile AFM cantilevers with soft PDMS tip arrays. PDMS is cast onto a patterned silicon wafer similar to μ CP and features arrays of pyramidal structures (Figure 6). The array is reinforced with a glass slide as a backing layer and the approach to a surface is monitored by an optical microscope through the glass and the stamp. When the tip array contacts the surface, the reflectance of light from the tips changes drastically, making leveling procedures possible.

Since good alignment is crucial for large area patterning up to the cm^2 scale, several improvements were made to address this problem^[49,50].

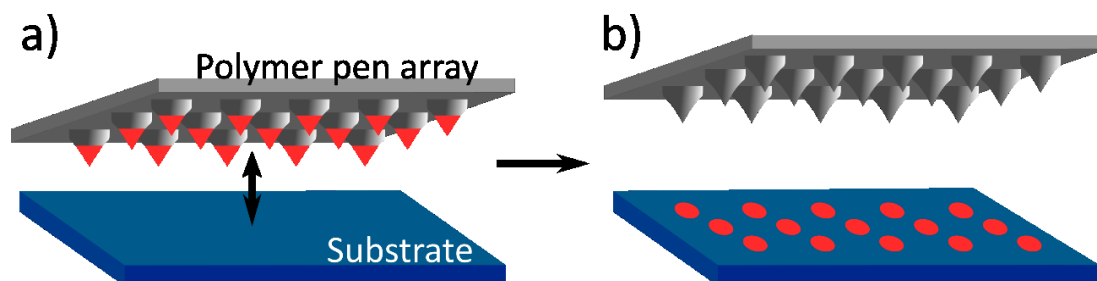


Figure 6: Schematic illustration of PPL. a) An inked elastomeric tip array is brought into contact with a substrate. b) Deposition of adsorbed molecules onto the surface.

With these advancements, more machinery was required to be added to an already heavily automated system. Organic solvents mixed with a functional component constitute a printable ink. Water, however, cannot be used as the sole solvent component for the ink and stamping is only possible under defined atmospheric conditions to prevent the stamps from drying out. After a few printing cycles, the adsorbed ink runs out, the tips have to be re-inked and the stamp must be re-aligned, which makes continuous patterning a tedious process^[51]. The achievable dot size can range from 90 nm to 10 μm and is controlled by the pressure applied during the stamping procedure. A higher force results in bigger spots because of the deformation of the flexible PDMS tips. Although this concept brings a lot of flexibility to the technique, controlling the spot size is difficult and often requires a series of testing procedures. Compared to DPN, patterns in the nanometer regime are not as robust and not as easily reproducible with conventional PPL. Therefore, analog to μCP , several methods were developed to reinforce the stamp material. In 2012 dual-elastomer tips were introduced, which consisted of a harder elastomer for the tips and a softer elastomer as a backing layer^[52]. During stamping, the soft layer acts as a cushion and prevents deformation of the hard stamp tips. This adaptation not only helps with the alignment but also increases precision. Other materials for stamp preparation have been explored as well, Zhong and colleagues tested poly(methyl methacrylate), poly([methyl methacrylate]-co[butyl methacrylate]) and poly(3-mercaptopropylmethylsiloxane) for their suitability^[53]. Hendrick *et al.* coated PDMS tip arrays with a ≈ 175 nm thick silica layer^[54], changing the elastic properties from soft to hard and accepted the loss of force-dependent patterning. The benefits were smaller dot sizes in the range of ≈ 40 nm and a pitch of ≈ 200 nm, which is a substantial improvement over the usual pitch of ≈ 10 μm between the center of each tip. The relation to DPL and μCP also suggest that

the same range of inks usable for these methods can be applied to some form of PPL, lipids^[55], proteins^[51] and other small functional molecules^[56] have already been successfully patterned.

2.1.2.3 Capillary stamping

One of the main drawbacks of μ CP and PPL is that no successive stamping is possible because the stamp neither has an ink delivery system nor an ink reservoir that feeds the contact elements new ink after a successful stamping cycle. To solve this problem, porous stamps were developed in 2009 and consisted of blends of different polymers (poly(ether sulfone) (PES)/poly(vinylpyrrolidone) (PVP)) which phase-separated into an interconnected porous structure^[57]. By adding a hydrophilic polymer into the blend, another drawback of conventional PDMS stamps could be solved: stamping from an aqueous solution.

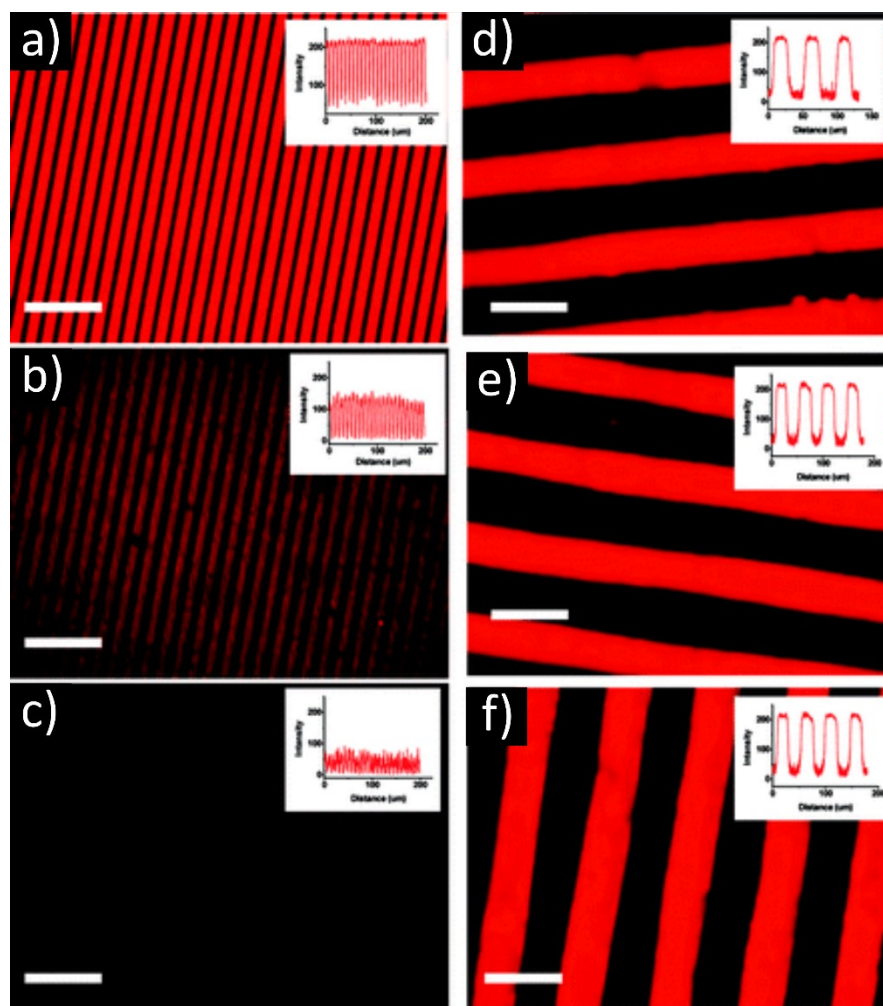


Figure 7: Fluorescence microscopy images and intensity profiles of stamped dye-labeled human immunoglobulin out of aqueous buffer conditions onto an amino-functionalized glass surface (scale bars = 40 μ m). a-c) Consecutive stamping cycles with an oxidized PDMS stamp. d-f) Consecutive stamping cycles with a porous PES/PVP stamp. Image taken from Xu *et al.*^[57].

As a proof of concept, a dye-labeled antibody was printed consecutively with a PES/PVP stamp and compared to a fresh plasma cleaned PDMS stamp. The porous stamp was able to pattern the surface without deterioration for three successive cycles (Figure 7d-f), while the PDMS stamp already showcased a drastic drop after the first cycle (Figure 7a-c). Similarly, stamping of dendrimers and hydrophilic nanoparticles became possible.

In 2018 Schmidt *et al.* developed mesoporous organo-silica stamps prepared *via* Sol-Gel synthesis with methyltrimethoxysilane (MTMS) as a precursor^[16]. It utilized the same principle of a continuous pore network for ink supply and made patterning from organic solvents down to the nanometer range possible. The stamp featured hexagonally arranged pillars (nearest neighbor distance: $\approx 1.2 - 1.3 \mu\text{m}$) with round tips ($\approx 400 \text{ nm}$ diameter) and pore sizes of $\approx 31 \text{ nm}$. A simple fabrication process (molding against a structured silicon wafer) and the ability to stamp sub-micron features with various inks under ambient conditions are vital characteristics of the method.

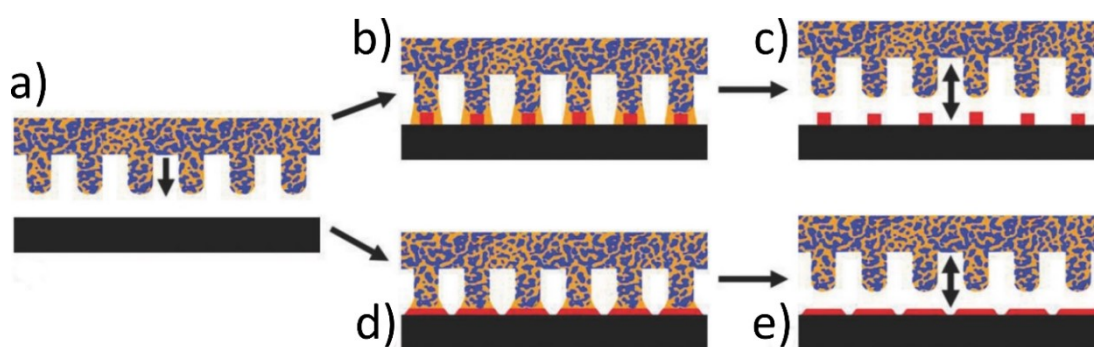


Figure 8: Capillary stamping illustration. a-c) Mesoporous silica stamps (blue) soaked with ink (orange) are brought into the proximity of the substrate. Liquid bridges form between the tips of the contact elements and the substrate. The dissolved molecules crystallize under the contact elements. Upon retraction of the stamp, the residual solvent evaporates, leaving nanoparticles (red) behind. a, d-e) Ink with a reactive component towards the substrate spreads with the meniscus of the liquid bridge and leaves behind a chemically patterned surface after the stamp removal. Illustration taken from Schmidt *et al.*^[16].

Ink is transferred *via* liquid bridges, which form between the contact elements and the substrate upon approach delivering the desired component to the surface. For inks such as C_{60} -fullerenes, crystallization into nanoparticles occurs under the contact elements of the stamp when the solvent evaporates (Figure 8a-c). Surface reactive molecules mixed into the ink spread with the meniscus of the solvent and leave, upon retraction of the stamp, a functionalized area behind (Figure 8a, d-e). The featured sizes are, amongst other factors, a result of the used ink and its wetting behavior on the respective surface in combination with the shape of the contact elements. Since its introduction, small organic molecules, polymers and nanodiamonds have been stamped by this method^[58].

Scanner-based capillary stamping by Hou *et al.* merged PPL and capillary stamping by utilizing porous polystyrene/poly-2-vinylpyridine block copolymer stamps^[59]. By selective swelling of P2VP, a continuous pore system with an average diameter of ≈ 40 nm was obtained. The stamp was attached to a porous glass layer and used with a piezo stage under defined atmospheric conditions for more than 800 consecutive stamping cycles without reinking. Simultaneous patterning of two different inks was also achieved by spatially dividing the stamp into two parts and loading them with two different inks at the same time.

2.2 Patterned substrates for bioanalytics

Spatial control of the desired substance on patterned substrates obtained by the above-mentioned techniques has a fundamental impact in a large variety of scientific fields^[60–63]. Particularly, biofunctionalizations in combination with patterned surfaces have broad applications in life sciences and dramatically reshaped the overall process in an efficient and sample-economical manner when paired with micro-/nanoarray technologies^[64,65].

Patterned biofunctionalized microarrays are commonly used for high-throughput screenings (HTS) of live cells for gene expression^[66], which are extremely useful for drug screenings^[67] or studies of stem cell differentiation^[68]. In one of these applications, HTS is performed with microwell plates under microfluidics conditions^[69]. In an effort to reduce the use of consumables (e.g., well plates, pipetting equipment) for HTS, patterned substrates based on superhydrophobic surfaces for live-cell imaging were developed^[70,71].

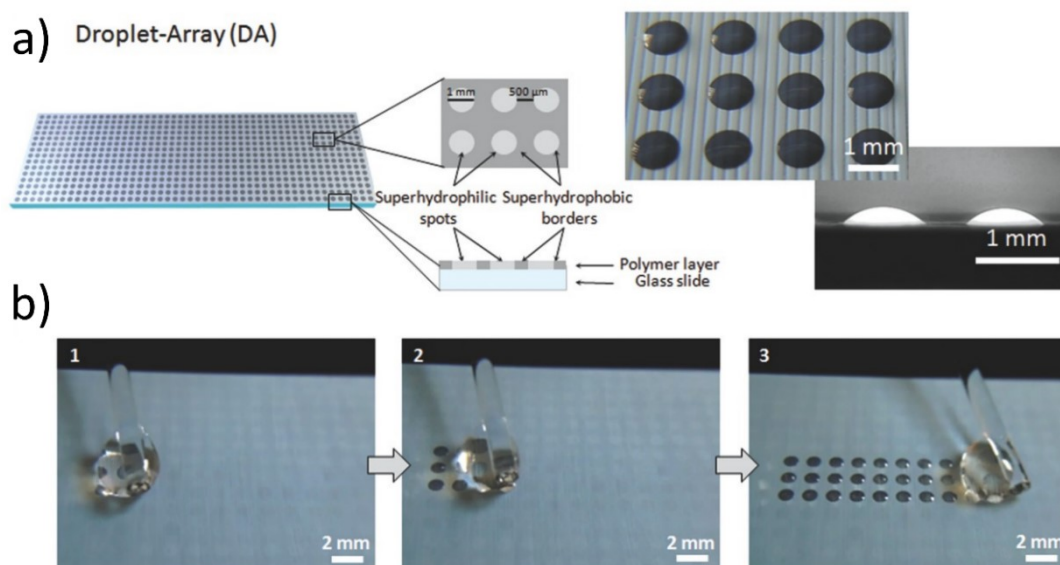


Figure 9: Illustration of the droplet array created by thiol-yne click chemistry. a) Schematic depiction of the droplet array and its dimensions (left). Images of droplets formed on the superhydrophobic-superhydrophilic array (right). b) Images of droplet creation by discontinuous dewetting. Image taken from Popova *et al.*^[70].

In order to create the patterned substrate, glass slides were first modified with a porous poly(2-hydroxyethyl methacrylate-*co*-ethylene dimethacrylate) (HEMA-EDMA) polymer film. Different photomasks achieved different patterns by UV-induced thiol-yne click chemistry and, depending on the applied thiol, rendered the illuminated surface hydrophobic or hydrophilic. The porous structure of the underlying polymer enhanced the physical effect even further to develop superhydrophobic-superhydrophilic spots^[72]. The array fabricated in this manner

exhibits droplet volumes of 60 nL (Figure 9) and feature sizes of ≈ 1 mm, which was scaled down in subsequent applications^[73]. For live-cell imaging, a cell suspension was added to the patterned substrate by discontinuous dewetting cells aggregated only on the hydrophilic dots^[74]. The array was then sandwiched with another array of the exact dimensions but patterned with chemicals of interest (*e.g.*, Calcein, Doxorubicin), thus transferring them to the cell containing droplet.

In another application, the micropatterned substrate is used for studying the interaction between proteins and nucleic acids on a single molecule level by tethering DNA onto a glass substrate^[75]. For this purpose, micropatterns were created by μ CP of streptavidin (SAV) onto a biotinylated glass surface (Figure 10). Since SAV has multiple binding sides, a biotinylated λ DNA was bound to the patterned SAV line arrays. Under the proper flow conditions, the DNA is stretched to full length within a flow chamber. These so-called DNA curtains give access to a high number of identical protein-DNA interaction sites, which can be analyzed with single-molecule detection methods^[76].

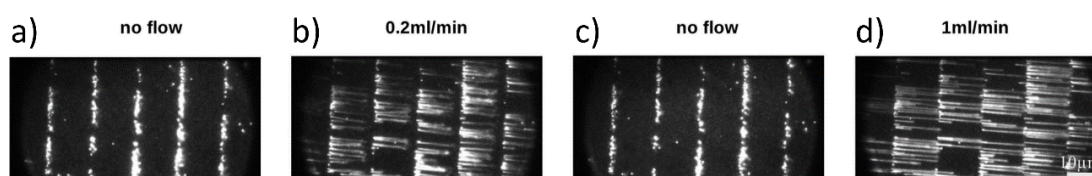


Figure 10: TIRFM images of SYTOX green-stained λ DNA tethered *via* biotin-streptavidin interaction to a glass substrate mounted in a flow cell. a,c) without flow b) with a low flow rate of 0.2 ml/min. d) a high flow rate of 1 ml/min. Image taken from Tutkus *et al.*^[75].

For bioanalytics of biomolecular interactions in their native cellular conditions, live-cell micropatterning has emerged as a powerful tool for exploring protein-protein interactions and mapping signaling pathways^[77]. In one application, patterning techniques provide precise control of ligand density by the lateral spacing of signaling ligand on the surface. Thus, the implication of ligand density and spacing for stimulating cell signaling could be quantitatively explored^[78]. For detecting signaling relevant protein-protein interactions in the cytosol, an *in situ* single cell pull-down (SiCPull) approach was developed on a micropatterned surface^[79].

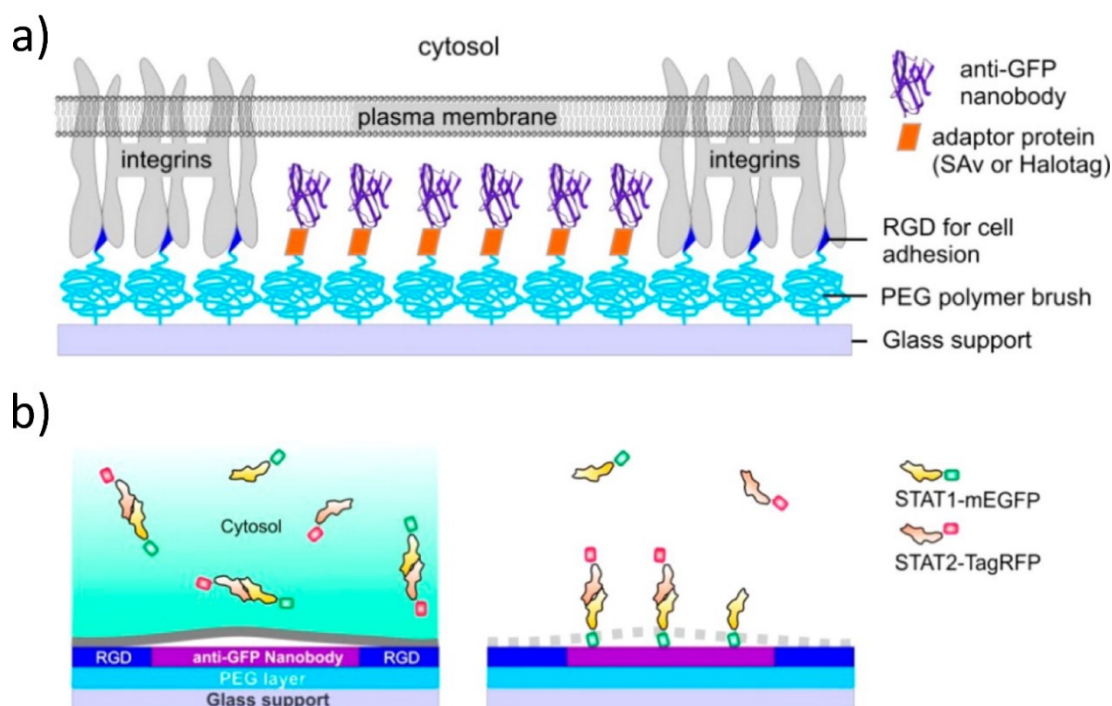


Figure 11: Schematic illustration of SiCPull assay for cytosolic protein complexes. a) Surface architecture of SiCPull micropatterned surface. b) Cell expressing both bait (STAT1-mEGFP) and prey (STAT2-TagRFP) protein in the cytosol (left). With lysing of the cell, the bait protein is pulled down *in situ*, and the prey is subsequently recruited. Illustration taken from Wedeking *et al.*^[79].

To generate micropatterned surfaces for SiCPull analysis of type I interferon (IFN) signaling, an anti-GFP nanobody was μ CP in line arrays onto a glass substrate modified with poly(L-lysine)-poly(ethylene glycol)-RGD (PLL-PEG-RGD) and poly(L-lysine)-poly(ethylene glycol)-HaloTag (PLL-PEG-HTL) (Figure 11a). The nanobody is used for immobilizing the key transcription factor in IFN signaling as the bait molecule, *i.e.*, signal transducer and activator of transcription 1 (STAT1) fused to an mEGFP and the prey protein STAT2 (Figure 11b)^[80]. With this approach, the stability of the signaling STAT1/STAT2 complex was determined by fluorescence recovery after photobleaching (FRAP). Stoichiometry of the heterodimeric protein complexes was obtained by single-molecule photobleaching counting. Taking advantage of the inherent contrast of micropatterning, SiCPull avoids the external supply of cell lysates^[81]. It thus allows reliable detection of protein complexes from individual cells and can be scaled up for paralleled single-cell analyses.

Inspired by the natural microcompartmentation, such as membrane skeleton, protein condensation and lipid microdomains, various surface micropatterning approaches have been developed in the past decades to manipulate signaling relevant proteins in the plasma membrane^[82–85]. Patterned surfaces with micrometer scale features similar to the size of the grown cells were used to investigate cell death or survival^[86]. Bovine endothelial cells were

confined into different shapes (circles, squares) of various sizes ranging from 5-50 μm by printing adhesion-promoting proteins onto the substrate. With decreasing size, cells entered apoptosis more frequently despite the addition of more matrix proteins to mediate focal adhesion. This result showed that the topographical structure of the biointerface between the cell and the substrate has determinant roles in cell fate^[87]. Micro-/nanopatterning of focal adhesion complexes, T-cell receptors and bone morphological proteins on the surface have been successfully exploited to steer cell adhesion, immune response and cell differentiation, respectively^[88–92]. Recently, micropatterned surfaces have been employed for quantifying mechanical forces and their essential role in adhesion, migration and proliferation were investigated^[93].

Live cell imaging in combination with biofunctionalized micropatterned surfaces strengthens the mechanistic understanding of regulatory processes for cell signaling. These results inspired the development of biofunctionalized surfaces with tailored nanoscale features for further exploring spatiotemporal control on cell signaling.

2.3 Wnt signaling pathway

The Wnt signaling pathway is an evolutionarily conserved pathway responsible for cell differentiation, cell proliferation and cell migration^[94]. Mal-regulations of Wnt signaling is the cause of a variety of diseases, such as cancer, congenital malformations and osteoporosis^[95]. It is categorized into two main pathways, the canonical Wnt pathway (i.e., Wnt/ β -catenin pathway) and the non-canonical pathway, including the planar cell polarity pathway and the Wnt/ Ca^{2+} pathway^[96,97]. In mammals, 19 Wnts and 10 Frizzled (Fzd) proteins interact with a high degree of promiscuity yet contribute to distinct biological functions. All Wnt proteins have a conserved Ser residue for post-translational palmitoylation^[98]. Palmitoylation limits the diffusion of Wnts in the extracellular space due to interactions with cellular membranes^[99]. Therefore, Wnt signaling is spatiotemporally confined within tissues at a one-cell range as a morphogen^[100]. Fzd has seven transmembrane helices resembling a G-protein-coupled receptor^[101]. The extracellular cysteine-rich domain (CRD) of Fzd binds to Wnts. Low-density lipoprotein receptor-related protein 5/6 (Lrp5/6) are involved in the canonical Wnt signaling as co-receptors. They are single-span transmembrane receptors containing 4 extracellular β -propeller and 5 intracellular PPPSPxS/T motifs^[102]. In the canonical Wnt signaling pathway, Wnts (Wnt1, 2, 3, 3a, 8 or 8a) or engineered Wnt surrogate ligands^[103,104] crosslink Fzd with co-receptor Lrp5/6 in the plasma membrane, followed by phosphorylation of the intracellular domain of Lrp5/6. The downstream signaling includes a variety of different proteins, eventually leading to the destruction of β -catenin in its off-state (Figure 12a) or the accumulation of β -catenin in its on-

state (Figure 12b). As a consequence of Wnt stimulation, β -catenin gains higher levels in the cytoplasm. It transfers into the nucleus and activates, with the help of the transcription factor/lymphoid enhancer factor (TCF/LeF), transcription of Wnt/ β -catenin target genes^[105].

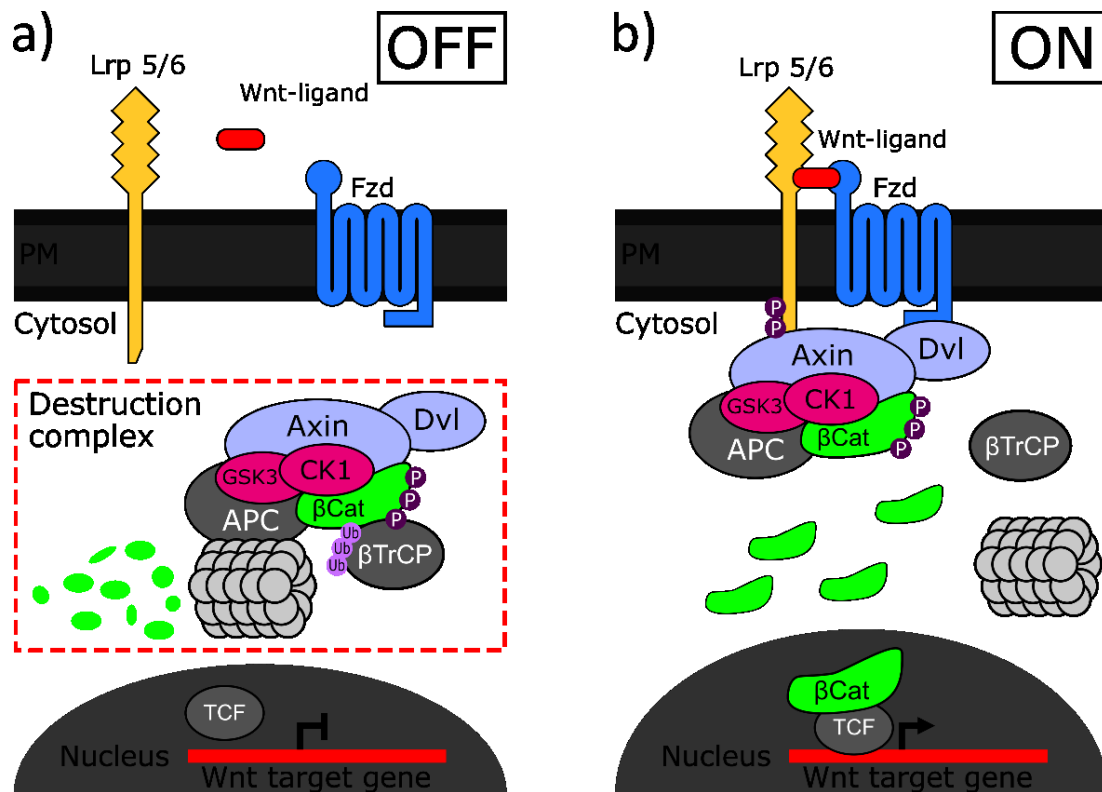


Figure 12: Schematic illustration of the Wnt/ β -Catenin pathway. a) Wnt signaling pathway off. The Wnt-ligand is not binding to the Fzd receptor (blue) and not heterodimerizing Lrp (yellow) and Fzd. The destruction complex consisting of the scaffold proteins Axin and Dvl (light blue), the two kinases CK1 and GSK3 (magenta) and the tumor suppressor protein APC (grey) is able to bind and phosphorylate β -Catenin (green) and therefore recruit β TrCP (grey). β TrCP is subsequently responsible for the ubiquitination of β -Catenin and primes it for its proteasomal degradation. b) Wnt signaling pathway on. When the Wnt-ligand engages and dimerizes Lrp and Fzd, Lrp is phosphorylated and able to draw the destruction complex to the cell membrane by binding Axin. When the DC is attached to the membrane receptors by Axin and Fzd, the binding site for β TrCP is blocked and β -Catenin is not degraded, thus enriching in the cytosol. Upon translocation into the nucleus, β -Catenin activates with the help of transcription factor TCF (grey) the Wnt target genes. Schematic adapted from Nusse *et al.*^[106].

Current studies depict a switch of two states for the canonical Wnt signaling. In the off-state, the cytosolic proteins Dvl (Dishevelled segment polarity protein 1, 2, and 3) and Axin (Axis inhibition protein 1 and 2) bind together and act as a scaffold to the Adenomatous polyposis coli (APC) and the two kinases Casein kinase 1 (CK1) and Glycogen synthase kinase 3 (GSK3). The complex is capable of phosphorylation of β -catenin, which is bound to Axin as well (Figure 12a). This whole construct is termed the destruction complex (DC). Then the E3 ubiquitin ligase β -transducin repeat-containing protein (β -TrCP) is recruited, prompting ubiquitination of β -catenin and its proteasomal degradation. In the on-state, the lipidated Wnt-Ligand activates

the pathway by binding to Fzd and Lrp5/6, forming heterodimeric receptors on the cell surface (Figure 12b). This leads to phosphorylation of intracellular PPPSPxS/T motifs of Lrp5/6 and recruits DC to the cell membrane. Moreover, Dvl is consecutively binding to Fzd, thus facilitates the binding of Axin to Lrp6^[107]. Upon association with phosphorylated Lrp5/6, the ability of the DC to promote β -catenin degradation is impaired, mainly because the binding site for the ubiquitin ligase is blocked. Without ubiquitination, the newly formed β -catenin accumulates in the cytosol, eventually transferring into the nucleus^[106].

2.4 Optogenetics

The optogenetics toolbox provides precise temporal control combined with a high degree of spatial control^[108]. Developed to manipulate the action potential of neurons^[109], the fusion of proteins of interest to light-inducible dimers also gained a lot of attention in protein-protein interaction experiments^[110]. Activation of a variety of cell biological systems, such as signaling pathways^[111], DNA transcription^[112] or protein degradation^[113] by light irradiation at different wavelengths, have been established (Figure 13).

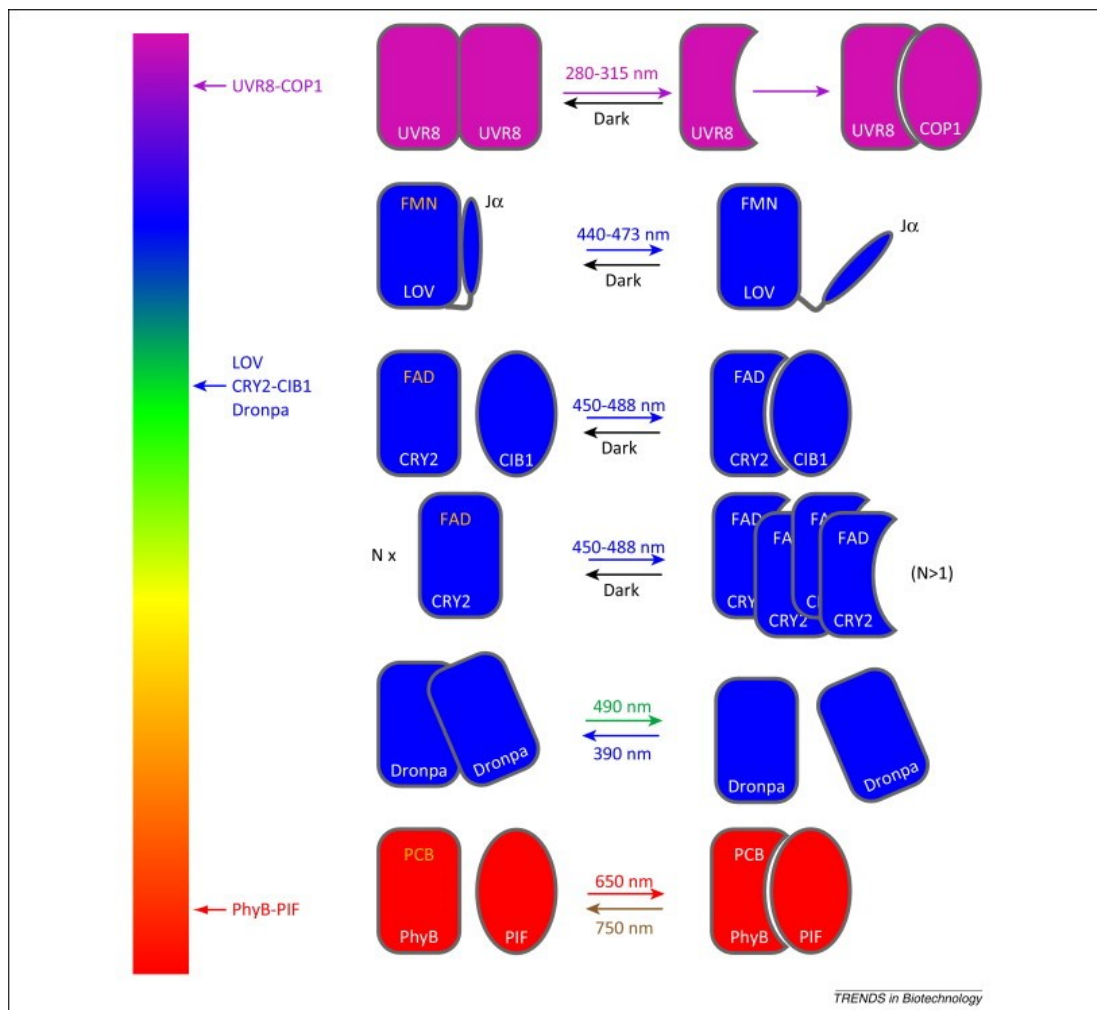


Figure 13: Overview of photoswitchable systems (UVR8-COP1, LOV, CRY2-CIB1, Dronpa, PhyB-PIF), cofactors (FMN, FAD, PCB) (yellow: ground state; white: photoactive state) and their induced conformational change upon illumination with their effective wavelength. Illustration taken from Zhang *et al.*^[110].

Cryptochrome 2 (CRY2) and Phytochrome B (PhyB) form heterodimers when illuminated with 450-488 nm light for CRY2 and 650 nm light for PhyB, respectively. In its photoexcited state, CRY2 binds to cryptochrome interaction basic helix-loop-helix (CIB1) within seconds and reverts to its monomeric state within minutes without activating blue light present^[114]. It is also able to

form oligomers with the same photo-responsive properties^[115]. With red light, PhyB can dimerize with the phytochrome interaction factor (PIF) if the cofactor phycocyanobilin (PCB) is present^[116]. The association reaction occurs within seconds after the illumination and is centered around a conformational change of PCB. In contrast to the CRY2 system, the dissociation does not take place automatically but needs an infrared pulse of 750 nm light^[117]. The photoactivatable Dronpa protein is a system that does not require cofactors. By forming tetramers, it dissociates upon irradiation with 490-500 nm light into monomers and can be brought back into its tetrameric state by 390-400 nm light^[118]. The light, oxygen and voltage domain (LOV) needs an additional cofactor/chromophore for its photoreactive function, which is flavin mononucleotide (FMN), an abundant molecule in mammalian cells^[119]. FMN is anchored to the per-arnt-sim (PAS) core of the LOV and upon blue light illumination, a conserved cysteine residue covalently binds to the cofactor. The introduction of the covalent bond is accompanied by a conformational change along the PAS core and leads to a tilt of the usually tethered J α helix away from the core. Hydrolysis of the cysteine-FMN bond in the dark state secures the J α helix back onto the LOV within several seconds^[120]. The underlying mechanism of the LOV system is the uncaging of a responsive element either through direct attachment to the J α helix or the dimerization of a second protein to the helix. The improved light-inducible dimer (iLID) is based on the LOV2 domain of phototropin 1 from *Avena Sativa* (As) and the short peptide SsrA from *Escherichia coli*. It utilizes the AsLOV2 system to cage the SsrA peptide introduced to the J α helix from its binding adaptor protein SspB (stringent starvation protein B). Several mutations to the AsLOV2 domain were made to improve binding parameters and mutations to the adaptor protein SspB resulted in the two variants, iLID nano (wild type) and micro (R73Q), with different affinity ranges^[121]. Further development led to the SspB milli (R73Q, A58V) version with yet another increase in binding affinity^[122]. Several biomolecular investigations using the iLID system have been conducted^[123,124].

3 Experimental

3.1 Materials

Table 1: List of used chemicals with respective supplier and their abbreviation.

| Chemical name | Supplier | Grade | Abbreviation |
|---|-----------------|---------------|-----------------|
| Acetic acid | Fisher Chemical | 99 %, glacial | |
| <i>N</i> -Aminoethyl-aza-2,2-dimethyl-4-methylsilacyclopentane | Gelest | | Cyclozasilane |
| ATTO 488- <i>N</i> -hydroxysuccinimidyl ester | ATTO-TEC | | ATTO 488 NHS |
| ATTO 647- <i>N</i> -hydroxysuccinimidyl ester | ATTO-TEC | | ATTO 647N NHS |
| ATTO 647-hydroxysuccinimidyl ester | ATTO-TEC | | ATTO 647 NHS |
| ATTO 655 maleimide | ATTO-TEC | | |
| Biotinyl-(polyethylenglycol) ₅₀₀₀ -succinimidyl valerate | Laysan Bio Inc | | bt-PEG-SVA |
| Bovine serum albumin | Carl Roth | ≥ 98 % | BSA |
| (2'Z,3'E)-6-Bromoindirubin-3'-oxime | Sigma Aldrich | ≥ 98 % | BIO |
| α-bromoisobutyryl bromide | Alfa Aesar | 98 % | BIBB |
| Copper(II)bromide | Alfa Aesar | 99 % | |
| Cyanine5-dibenzocyclooctyne | Lumiprobe | | Cy5-DBCO |
| Dibenzocyclooctyne-(polyethyleneglycol) ₁₂ - <i>N</i> -hydroxysuccinimidyl ester | Jena Bioscience | | NHS-PEG12-DBCO |
| Dichlormethane | Alfa Aesar | 99.7 %, dry | DCM |
| 2,2-Dimethoxy-1-thia-2-silacyclopentane | Gelest | | Cyclothiasilane |
| Dimethyldichlorosilane | Merck | 98 % | DMDCS |
| Dimethylformamide | Sigma Aldrich | 99.8 %, dry | DMF |
| Diphenyldichlorosilane | Gelest | | DPDCS |
| Ethyl-α-bromoisobutyrate | Sigma Aldrich | 98 % | EBIB |
| 3-(Ethyliminomethyleneamino)- <i>N,N</i> -dimethylpropan-1-amine | Carl Roth | ≥ 99 % | EDC |
| 2-[4-(2-hydroxyethyl)piperazin-1-yl]ethanesulfonic acid | Carl Roth | 99.5 % | HEPES |
| Methoxy-(polyethyleneglycol) ₅₀₀₀ -succinimidyl valerate | Laysan Bio Inc | | mPEG-SVA |
| Methyltrimethoxysilane | Sigma Aldrich | 98 % | MTMS |
| 1-Naphthylmethyltrichlorosilane | Gelest | | NMTS |
| Octadecyltrichlorosilane | Sigma Aldrich | >90 % | ODTS |

| | | | |
|---|---------------|------------|-------|
| <i>N,N,N',N'',N''</i>- pentamethyldiethylenetriamine | Alfa Aesar | 98 % | PMDTA |
| Pluronic F127 | Sigma Aldrich | BioReagent | F127 |
| Sodiumazide | Sigma Aldrich | 99 % | |
| Sodiumchloride | Carl Roth | 99.5 % | |
| Styrene | Sigma Aldrich | ≥ 99 % | |
| Tin(II) 2-ethylhexanoate | Alfa Aesar | 96 % | |
| Toluene | Alfa Aesar | 99.8 % | |
| Triethylamine | Alfa Aesar | 99 % | TEA |
| Urea | Sigma Aldrich | BioReagent | |

Other standard solvents were purchased from Fisher Chemical and used without further purification. Reagents for mammalian cell culture were obtained from PAN-Biotech. Plasmids, proteins and antibodies were kindly provided by the group of Prof. Dr. Jacob Piehler (Biophysics, University of Osnabrueck).

3.2 Characterization

3.2.1 Atomic force microscopy

Atomic force microscopy (AFM) was performed in semicontact mode using an NT-MDT NTEGRA microscope with NSG10 cantilevers purchased from NT-MDT (gold-coated silicon, resonant frequency: 140 kHz-390 kHz, force constant: 3.1 Nm⁻¹-37.6 Nm⁻¹)

3.2.2 Scanning electron microscopy

Scanning electron microscopy (SEM) images were acquired with a Zeiss Auriga scanning electron microscope operated at an accelerating voltage of 3 keV. For detection, both secondary electron secondary ion detector (SESI) and in-lens detector were used. If necessary, the samples were sputtered with platinum/iridium before imaging.

3.2.3 Water contact angle measurements

Water contact angles (CA) were measured with a Krüss DSA100 drop shape analyzer in sessile drop mode at ≈ 23 °C and a relative humidity of ≈ 45 %. For every sample, three CA measurements were taken and averaged to give the final value.

3.2.4 X-ray photoelectron spectroscopy

X-ray photoelectron spectroscopy (XPS) measurements were carried out under an ultra-high vacuum in an ESCA-unit Phi 5000 VersaProbe III with a base pressure of 10^{-9} mbar. As an X-ray source, the Al K_{α} radiation of a mono-chromatized Al anode ($h\nu = 486.6$ eV) was used. Sample charging was prevented by using simultaneously both an ion gun and an electron gun simultaneously. The signals were analyzed with a 32-channel electrostatic hemispherical electronic analyzer. The spectra were acquired at a take-off angle of 15° to enhance the contribution of the aminosilane nanodot arrays. The XP spectra were calibrated using the carbon C 1s (185.0 eV) peak. For analyzing and fitting the XP spectra, the Software XPSpeak 4.1 was used.

3.2.5 Total internal reflection fluorescence microscopy

Total internal reflection fluorescence microscopy (TIRFM) was carried out at 25°C using an inverted microscope (Olympus IX-83) equipped with a 4-Line TIRF condenser (Olympus TIRF 4-Line). The setup was equipped with a 488 nm diode laser (LuxX 488-200; Omicron), 561 nm and 642 nm fiber laser (MPB Communications). The lasers were operated in combination with a TIRF pentaband polychroic beamsplitter (Semrock zt405/488/561/640/730rpc) and a pentabandpass emitter filter (BrightLine HC 440/521/607/694/809). Images were acquired with an electron-multiplying CCD camera (Andor iXon Ultra 897) through a 150-fold oil immersion objective (Olympus UAPON150x TIRF, NA 1.45) or a 100-fold oil immersion objective (Olympus UPLAPO 100x HR, NA 1,5). DIC images were taken with a DIC condenser equipped to the system.

For the optogenetics experiment, the 488 nm laser was fitted with a 5 % transmission filter. Ten consecutive cycles of activation (30 s) and decay (90 s) were performed while imaging the 561 nm channel with one frame per second (fps). The 488 nm laser was turned on continuously during the activation periods.

Direct stochastic optical reconstruction microscopy (dSTORM) image sequences were acquired with a 2-Amino-2-(hydroxymethyl)propane-1,3-diol (TRIS) imaging buffer (150 mM TRIS, 10mM NaCl, pH: 8.5) containing β -mercaptoethanol (β -ME) and an oxygen scavenger system (glucose, glucose oxidase, catalase). Prior to the recording, the sample area was illuminated with the respective laser for 120 s at full intensity to transfer most dyes into the dark state. Recordings were taken over a time period of approximately 12,5 min with 40 fps, using a 405 nm Laser (BCL-100-405, CrystaLaser) to recover the dye from the dark state.

Reconstruction of the super-resolution image was performed with the ImageJ plugin ThunderSTORM^[125].

3.2.6 Image analysis

For spot size analysis, TIRFM images were deconvolved with Huygens software (Huygens Core, Software Version v3.5, Scientific Volume Imaging, Netherlands, <http://svi.nl>). A theoretical point spread function (PSF) for widefield microscopy was used with the following settings: deconvolution algorithm = classic maximum likelihood estimation (CMLE); background mode = automatic; signal-to-noise ratio (SNR) = 30; number of iterations = 20; quality change number = 0.01. The deconvolved images were then further processed by a watershed algorithm (ImageJ; Interactive H_Watershed from MPI CBG) with varying values for seed and intensity threshold. Both parameters were set, so the algorithm matches the outlines of each spot given by the deconvolved images. Area (A), circularity (C) and aspect ratio (AR) were then deducted for each dot and plotted in a histogram.

Circularity and aspect ratio were determined as geometric descriptors for the characterization of the stamped pattern to showcase the deviation from an ideal circle.

$$C = \frac{4\pi \cdot Area}{perimeter^2} \quad (1)$$

$$AR = \frac{[major\ axis\ lenght]}{[minor\ axis\ lenght]} \quad (2)$$

Dot colocalization analysis was performed by a spot colocalization program. For each analyzed channel a Tikhonov deconvolution is performed to reverse the effect of the point spread function in the fluorescence image and the nanodot array. The PSF of the microscope was approximated by 2D-Gaussian and a regularization factor for smoothness ($\gamma = 10^{-1.5}$) was added for the deconvolution process. Then the individual nanodots were identified by smoothing the deconvolved image and looking for the local maxima in the pixel intensities. In order to discriminate against noise peaks, a minimum signal threshold is estimated using Otsu's method^[126]. The detected nanodots are further refined by calculating the median distance between nanodots and then discarding all nanodots that do not satisfy at least six such neighbors. The accepted pixels are then thickened radially by 2 pixels to capture the whole printed area but were always separated by 1 pixel. Additionally, a cell mask is generated by dilating the image further by 2 pixels.

The contrast is calculated relative to the local background estimated from the pixels surrounding each identified nanodot. To get the minimum effective contrast of Lrp6 (i.e., the threshold for

activation), the effective response of each channel was analyzed by fitting a 2-Fraction Gaussian Mixture. Dots were classified by their probability to create high contrast in respect to the Lrp6 channel. Dots with a high contrast probability were then sampled via bootstrapping the 5 percentile of Lrp6 contrast responsible for the recruitment of the other two channels and used to determine the minimum effective Lrp6 contrast. The effective contrast value calculated between Lrp6 and Axin1 was transferred to the Lrp6/Fzd8 graph. Correlation coefficients and dependencies were determined by calculating looking at the contrast distributions to the ratio = 0.

Intensity measurements for β -Catenin immunostaining experiments were taken by outlining the borders of the cell and measuring the mean intensity with ImageJ. For nucleus measurements, outlines of the nucleus were taken from DIC images and transferred to the immunostaining channel and subsequently analyzed. Values taken from different sessions were normalized against the negative control HeLa wt, except for the values gathered for the NGS 2 h treated cells. Those values were normalized against the negative control of Lrp6-transfected cells without a pattern, and a factor was multiplied with the obtained values to compensate for the different reference. The factor consisted of the mean value of the negative HeLa wt control, divided by the mean value of the Lrp6-transfected cells without a pattern.

3.2.7 Total internal reflection fluorescence - Reflectance interference spectroscopy

A home-built setup for total internal reflection fluorescence spectroscopy (TIRF) and reflectance interference spectroscopy (RIfS) was used as described in detail before^[127,128]. For TIRF-RIfS detection of BSA on coated substrates (substrates consisted of 1x1 cm² glass chips with a 500-600 nm silica interference layer on top), BSA in HEPES buffered saline (HBS) (20 mM HEPES, 150 mM NaCl, pH 7.5) was injected into the flow chamber for 225 s and followed by HBS buffer wash. For binding measurements of HaloTag-mEGFP to BSA-HTL, BSA-HTL was injected over a period of 225 s, followed by an injection of tagless-mEGFP (225 s) and HaloTag-mEGFP (225 s). Each protein injection was separated by a washing step with HBS. Mass signals of protein binding and fluorescence signals were recorded simultaneously in the RIfS channel and the TIRF channel, respectively.

3.2.8 Matrix-assisted laser desorption/ionization

Matrix-assisted laser desorption/ionization (MALDI) measurements were performed with a Bruker UltrafleXtreme in linear mode with sDHB as the matrix for every sample.

3.2.9 Ultraviolet-visible spectroscopy

Ultraviolet-visible spectroscopy (UV/Vis) was carried out with a NanoDrop One from Thermo Scientific. Protein concentrations were calculated from the measured adsorption value at 280 nm in combination with the protein specific molar extinction coefficient.

3.3 Preparation and functionalization

3.3.1 Modification of glass substrates

Substrates were cleaned with lint-free cloths and plasma cleaned for 10 min in a Diener Femto plasma cleaner prior to their silanization. Immediately afterward, the slides were immersed into a 2 % v/v solution of the specified silane in dry toluene for 1-2 h. After the given time, the substrates were rinsed thoroughly with toluene and ethanol to remove residual unreacted silane and used within a timeframe of 2h. This procedure was applied for all silanes with the exception of OTS and FDTS. OTS was used in the same manner as described, but the slides were taken out after a reaction time of 10 min. FDTS was deposited *via* vapor deposition. Therefore, the clean substrates were heated to 80 °C for 2 h in a sealed container in the presence of FDTS ($\approx 200 \mu\text{l}$) and used without any further washing step.

Hydroxyl-terminated glass surfaces were fabricated by plasma cleaning only.

Graphene modified glass slides were prepared on plasma cleaned glass surfaces. From a graphene wafer (Graphenea, Easy Transfer: Monolayer Graphene on Polymer Film), a $\approx 5 \times 5$ mm piece was separated and immersed into water. The supporting back-layer was removed and the remaining graphene piece was carefully dragged onto the desired position on the glass slide. The slide was air-dried until all visible water was evaporated, then the samples were placed in a 150 °C convection oven for 2 h with air atmosphere. In order to remove all residual moisture, the slides were placed in a freeze dryer overnight. The last polymer protection layer on the graphene was removed with an acetone and an isopropanol bath for 15 min each. Afterward, the slides were blown dry with N_2 .

3.3.2 Stamp synthesis of mesoporous silica stamps

Mesoporous silica stamps were prepared following the procedures reported by Schmidt *et al.*^[16]. Hence macroporous silicon (mSi) was silanized in a 2 % v/v DMDCS in n-hexane overnight at 40 °C and washed with ethanol afterward. The main stamp material was synthesized by adding 1 g of Pluronic F127, 0.5 g of Urea to 9.98 mL of 10 mM aqueous acetic acid solution and stirred until a transparent solution was obtained. Then, 4.98 mL MTMS was added and the reaction

mixture was stirred for an additional 30 min until the desired sol was obtained. In the next step, the sol was poured into a polystyrene container with the silanized mSi on the bottom and tightly sealed with Parafilm. The container was placed in a circulation oven at 60 °C for 4 d with an air atmosphere. After aging, the resulting silica monoliths were removed from their templates and neutralized with MilliQ water for 1 d at 60 °C in order to remove any residual chemicals. The solvent was exchanged by placing the water-soaked stamps in EtOH for approximately 1 d and refreshing the ethanol at least three times. Stamps were stored in EtOH and used no later than two weeks.

3.3.3 Synthesis of functionalized bovine serum albumin

A solution of 1 g bovine serum albumin (BSA) in 5 mL HBS was dialyzed in 2 L HBS at 4 °C for 48 h (dialysis tubing: 14.000 kDa cutoff). The remaining concentration was determined *via* UV-Vis spectrometry and the purified BSA was used for every further functionalization.

3.3.4 Dye functionalization of BSA

NHS functionalized dyes were mixed in a ratio of 1:1 ration with purified BSA and shaken for 4 h at RT. The reaction solution was then transferred into a BSA pre-blocked Amicon-Ultra 0.5 mL centrifugal filter (cutoff: 3000) and diluted with 500 µl HBS. The vessel was centrifuged for 15 min at 14.000 G and the resulting centrifugate was discarded. This step was repeated three times until the supernatant was collected and analyzed *via* UV-Vis spectrometry.

3.3.5 HaloTag-Ligand functionalization of BSA

369 µL purified BSA (0.37 µmol) was added to 3.4 mL HBS and combined with a solution of 96 mg EDC (0.5 mmol) in 1 mL HBS. 1.7 mg HaloTag-NH₂ (HTL, 7.6 µmol) was dissolved in 200 µL EtOH, added to the reaction mixture and shaken overnight at 4 °C. The completed reaction was then dialyzed in 2 L HBS for 24 h at 4 °C (14.000 kDa cutoff) and analyzed, resulting in a 62.8 µM BSA-HTL solution. MALDI analysis showed a broad peak at 69511 m/z, compared to unfunctionalized purified BSA, a mass difference of 3058 m/z. Thus, resulting in a labeling degree of ≈ 13.7 HTL per BSA molecule.

3.4 Capillary stamping

3.4.1 Pre-stamping preparations of porous silica stamps

The synthesized stamps were ground on a piece of sandpaper until they were able to be mounted to the stamp holder. On the front side, the edges were additionally trimmed to prevent

small pieces from breaking off during the stamping procedure; this also helped to remove formed air bubbles that could cause ink leakage. The finished stamps had a suitable stamping surface of about 5 x 5 mm² and a flat backside, which was necessary to fix it to the stamp holder *via* double-sided adhesive tape. The holder was a stainless steel cylinder (height 4.5 cm; diameter 2 cm; mass \approx 27g), fitted with a 3 mm thick poly(dimethoxysilane) (PDMS) pad on its flat cylinder base. The PDMS was mixed at a ratio of 1:9 (Base : Prepolymer) and cured at room temperature for a week. With this setup, manual stamping could be performed. While being a feasible option, the stamp holder was exchanged with a smaller steel cylinder (height 1 cm; diameter 1.5 cm; mass \approx 16 g) and fixed to the Proxxon Micro-Press MP 120 with a steel adapter secured by a screw. In the same manner, a PDMS-back layer was fixed to the holder to help with the alignment during the stamping procedure. The Micro-Press, although still manually driven, helped to control stamping parameters such as pressure better and it completely eradicated the problem of pattern shifts in x, y-direction by controlling the approach in z-direction.

Table 2: Detailed register of all stamped reagents with their respective post-treatment and analysis methods. For each method stamping by hand or stamping with the help of the Micro-Press is marked.

| Stamped reagent | Post treatment and analysis | Stamping | |
|-----------------------------|--|----------|-------------|
| | | By hand | Micro-Press |
| Heterocyclic silanes | Fluorescent labeling/dot array analysis | X | |
| | PS-brush synthesis | X | |
| | Biofunctionalization with HTL | X | |
| PLL-PEG-bt | Fluorescent labeling/dot array analysis | X | |
| SAV-Cy5 | Fluorescent labeling/dot array analysis | X | |
| BSA-HTL | Fluorescent labeling/dot array analysis | X | |
| | dDARPin functionalization/fluorescent labeling/dot array analysis | X | |
| | dDARPin functionalization/fluorescent labeling/dot array analysis on graphene modified surface | | X |
| | dDARPin functionalization/optogenetics | | X |
| | dDARPin functionalization/investigation of Wnt signaling pathway | | X |

3.4.2 Heterocyclic silanes

Ethanol-soaked stamps were immersed into 3 ml toluene, which was exchanged 3 times until the solvent was exchanged entirely. Then the stamps were infiltrated for ≈ 15 min with the ink-solution, 0.5 mM cycloazasilane and 2 mM cyclothiosilane in dry toluene, respectively. After infiltration, the backside of the stamps was patted dry, fixed to the stamp holder and freshly prepared hydroxyl-terminated glass slides were patterned by pressing the stamp onto the surface for 1-2 s. In this manner, up to 10 slides or more were able to be patterned without reloading the porous stamp with ink.

3.4.3 Streptavidin-cyanine 5

A mixture with a mass ratio of 20:1 n-hydroxysuccinimide-polyethylene glycol-methoxy (NHS-PEG-OMe) and n-hydroxysuccinimide-polyethylen glycol-biotin (NHS-PEG-bt) was weighed and dissolved in HBS. The solution was centrifuged for 5 min and 75 μ l were sandwiched between two cycloazasilane modified glass substrates. After 2 h, the samples were washed with MilliQ water and dried under nitrogen.

Ethanol-soaked stamps were immersed into 5 ml MilliQ water, which was exchanged 3 times until the solvent was exchanged entirely. Then the stamps were infiltrated for ≈ 30 min with a 0.27 μ M Streptavidin – Cyanine 5 (SAV-Cy5) solution in HBS. In order to remove excess ink, the stamp was dried under a stream of nitrogen until a clear rainbow shine was visible. After attachment to the stamp holder, modified glass substrates were patterned for $\approx 1-2$ s, subsequently washed with water, shortly dried with N_2 and placed in HBS. For multiple patterning cycles, new ink was added on the structured stamp surface for ≈ 1 min and blown dry afterward.

3.4.4 BSA-ATTO 647N

Ethanol-soaked stamps were immersed into 5 ml MilliQ water, which was refreshed 3 times until the solvent was exchanged entirely. Then the stamps were infiltrated for ≈ 30 min with a 6 μ M BSA-ATTO 647N solution in HBS. In order to remove excess ink, the stamp was dried under a stream of nitrogen until a clear rainbow shine was visible. After attachment to the stamp holder, NMTS modified glass slides were patterned for $\approx 3-5$ s. After washing with water, the samples were stored in HBS until further use. For multiple patterning cycles, new ink was added on the structured stamp surface for ≈ 1 min and blown dry afterward.

3.4.5 BSA-HTL

Ethanol-soaked stamps were immersed into 5 ml MilliQ water, which was refreshed 3 times until the solvent was exchanged entirely. Then the stamps were infiltrated for ≈ 30 min with a $15 \mu\text{M}$ Bovine serum albumin-HaloTag-Ligand (BSA-HTL) solution in HBS. In order to remove excess ink, the stamp was dried under a stream of nitrogen until a clear rainbow shine was visible. After attachment to the stamp holder, NMTS or Graphene modified glass substrates were patterned for $\approx 3-5$ s and backfilled with fetal bovine serum (FBS) or 10 % BSA in HBS for 15 min. After washing with water, the samples were stored in HBS until further use. For multiple patterning cycles, new ink was added on the structured stamp surface for ≈ 1 min and blown dry afterward.

Co-stamping of BSA-HTL with fluorescently labeled BSA was performed by adding $1.6 \mu\text{M}$ ATTO 488-BSA, $0.3 \mu\text{M}$ TexasRed-BSA or $1.2 \mu\text{M}$ ATTO 647N correspondingly to the BSA-HTL containing ink solution.

3.4.6 Poly(L-lysine)-poly(ethylene glycol)-biotin (PLL-PEG-bt)

Ethanol infiltrated stamps were immersed into a $500 \mu\text{g/ml}$ PLL-PEG-bt (biotin labeling degree: 5 %) in a 70 % EtOH to 30 % H_2O (v/v) ink. After 1 h, the stamps were removed from the solution, air-dried shortly and fixed to the stamp holder. The freshly prepared DMDCS glass slides were patterned by pressing the stamp onto the surface for 5-10 s. The samples were left for 3 min and then washed three times with MilliQ water. Unspecific binding sites were blocked with a BSA solution (2 % m/m in HBS) for 10 min at RT.

3.5 Post-stamping treatments

3.5.1 Fluorescent labeling of heterocyclic silane patterns

Aminosilane nanodots were labeled with a 0.5 mM solution of ATTO 647 NHS in HBS for 10 min. The samples were washed with MilliQ water three times. The same procedure was applied to label the thiosilane nanodots, the difference being that ATTO 655 maleimide was used as a fluorescent dye.

3.5.2 Synthesis of PS brushes on cycloazasilane patterns

Glass slides patterned with arrays of cycloazasilane nanodots were immersed into a mixture of 5 mL dry DCM, 123 mL BIBB (1 mmol) and 207 mL TEA (1.5 mmol) for 12 h while shaking. Then, the glass slides were washed with DCM, H_2O and EtOH. To remove stabilizers, 5 mL styrene was subjected to column chromatography using basic alumina as a stationary phase, then collected

in a flask and degassed with argon for 30 min. The prepared glass slides, 3.2 mL EBIB (0.02 mmol), 181 mL of a CuBr_2/DMF solution (0.1 M) and 181 mL of a PMDTA/DMF solution (0.5 M) were added under argon. The flask was sealed with a septum cap and heated to 90 °C. Through the septum cap, 271 mL Sn(II) 2-ethylhexanoate (0.8 mmol) was added to start the reaction. After a polymerization time of 7 h the reaction mixture became viscous and the reaction was stopped by cooling to room temperature and exposure of the catalyst to air. The glass slides were ultrasonicated in methanol, EtOH, DCM and DMF for 15 min to remove excess polymer.

3.5.3 End-chain functionalization of PS brush

The PS brush samples were immersed into a 50 mM NaN_3 solution in DMF for 90 min. The slides were subsequently washed with H_2O and EtOH. As a backfilling agent, PLL-PEG-OMe (2 $\mu\text{g}/\text{ml}$) was added and washed away with H_2O after 15 min. The dye labeling step was performed in EtOH with a 1 μM Cy5-DBCO solution for 1 h. Afterward, the samples were rinsed extensively with H_2O and EtOH in order to remove any unbound dye.

3.5.4 Immobilization of HaloTag-mEGFP protein on cycloazasilane patterns

Aminosilane nanodots stamped on glass slides were functionalized with 1 mM DBCO-PEG12-NHS in HBS for 15 min. After the coupling reaction, the glass slides were washed with H_2O , MeOH and EtOH. The DBCO moiety was clicked with a 1 mM solution of Azido-HaloTag Ligand (click-HTL)^[129] in DMF for 2 h and washed with DMF and EtOH. After drying in a nitrogen stream, the unprotected surface of the glass slides between the aminosilane nanodots was backfilled with a PLL-PEG-OMe solution in HBS buffer (2 mg mL^{-1}) for 10 min and washed with fresh MilliQ water. For protein immobilization, the slides were incubated with HBS buffer containing 200 nM HaloTag-mEGFP for 5 min and then washed repeatedly with HBS. The obtained samples were stored in HBS before TIRFM imaging.

3.5.5 HaloTag-dDARPin functionalization of BSA-HTL patterns

BSA-HTL patterned samples were washed with water and sandwiched with 25 μl DARPin-R7-(GSGSD)₃-HaloTag-DARPin-R7-H8 (14 μM) with 10 % FBS for 1 h. The samples were then washed with water and placed in HBS until further use.

3.5.6 Fluorescent labeling of BSA-HTL/BSA-HTL-dDARPin patterns

BSA-HTL patterns were labeled with different concentrations of HaloTag-mEGFP or tagless-mEGFP at RT, repeatedly washed with water and placed in PBS. For every dDARPin experiment, 10 % FBS was added to the tagless-mEGFP as an additional blocking agent.

Table 3: Overview of mEGFP labeling of BSA-HTL and BSA-HTL-dDARPin patterns. Patterned substrates were incubated with a differently tagged mEGFP under the mentioned conditions.

| Patterned substrate | Conditions | Fluorescent protein |
|------------------------------------|--------------------------|---------------------|
| BSA-HTL | 10 min, 200 nM | HaloTag-mEGFP |
| BSA-HTL/BSA-TexasRed | 5 min, 100 nM | HaloTag-mEGFP |
| BSA-HTL-dDARPin | 10 min, 200 nM, 10 % FBS | tagless-mEGFP |
| BSA-HTL-dDARPin (graphene surface) | 5 min, 200 nM, 10 % FBS | tagless-mEGFP |

3.5.7 Fluorescent labeling of PLL-PEG-bt

PLL-PEG-bt patterns were labeled with 20 nM SAV-ATTO 655 in HBS for 1 min at RT, washed with water at least three times and placed in PBS.

3.6 Cell culturing

3.6.1 Transformation

For amplification purposes, DH5 α competent cells were thawed and incubated with 1-2 μ l plasmid (concentrations varied between 500 ng/ μ l to 3000 ng/ μ l) of interest for 30 min on ice. Then the cells were heat-shocked at 42 °C for 1 min and put on ice for an additional 2 min. To the mixture, 350 μ l LB medium was added and incubated while gently shaking for 1 h at 37 °C. From this mixture, 100 μ l were spread over a pre-heated agar plate (ampicillin) and placed into an incubator (37 °C) overnight. One of the grown colonies was picked and transferred into the remaining LB medium (\approx 250 μ l) with ampicillin. The flask was placed into a shaker at 37 °C and left for \approx 16 h. The plasmid was harvested with the NucleoBond Xtra Midi Kit according to the instructions given. Concentration was measured *via* the spectral photometer NanoDrop.

3.6.2 Transfection

Transient transfection was carried out by calcium phosphate precipitation or *via* a PEI transfection protocol.

HeLa (wt) cells were plated onto a 6 cm petri dish and grown overnight.

For calcium phosphate precipitation, 50 μ l CaCl₂ was added to the chosen plasmid (Table 4) and diluted with water to an overall volume of 500 μ l. The plasmid-solution was added dropwise to 500 μ l of stirring HBS and transferred to the seeded HeLa cells.

For PEI transfection, the chosen plasmid was added to 300 μ l NaCl, vortexed and mixed with 10 μ l PEI. After a 15 min incubation time at RT, the mixture was transferred to the seeded HeLa cells.

Table 4: Overview of the employed plasmid, transfection methods for each experiment and plasmid amount for each transfection.

| Experiment name & used plasmids | Transfection method | Amount of plasmide |
|--|----------------------------|-------------------------------------|
| <u>BSA-HTL IFNAR2</u> pSems-HaloTag-mEGFP-IFNAR2 | Calcium phosphate | 12 μ g |
| <u>BSA-HTL-dDARPin-Lrp6</u> pSems-mEGFP-hLrp6 | PEI | 5 μ g |
| <u>BSA-HTL-dDARPin-Optogenetics</u> pSems-fSnap-Sspb-R73Q pSems-H10-GFP-TMD-iLID | Calcium phosphate | 2.7 μ g 1.5 μ g |
| <u>BSA-HTL-dDARPin-Axin1</u> pSems-mEGFP-hLrp6 pSems-linker-fSnap-Fzd8 pSems-TMD-tandem mCherry-Axin1 | Calcium phosphate | 5 μ g 5 μ g 5 μ g |
| <u>BSA-HTL-dDARPin-Dvl2</u> pSems-mEGFP-hLrp6 pSems-linker-fSnap-Fzd8 pSems-leader-tandem mCherry-Dvl2 | Calcium phosphate | 5 μ g 5 μ g 5 μ g |
| <u>BSA-HTL-dDARPin-β-Catenin</u> pSems-mEGFP-hLrp6 pSems-linker-fSnap-Fzd8 | PEI | 5 μ g 5 μ g |

After 2-3 h for the PEI transfection and 6-8 h for the calcium phosphate transfection, respectively, the cells were washed twice with PBS, refilled with medium and placed into the incubator overnight.

3.6.3 Cell experiments

Transfected HeLa cells were detached from the dish by treatment with Trypsin/EDTA and seeded on a prepared coverslip in different concentrations. The elapsed time between seeding and

measuring samples varied (see Table 5). For live-cell TIRF analysis, glass slides were clamped onto a TIRFM sample holder and 500 μ l MEM ++ medium without indicator was added.

Table 5: Overview of all cell experiments in correspondence with their resting time before imaging or further processing.

| Experiment name | Elapsed time before imaging/processing |
|---|--|
| BSA-HTL IFNAR2 | 18 h |
| BSA-HTL-dDARPin-Optogenetics | 18 h |
| BSA-HTL-dDARPin-Axin1 | 7 h |
| BSA-HTL-dDARPin-Dvl2 | 7 h |
| BSA-HTL-dDARPin-β-Catenin | 8 h |

3.6.4 Protein labeling

Protein labeling in live cells was performed at 37 °C under different conditions (see Table 6). Afterward, the samples were washed with PBS at least two times and resuspended in medium.

Table 6: Overview of all transiently transfected cell experiments stained with dye labeled proteins after seeding the cells on the surface under the given conditions.

| Experiment name | Staining conditions |
|---|--|
| BSA-HTL IFNAR2 | 10 nM IFN α 2-ATTO 655, during microscopy |
| BSA-HTL-dDARPin-Optogenetics | 50 nM MAP 555, 30 min |
| BSA-HTL-dDARPin-Axin1 BSA-HTL-dDARPin-Dvl2 | 100 nM, fSnap-DY 647, 30 min, |
| BSA-HTL-dDARPin-β-Catenin | 100 nM, fSnap-DY 549, 30 min, |

3.6.5 Fixation

Prepared samples were fixed with 1 ml 4 % PFA (paraformaldehyde) in HBS for 15 min at RT. The fixation mixture was then siphoned off and the glasses were washed with PBS three times for 5 mins each. If the sample was not immediately used, fixed cells could be stored at 4 °C in PBS for up to a week.

3.6.6 Immunostaining

Fixed cells were subjected to 1 % v/v solution of Triton-X in PBS for 10 min, washed three times with PBS and backfilled with a 3 % m/m solution of BSA in PBS for 30 min. After removing the backfilling solution, 20 μ l of a 1:1000 diluted Antibody (β -Catenin, Mouse AB- Alexa Fluor 647 Conjugate) solution with 3 % BSA was added to the coverslips and topped off with a small piece of parafilm. This package was placed in a loosely closed container and placed into the fridge at 4 °C overnight. The samples were washed three times with PBS and placed into the TIRF sample holder under PBS coverage for fluorescence analysis.

4 Results and discussion

4.1 Substrate design – stamping of heterocyclic silanes and synthetic polymers

Capillary stamping with mesoporous silica stamps was developed with organic solvents as the primary ink component in mind due to the hydrophobic nature of the stamps. During stamping, the main volatile ink component evaporates almost immediately and leaves the reactive/functional non-volatile ink component on the surface behind. Since the stamps act as an ink reservoir, several stamping cycles with no quality deterioration were also possible. This approach was adopted in order to gain access to biofunctionalizable dot arrays.

4.1.1 Stamping of heterocyclic silanes

Cyclic silanes were first used to create a densely packed functionalizable dot array. These heterocyclic silanes undergo a ring-opening reaction upon contact with hydroxyl-terminated surfaces with a minimum of side reactions^[130]. This is an advantage over classical trifunctional silanes (*e.g.*, trichlorosilanes, trialkoxysilanes) which can easily functionalize surfaces due to their high reactivity but often show side reactions such as polymerizations. The result is a silane multilayer on top of the surface. Polymerization of heterocyclic silanes, however, is intrinsically impossible, thus creating only a silane monolayer. The heteroatomic bond -SiX within the cyclic silanes (*e.g.*, X=N, X=S) split in a ring-opening reaction triggered by hydroxyl groups on a silica surface (see Figure 14)^[131]. This reaction is accompanied by a hydrogen transfer from the surface-bound -OH group to the heteroatom, resulting in a silane monolayer with free-standing -XH groups. The reaction of the cyclic silane is driven by the formation of the very stable Si-O bond and the complete loss of any ring strain. It showed similar efficiency compared to click-chemical reactions and was coined a click chemical ring-opening reaction^[17]. Residual water in solution or air moisture leads, in the same way as its trifunctional silane counterparts, to hydrolysis but does not impede on the reactivity of the remaining heterocyclic silane molecules since the hydrolysis products are unable to react with each other or the surface. The hydrolysis products of trifunctional silanes, however, can bind to the surface even after a partial polymerization reaction with each other, thus creating an ill-defined surface^[132].

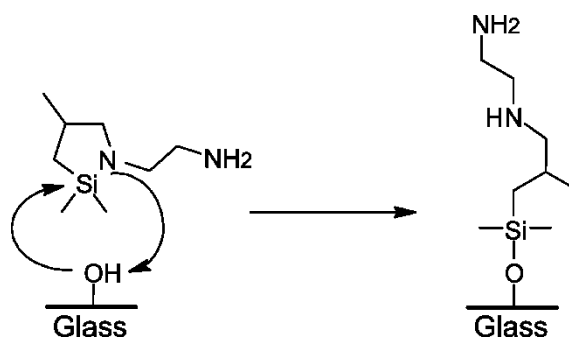


Figure 14: Reaction mechanism of cycloazasilane on the glass surface.

Two heterocyclic silanes (N-aminoethyl-aza-2,2-dimethyl-4-methylsilacyclopentane = azasilane and 2,2-dimethoxy-1-thia-2-silacyclopentane = thiosilane) were chosen for further experiments. Both chemicals were mixed with toluene and stamped on plasma cleaned glass slides for up to 10 consecutive stamping cycles without refilling the stamp with ink (Chapter 3.4.2). To confirm the silane reaction to the surface, cycloazasilane patterns were analyzed by CA measurements and XPS.

Freshly plasma cleaned glass slides have a water contact angle of 0° , which leads to water spreading on their surface. After patterning, the contact angle changed to an average of 72° , suggesting a reaction between the silane and the surface.

For further confirmation, XPS measurements were taken from the silane dot arrays and for comparison also from non-patterned areas on the same sample. Due to the reaction mechanism of cyclosilanes, only a silane monolayer is expected and thus, XPS spectra at a low electron take-off angle of 15° were taken. The low take-off angle increases the sensitivity for surface-bound atoms and assists in the distinguishing process since both silica substrate and silane monolayer share silicon in their atomic structure. The substrate consists of a SiO_2 -network, in which the silicon atom exists in the oxidation state of $4+$, the Si 2p peak of those Si-atoms bound to oxygen appeared at a binding energy (BE) of 103.5 eV in the XP spectrum^[133]. Si-atoms bound to a hydrocarbon group show a shift in binding energy to lower BE values of 102.5 eV due to the less electronegative binding partner^[134]. The measurement of the unfunctionalized surface detected a single peak at 103.3 eV that was assigned to the silica Si-atoms. The spectrum of the silane dot arrays showed a broader peak with a peak maximum at 102.9 eV, indicating the presence of silicon with carbon as their dominant binding partner, which corresponds to silane-Si atoms. The dissection of the spectrum into two separate Lorentzian functions with their maxima set to the values of 103.3 eV (Si 2p peak value of unpatterned glass) and 102.5 eV, respectively, illustrate the contributions coming from silica-Si and silane-Si. The

contributions amounted to 60/40 % (silica-Si/silane-Si) but should not be considered to be the exact atomic ratio since the penetration depth of the low angle XPS is unknown (Figure 15).

With the reaction of the cycloazasilane to the surface, nitrogen should be introduced to samples previously without any nitrogen fraction or contamination. An XPS spectrum of the N 1s region confirmed the presence of a peak for the patterned samples at 400.5 eV and a lack thereof for the bare glass substrates (Figure 15).

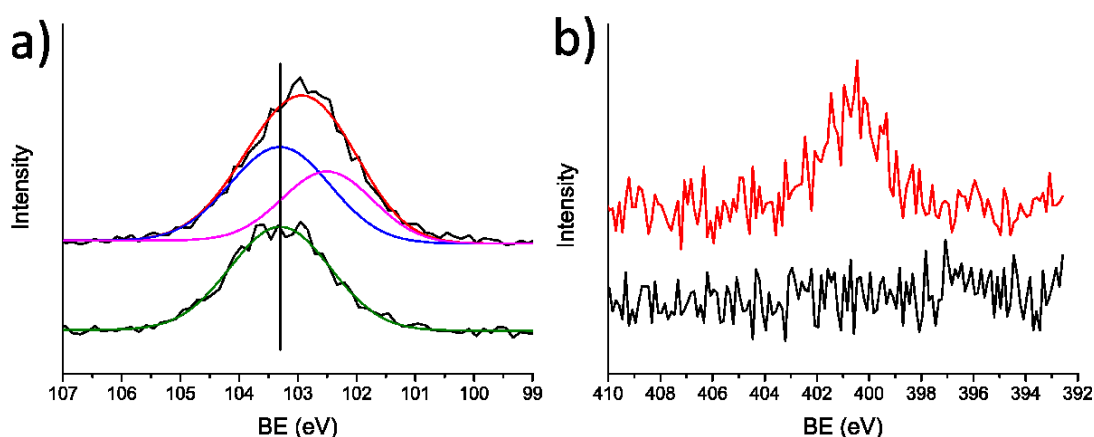


Figure 15: Low angle XPS-spectra of bare glass and cycloazasilane patterned glass slide (curves vertically shifted for clarity). a) bottom: Si 2p spectrum of the bare glass substrate (black) and fitted curve (green). Top: Si 2p spectrum of cycloazasilane patterned surface (black), fitted curves show the different contributions from the silica-Si atoms (blue) and silane-Si atoms (pink) which combined amount to the fitted curve (red), maximum for the silica-Si atoms at 103.3 eV highlighted with a black bar to indicate the shift in BE. b) N 1s spectrum of bare glass (black) and cycloazasilane patterned surface (red).

The last atom used for confirmation of the successful silane reaction was carbon (C 1s). For the non-patterned samples, adventitious carbon at a BE of 285.0 eV was detected^[135]. Adventitious carbon is also present in the patterned samples, but due to the introduction of carbon with more electronegative binding partners by the silane, a peak shift to higher BE can be expected. The spectrum obtained from the silane dot arrays showed a broader peak with a shoulder at 286.7 eV, see Figure 16. It was assumed that carbon atoms in the vicinity of nitrogen (α -position) contribute to the peak shoulder due to its more electronegative binding partner, while every other carbon atom was handled as adventitious carbon. Under this condition, 38 % of the relative peak area should be a contribution of carbon in α -position to nitrogen since 3 out of the 8 carbon atoms in the silane are bound to a -NH/-NH₂ group. The remaining 5 carbon atoms are in a C-CH_x, or -Si-CH_x bond and should make up 62 % of the relative peak area. A fit of two Lorentzian functions, with their respective maxima set to 286.7 eV and 285.0 eV, resulted in a ratio of 28 % to 72 %. Considering the presence of adventitious carbon and its impact on the

peak at lower BE, the result stands in reasonable agreement with the assumed atomic number ratio.

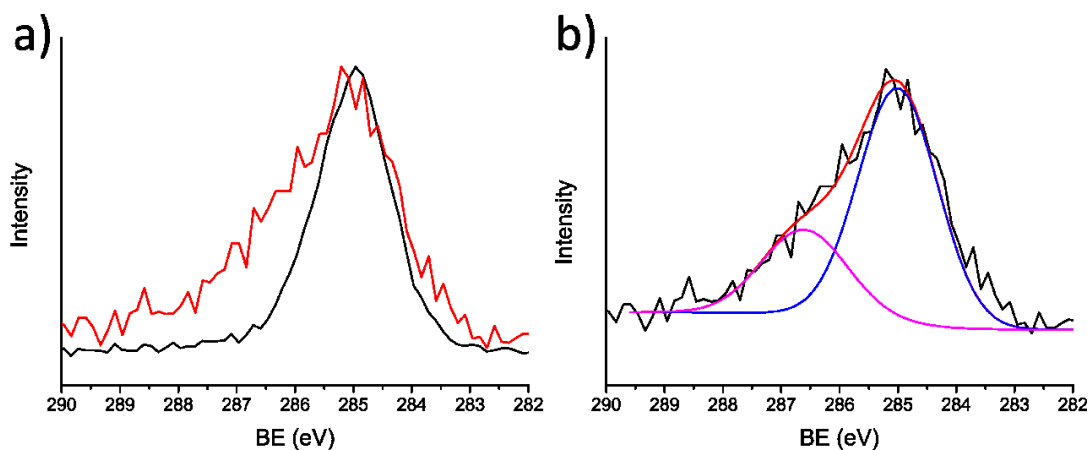


Figure 16: Low angle XPS-spectra of bare glass and cycloazasilane patterned glass slide. a) C 1s spectrum of the bare glass substrate (black) and cycloazasilane patterned surface (red). b) Fitted C 1s spectrum of cycloazasilane patterned glass surface (red) showcasing the contributions of carbon bound to nitrogen (pink) and the mixture of adventitious carbon with remaining C-CH, -Si-CH carbon atoms of the silane (blue).

The results from the contact angle and the XPS measurements combined substantiate the successful binding of the aminosilane to the glass substrate during capillary stamping.

4.1.1.1 Fluorescent labeling of cyclosilane dot arrays

Stamping from toluene allowed to perform up to 10 stamping cycles without reloading of the ink and with only a slight deterioration of the pattern quality. It is noteworthy that the whole patterning procedure was done by hand without any additional control over contact pressure or environment (*e.g.*, temperature, humidity). The stamp-substrate contact time was not measured but kept similar in the range of 1-2 s. It is clear that the overall procedure is very robust against environmental factors and easy to reproduce without any complex machinery.

First, aminosilane dots arrays were labeled with ATTO 647 NHS and imaged with TIRFM, thiosilane dots with ATTO 655 maleimide, respectively (Figure 17).

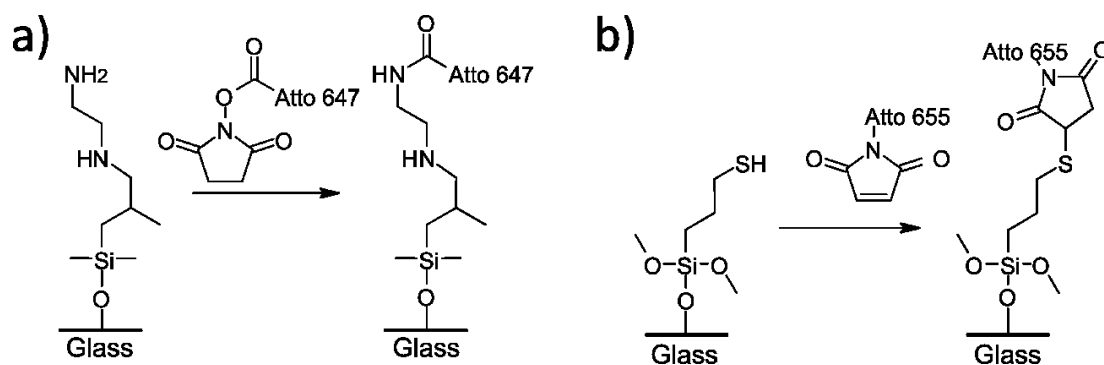


Figure 17: Reaction mechanism of cycloasilanes with labeled fluorescent dyes. a) Labeling of cycloazasilane with ATTO 647 NHS. b) Labeling of cyclothiosilane with ATTO 655 maleimide.

Fluorescence measurements for biological application should exhibit high fluorescence intensities and high signal-to-noise ratios. Hence the contrast between the dye-labeled silane dots and the surrounding area was determined (Figure 18).

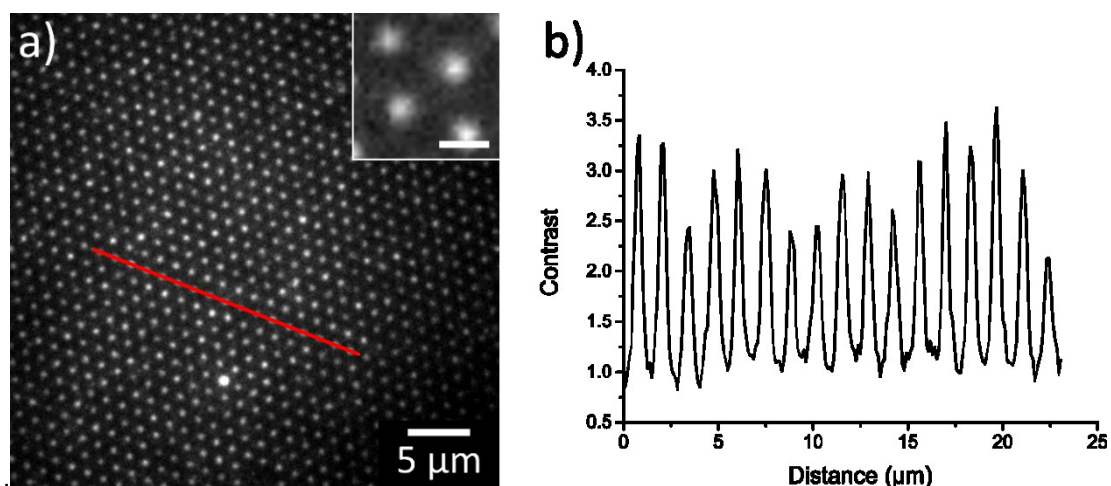


Figure 18: Contrast measurements of dye-labeled cycloazasilane patterns. a) TIRFM image of ATTO 647 labeled cycloazasilane patterns (inset scale bar 1 µm). b) Plotted contrast measurement is taken from the red line in panel (a).

The result was a contrast of ≈ 3.2 . It should be noted that the experiment was performed without any kind of backfilling for the non-patterned area. Generally, treatment with a blocking agent helps to increase the contrast since it prevents non-specific binding of the molecule of interest to the substrate. This was especially necessary while working with proteins or cells.

The dye-labeled aminosilane dot arrays were used to determine the actual size of each spot. With the nearest neighbor distance of ≈ 1.3 µm, each is far enough apart from one another to be easily distinguished under standard TIRFM imaging conditions. However, the actual dot was distorted by a series of factors summed up in the point spread function (PSF) of the system. In

order to gain a sharper image with more defined features, the PSF needs to be subtracted. Therefore, the raw TIRFM images were deconvolved using the Huygens image processing software that takes a theoretical PSF into account. The deconvolved images of ATTO 647 labeled aminosilane dot arrays for the 4th and the 10th consecutive stamping cycle are shown in Figure 19. The inset shows a magnified view of a small part of the patterned area.

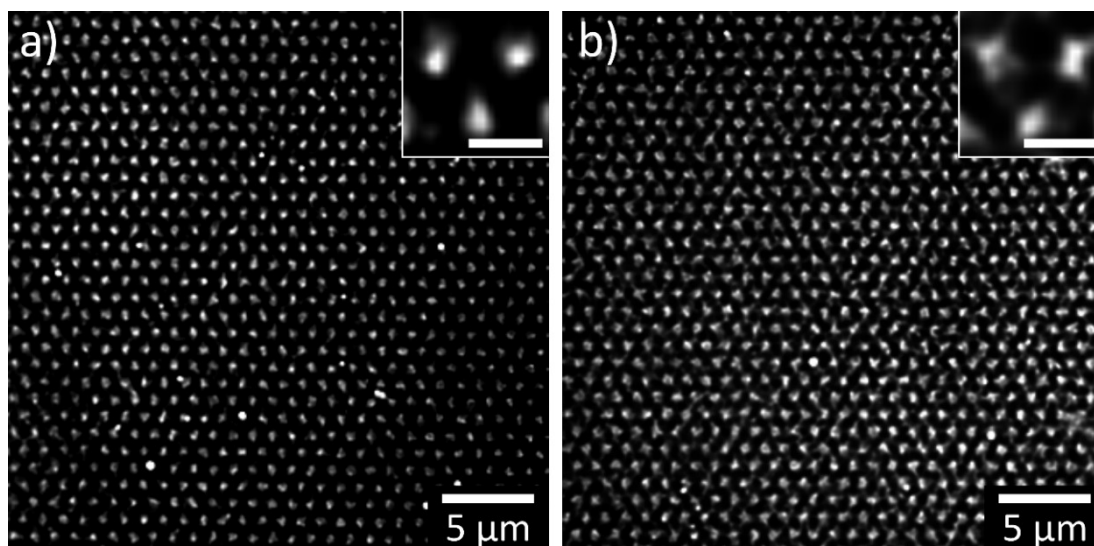


Figure 19: Deconvolved TIRFM images of consecutive stamping cycles of cycloazasilane. a) 4th and b) 10th stamping cycle of cycloazasilane (inset scale bars 1 μm).

In order to calculate the spot area, the images were analyzed with a watershed algorithm. The parameters (seed dynamic, intensity threshold) were selected to match the perimeter of the dots in each of the deconvolved images. The resulting median area for the 4th stamping cycle was $0.250 \mu\text{m}^2 \pm 0.044 \mu\text{m}^2$ and for the 10th stamping cycle, values of $0.342 \mu\text{m}^2 \pm 0.057 \mu\text{m}^2$ were obtained (Figure 20). This marks an increase in area of $\approx 36.8\%$ between the different stamping cycles, which is also apparent in the images. The median distance between the center of each spot was also determined and amounted to $\approx 1.3 \mu\text{m}$. Because the contact elements retain their shape during the consecutive stamping cycles, the median neighbor distance does not change and only varies in the range of $0.1 \mu\text{m}$ to $0.2 \mu\text{m}$ between different stamps. This is due to the different shrinkage during the stamp synthesis.

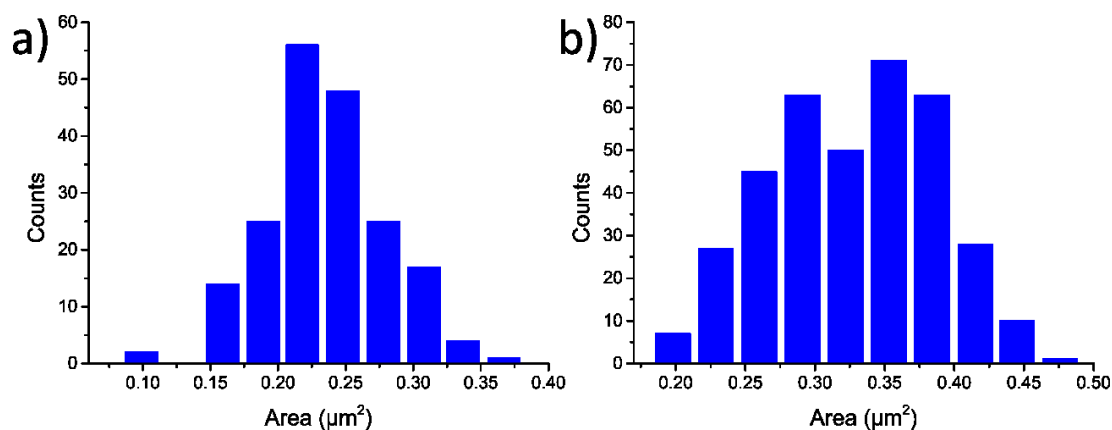


Figure 20: Frequency density of dot areas of consecutively stamped cycloazasilane patterns. a) 4th and b) 10th consecutive cycle.

Using the same calculation, the frequency density of the dot areas for ATTO 655 labeled thiosilane dots were generated. In Figure 21, the area distribution of the 4th stamping cycle ($0.323 \mu\text{m}^2 \pm 0.086 \mu\text{m}^2$) and the 10th stamping cycle ($0.320 \mu\text{m}^2 \pm 0.083 \mu\text{m}^2$) were summarized.

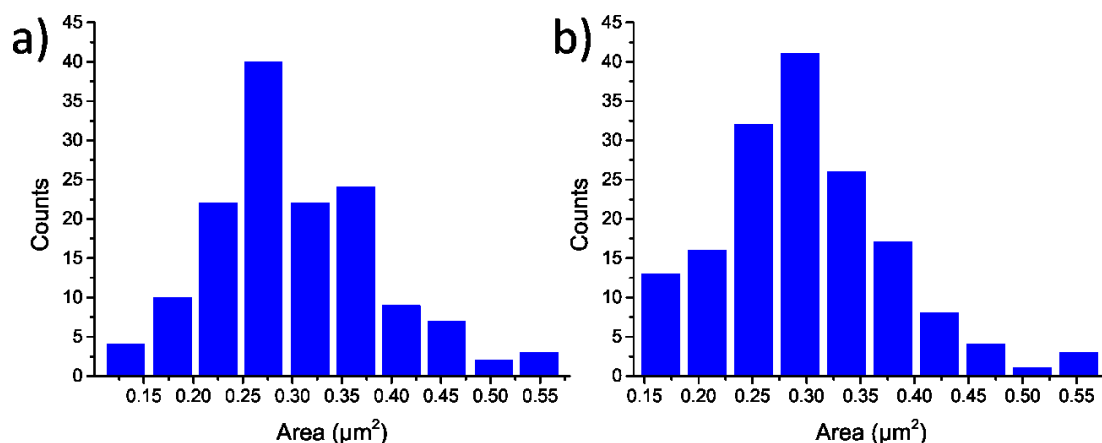


Figure 21: Frequency density of dot areas of consecutively stamped cyclothiosilane patterns. a) 4th and b) 10th consecutive cycle.

Similar to the area, the circularity (4th: 0.78 ± 0.14 ; 10th: 0.78 ± 0.16) and aspect ratio (4th: 1.57 ± 0.40 ; 10th: 1.53 ± 0.36) effectively did not change. Compared to the results of the cycloazasilane, the cyclothiosilane shows less desirable values in every measured category. This could be explained by the difference in surface spreading. Cycloazasilane patterns exhibit a CA of $\approx 72^\circ$, while cyclothiosilane exhibits a CA of $\approx 63^\circ$. A higher CA hints towards smaller dot sizes and possibly also a more rounded shape. However, the unchanging data gathered from the cyclothiosilane experiment suggests that the change in diameter and slight deterioration of the pattern in the cycloazasilane experiments stems from the manual stamping operation and not the degradation of the stamp during successive stamping cycles.

4.1.2 Polystyrene brushes by surface-initiated polymerization

The terminal functional group of the aminosilane dots was also used for more complex chemical functionalizations, one of which was the ARGET-ATRP (Activators regenerated by electron transfer – atom transfer radical polymerization) of styrene^[136]. ATRP is a form of living polymerization and a versatile method to polymerize a variety of different monomers. Advantages of this technique are the precise control over the molecular weight coupled with a low polydispersity and the retention of its end chain functionality for further modification. The disadvantages are that the reaction usually requires high amounts of copper catalyst, which is difficult to remove entirely^[137]. As a proof of concept, polymerization of styrene was chosen with an adapted protocol from Li *et al.*^[138].

In this experiment, BIBB was coupled to the terminal amine groups of the aminosilane dots to generate initiation sites for the ATRP. The following polymerization of styrene generated an area of discrete PS brushes on the patterned surface (Figure 22).

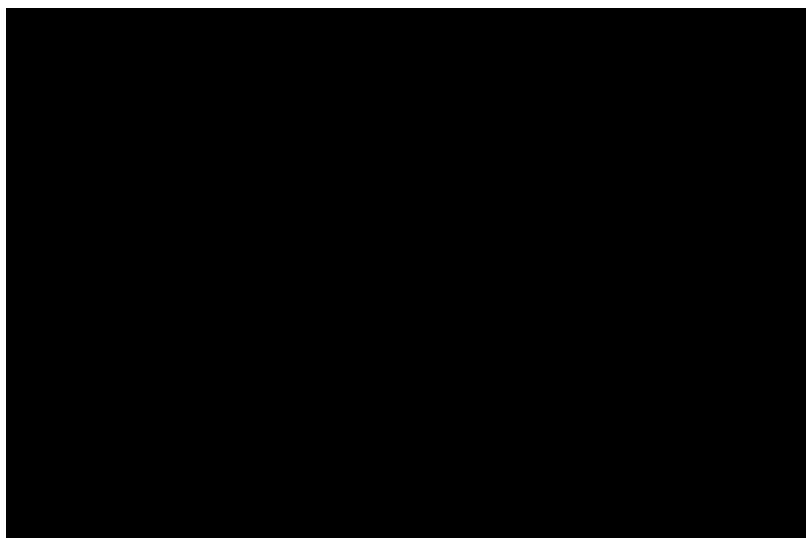


Figure 22: Reaction mechanism of polystyrene brush synthesis on cycloazasilane dot arrays.

The samples showed interference colors indicating periodic structures with pitches below the micrometer regime due to the diffraction of visible light. The brushes were also high enough to be visualized by SEM (Figure 23). The image shows a uniform area with discrete PS brushes matching the length scales of the contact elements from the stamp with a median distance of $\approx 1.2 \mu\text{m} - 1.3 \mu\text{m}$. This was confirmed by AFM measurements, and an expected diameter of $\approx 700 \text{ nm}$ and a height of $\approx 15 \text{ nm}$ for the imaged area was obtained.

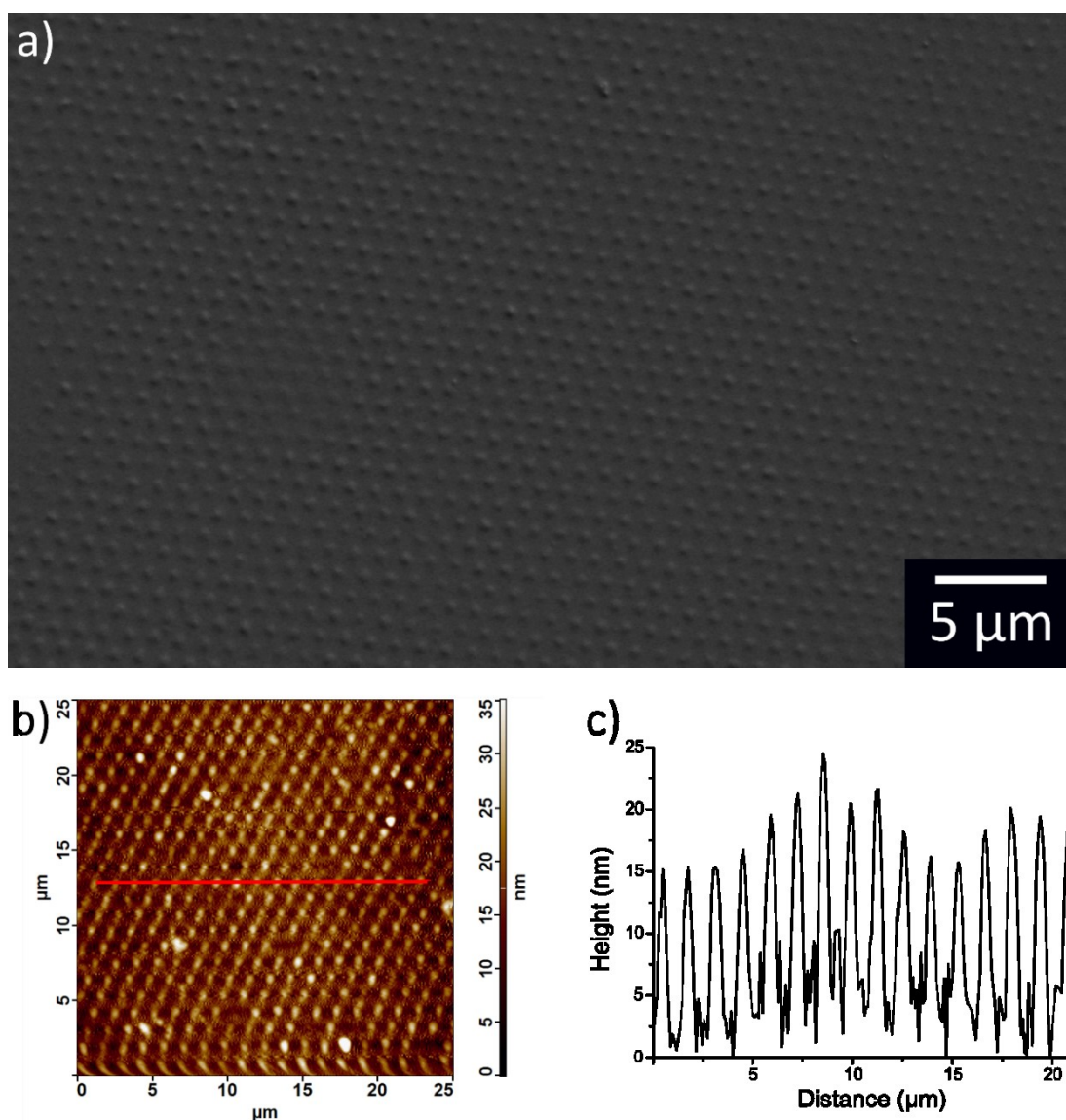


Figure 23: Functionalization of cycloazasilane dot arrays with polystyrene brushes *via* ARGET ATRP. a) SEM image of polystyrene brush functionalized dot array. b) topographical AFM image of PS brush array. c) Topographic profile along the line in panel (b).

It is noteworthy that no backfilling was needed during the whole polymerization, suggesting a well-defined patterning of the glass slides.

To prove the preservation of the functional halogen end group on the polymer brushes and the possibility of a bio-functional modification, the bromide group was exchanged with an azide group (chapter 3.5.3). The fluorescent dye (DBCO-Cy5) was coupled to the polymer brushes *via* copper-free click chemistry, included a backfilling step with PLL-PEG-OMe and was visualized with TIRFM. In Figure 24, the resulting image can be seen.

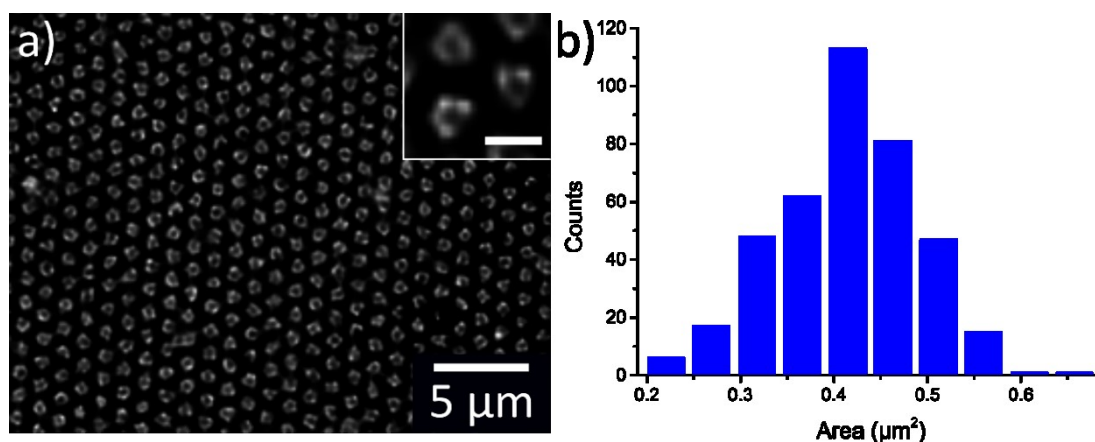


Figure 24: Dot analysis of DBCO-Cy5 labeled PS brushes. a) deconvolved TIRFM image (inset scale bar 1 μm). b) Frequency density of dot areas of PS brush arrays.

The spot area of the fluorescently labeled polymer brushes amounted to $0.440 \mu\text{m}^2 \pm 0.076 \mu\text{m}^2$ and aligned with the measured diameter by AFM. Therefore, cycloazasilane dot arrays were successfully used as starting sites for ARGET-ATRP, and the polymerization of styrene yielded distinct PS brushes, adapting the stamped pattern, with further modification possibilities. Nevertheless, compared to the only dye-labeled dots, the increase in diameter of 38 % shrinks the free space between the brushes by a considerable margin. This rise in diameter can be solely attributed to the nature of the PS brushes, which take up more space due to their random coil structure. With the dye-labeled PS brushes, a contrast of ≈ 1.3 could be achieved (Figure 25).

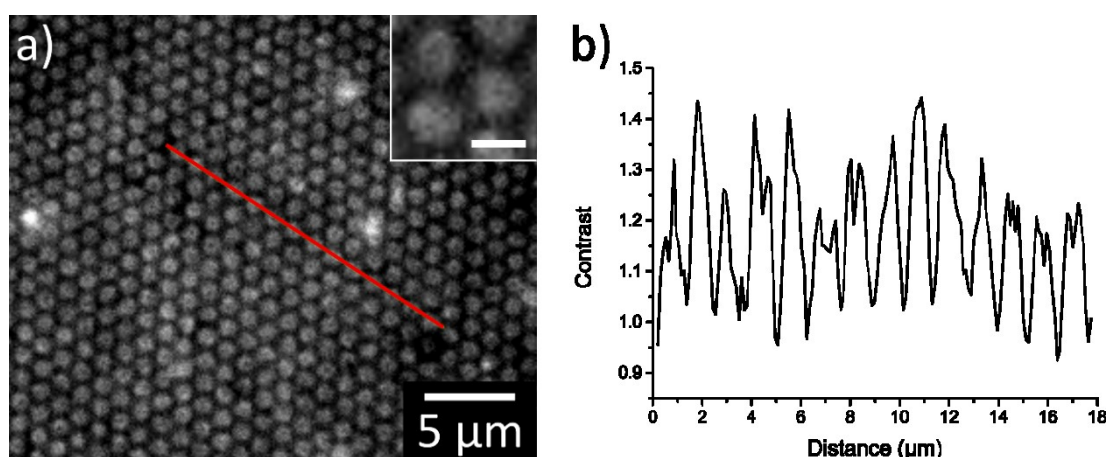


Figure 25: Contrast measurements of dye-labeled PS brushes. a) TIRFM image of DBCO-Cy5 labeled PS brush arrays (inset scale bar 1 μm). b) Plotted contrast measurement is taken from the red line in panel (a).

4.1.3 Biofunctionalization of cycloazasilane dot arrays with HaloTag-ligand

A direct approach to bio-orthogonal functionalization of the aminosilane dot arrays was put into practice by immobilizing site-specific proteins *via* the HaloTag with an about tenfold

improved spatial resolution compared to conventional soft lithography. NHS activated DBCO-PEG molecule was coupled with the amine group of the silane dot arrays and then further functionalized with azido-HaloTag-Ligand (click-HTL) *via* copper-free click-chemistry (Figure 26). The sample was backfilled with PLL-PEG-OMe to prevent non-specific binding of proteins to the bare glass substrate and helped to increase the resulting signal-to-noise ratio. HaloTag-mEGFP was used to label the HTL functionalized silane dots and TIRFM was performed to visually confirm the successful modification.

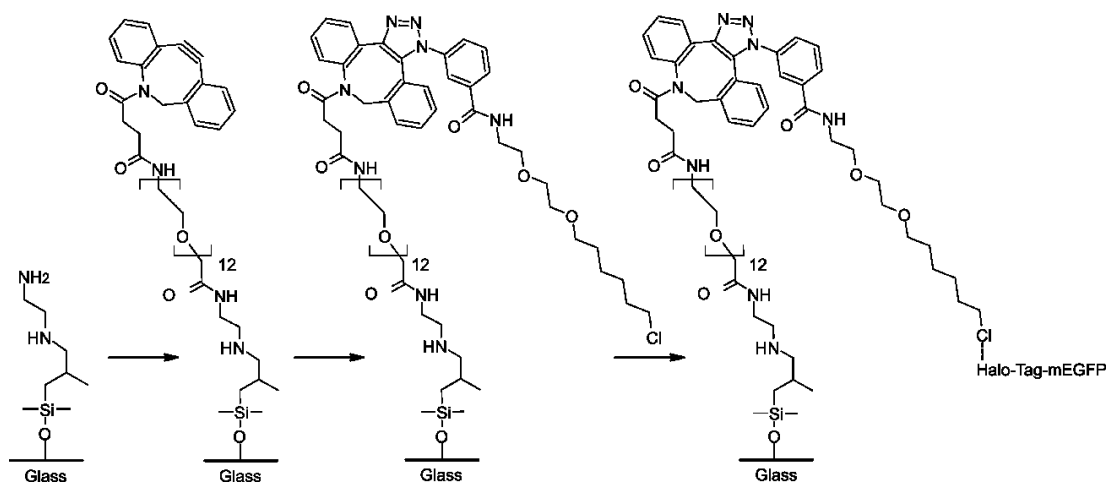


Figure 26: Reaction mechanism of Halo-Tag-mEGFP modification of cycloazasilane patterns.

Surface binding of HaloTag-mEGFP to click-HTL was calculated using a pseudo-first-order model according to

$$\Gamma = 1 - e^{-k_{on}ct} \quad (3)$$

where Γ (ng/mm²) is the surface load of HaloTag-mEGFP, c (mol/l) the concentration of HaloTag-mEGFP in solution and t (s) the incubation time. We set the on-rate constant of HaloTag-mEGFP binding to click-HTL k_{on} (M⁻¹s⁻¹) on to the previously determined value of $4 \cdot 10^4$ M⁻¹s⁻¹[129]. Hence, the adopted concentration and incubation time of HaloTag-mEGFP in this experiment guaranteed a 91 % binding of Halo-Tag-mEGFP to the immobilized click-HTL spots on the pattern. The resulting images (Figure 27) showed a contrast of about 1.6.

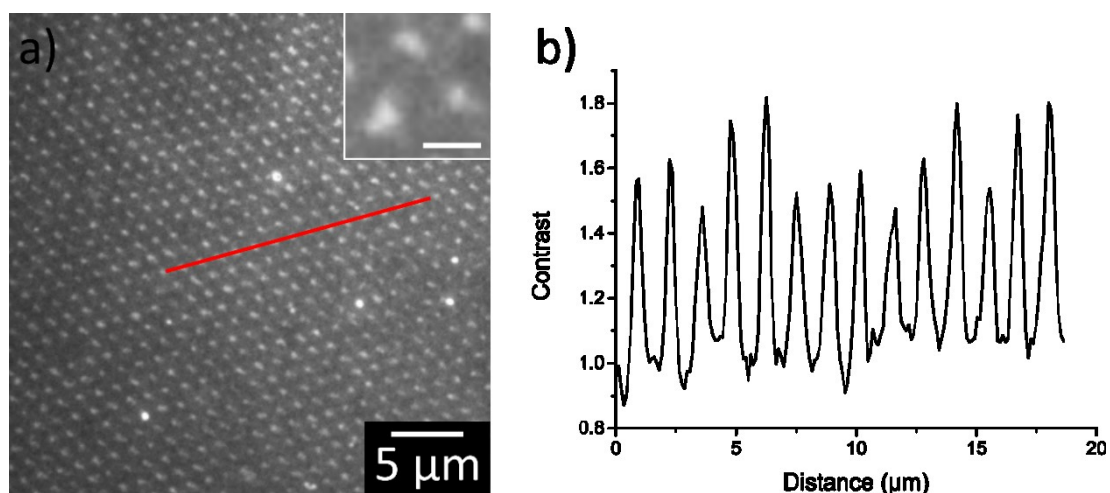


Figure 27: Contrast measurements of HaloTag-mEGFP functionalized arrays. a) TIRFM image (inset scale bar 1 μm). b) Plotted contrast measurement is taken from the red line in panel (a).

In Figure 27, the deconvolved image of aminosilane nanodots functionalized with HaloTag-mEGFP can be seen. The calculated median area from the deconvolved images (Figure 28) resulted in $0.134 \mu\text{m}^2 \pm 0.046 \mu\text{m}^2$ with the nearest neighbor distance of $\approx 1.3 \mu\text{m}$. The spot size decreased compared to the only dye-labeled silane spots ($\approx 0.110 \mu\text{m}^2$). The leading cause for this shift in area size is most likely the complex modification of the spots, which involved three reaction steps. Although robust chemical reactions with usually high yields (NHS-chemistry, copper-free click chemistry) were employed, the result was a smaller area and a skewed shape of each dot. The use of a backfilling agent could be the reason for partially blocking the outer perimeter of the spots for the GFP. As a consequence, a low circularity of 0.70 ± 0.18 and a high aspect ratio of 2.38 ± 0.72 were obtained.

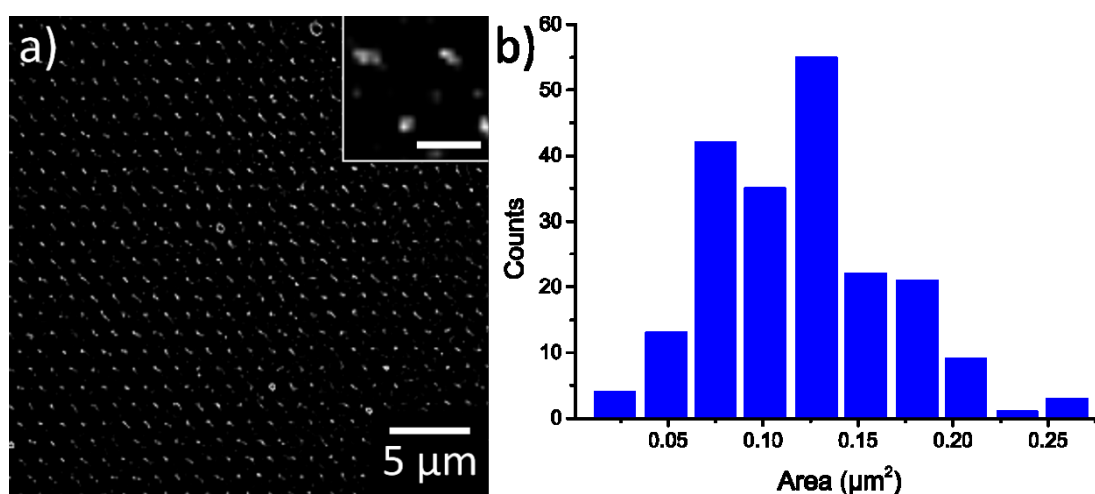


Figure 28: Dot analysis of HaloTag-mEGFP functionalized arrays. a) deconvolved TIRFM image (inset scale bar 1 μm). b) Frequency density of dot areas of HaloTag-mEGFP dot patterns.

While it was proven that a biorthogonal functionalization of aminosilane dots was possible, the obtained contrast was not good enough to proceed with *in vitro* cell experiments without further improvements.

4.1.4 Stamping of biotinylated Poly-L-Lysine

PLL-PEG is often used to functionalized glass surfaces because the positively charged PLL-backbone sticks to the partially negatively charged glass surface effectively, and the PEG side chains prevent unwanted interactions of the analyte with the surface. In addition, the polymer can be modified with functional end groups (*e.g.*, HTL), which can guarantee biorthogonal reactions. The concept of printing PLL-PEG-HTL is already established in combination with μ CP and was adapted for capillary stamping.

PLL-PEG-bt was stamped from EtOH on DMDCS silanized glass. The surface modification prior to stamping was used to prevent the spreading of the ink droplets and therefore increase the overall pattern quality. After fluorescently labeling the slides with SAV- ATTO 655, TIRFM was conducted.

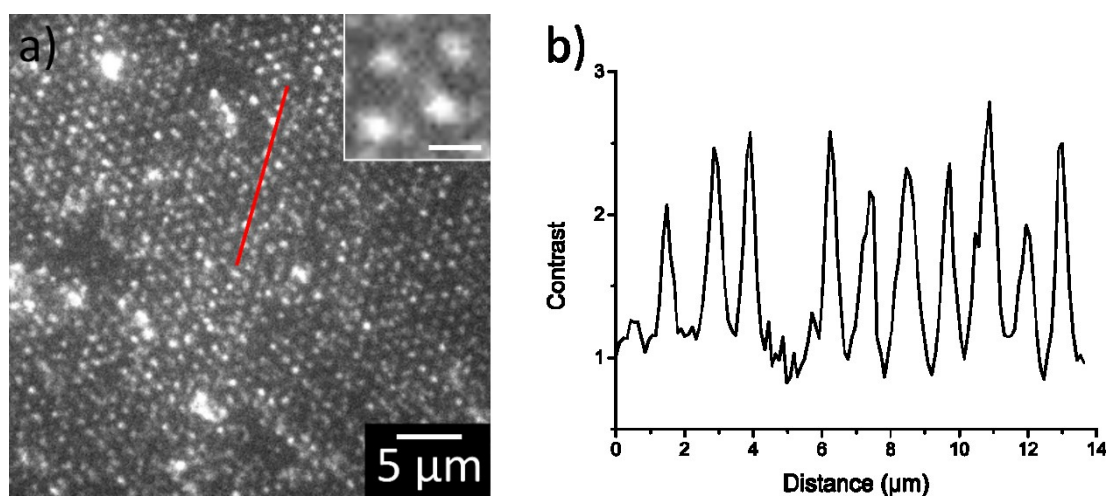


Figure 29: Contrast measurements of PLL-PEG-bt patterned surface a) TIRFM image (inset scale bar 1 μ m). b) Plotted contrast, measurement taken from the red line in panel (a).

The resulting contrast of about ≈ 2 , combined with a lot of defects and impurities of the pattern, was not suitable for any further application (Figure 29). It was also impossible to stamp several cycles consecutively with similar results. The second cycle already showed no patterned area anymore, which suggests that the polymer only adsorbs to the surface of the silica stamp and does not infiltrate the porous material. Thus, after one stamping cycle, most of the material is transferred to the glass slide, and the stamp cannot be used without refilling the ink.

4.2 Substrate design – stamping of proteins

Established lithography methods often directly stamp biomolecules from aqueous solutions. μ CP, for example, is used for a wide variety of biological samples^[9]. The direct patterning approach of protein or binding partner of interest circumvents the need for further functionalizations and desirably simplifies the experiment. Capillary stamping with mesoporous silica stamps has only been used with organic solvents, but for the direct printing of proteins, it is necessary to have an ink based on an aqueous solution because organic solvents denature proteins. At first, the mesoporous silica stamps are hydrophobic due to their methyl-terminated surface but can be infiltrated with water over a longer exposure time. About 1 h later, the fully immersed stamp replaced its previous solvent ethanol with water, which is noticeable when the silica stamp sank in the solution instead of floating on top. Another noticeable difference that speaks for the successful solvent exchange is the drastically prolonged time in which the stamp can stay intact outside of its solvent without drying out. The porous silica material tends to break apart due to internal stress and capillary forces when volatile solvents such as toluene evaporate. Water-soaked silica stamps stayed intact for several hours until the solvent partially evaporates and the stamp shrank to an unusable size. As a result, it is possible to stamp proteins with mesoporous silica stamps out of an aqueous solution.

4.2.1 Stamping of labeled streptavidin

A mixed strategy between surface modification and highly specific biomolecular interactions was employed to test the ability to print proteins with porous silica stamps.

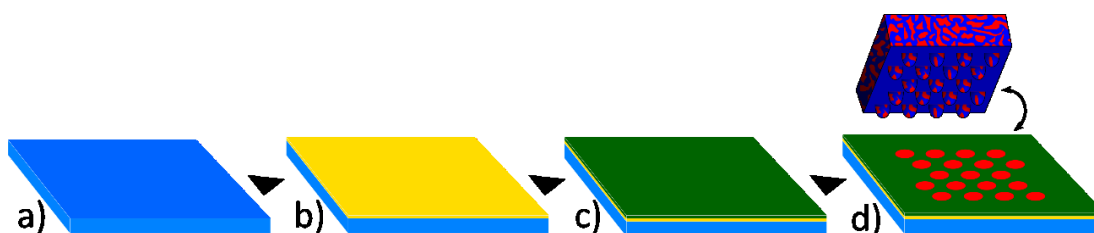


Figure 30: Schematic of processing and patterning PEG-bt coated glass slides with SAV-Cy5 a) bare glass substrate b) silanization with cycloazasilane c) coating with NHS-PEG-OMe/NHS-PEG-bt d) stamping of SAV-Cy5 with porous silica stamps soaked in HBS/SAV-Cy5 mixture.

First, the previously used cycloazasilane was used to form a continuous, non-patterned coating (Figure 30b). In the subsequent reaction, the surface was treated with a mixture of NHS-PEG-OMe and NHS-PEG-bt, yielding randomly distributed SAV binding sites (Figure 30c). The ink consisted of a dye-labeled SAV-Cy5 in HBS (Figure 30d). The bt-SAV interaction is highly

specific and shows swift reaction times ($K_D \approx 10^{-15} \text{ M}^{[139]}$). Both parameters are substantial for achieving a regular pattern and a high contrast.

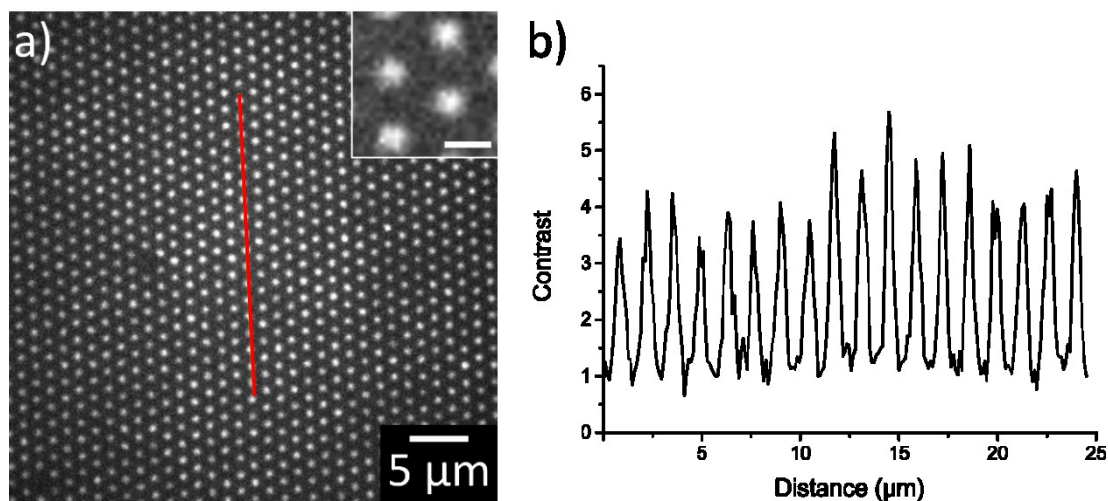


Figure 31: Contrast measurements of SAV-Cy5 patterned cycloazasilane-PEG-bt surface. a) TIRFM image (inset scale bar 1 μm). b) Plotted contrast, measurement taken from the red line in panel (a).

For this configuration, a contrast of ≈ 4 could be achieved (Figure 31). The overall pattern fidelity was also excellent and proved that it is possible to print biomolecules *via* capillary stamping. The result also suggests the transfer of intact and bioactive SAV because with loss of its structure, binding to biotin would not be possible and precise patterns would not be obtainable. Only physio-adsorbed molecules would have been removed during the subsequent washing step due to the protein-repellent properties of the PEG-grafted surface.

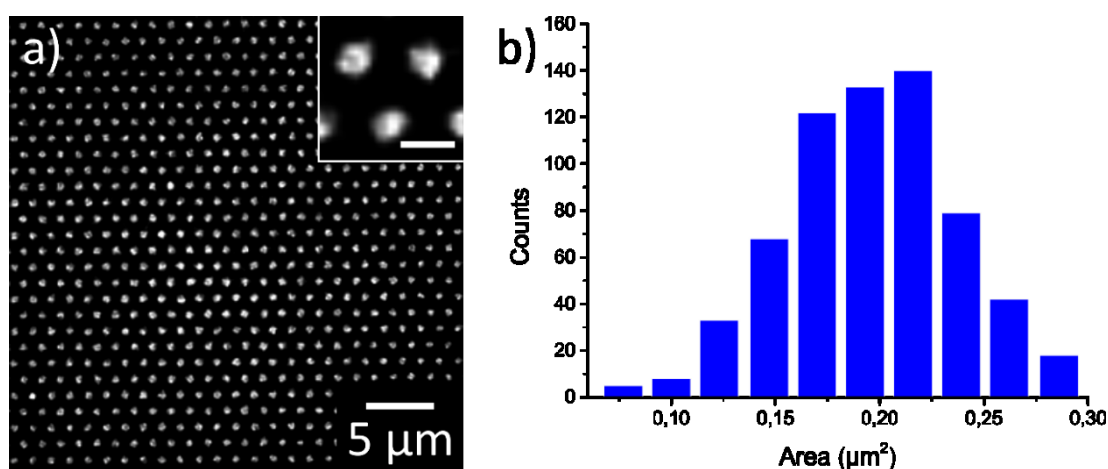


Figure 32: Dot analysis of SAV-Cy5 patterned cycloazasilane-PEG-bt surface. a) deconvolved TIRFM image (inset scale bar 1 μm). b) Frequency density of dot areas of SAV-Cy5 patterns.

After deconvolution of the image, a mean dot area acquired from Figure 32 amounted to $0.207 \mu\text{m}^2 \pm 0.039 \mu\text{m}^2$ with a circularity of 0.96 ± 0.056 and an aspect ratio of 1.22 ± 0.14 . Especially overall pattern fidelity, circularity and aspect ratio benefited from the solvent change, several stamping cycles could not be performed anymore. After one cycle, the pattern quality deteriorated drastically, suggesting adsorption of SAV-Cy5 only on the stamp surface, but re-loading the stamp with ink and following stamping was possible. The achieved values in contrast and size warranted a continuation for *in vitro* cell experiments. However, the bt-function is not biorthogonal and cell experiments can suffer from undesirable interactions between the bt-function and naturally occurring binding partners, thus making this setup only applicable in well-defined environments.

4.2.2 Stamping and modification of BSA-HTL

In order to obtain the desired biorthogonality and gain a higher contrast, the printing of modified BSA on hydrophobically coated glass slides was tested. BSA is a robust protein, usually used as a blocking agent for different kinds of surfaces. In its role, it reduces the unspecific binding of proteins of interest^[140]. Due to its application, BSA is known to stick to surfaces very well, especially hydrophobic ones are readily coated. Additionally, it is cheap and available in high purities and can easily be further modified with desired functional groups^[141].

Hydrophobic coatings improve the adsorption speed of BSA and prevent spreading of the water-based ink. Both parameters were substantial for high-quality patterns and small dot sizes. A high surface density helped to increase contrast by supplying more binding sites for reaction partners. Adsorption kinetics and analyte surface loading can be quantified with TIRF-RfS measurements, while hydrophobicity was measured by separate water contact angle experiments (Chapter 3.2.3). In the following chapter, both methods were employed in order to find the ideal surface treatment for BSA adsorption and patterning.

4.2.2.1 TIRF-RfS analysis of silanized surfaces for optimization of BSA adsorption

Since silanization of glass represents an efficient way to change the surface properties from hydrophilic to hydrophobic^[142], several silanes with hydrophobic residues were tested to promote BSA adsorption onto the glass coverslip. The tested silanes can be divided into 2 groups. The first group contains silanes with alkyl chains of different lengths (DMDCS, OTS), the second group utilizes conjugated π -systems to bind BSA (NMMS, DPDCS) and as a reference, hydrophilic pegylated silane (MPEGTMS) was employed (Figure 33).

225 s with a subsequent washing step. For each measurement $t_{1/2}$, the time necessary to gain half of the maximum surface loading was determined to get a qualitative value for the adsorption speed of BSA. The surface load Γ (ng/mm²) was extracted directly out of the spectrum while the association rate constant k_a (M⁻¹s⁻¹) was fitted with the following formula for Langmuir association:

$$\Gamma = \Gamma_{\text{eq}} \cdot (1 - e^{-(k_a \cdot c + k_d)(t-t_0)}) + RI \quad (5)$$

with

$$\Gamma_{\text{eq}} = \left(\frac{k_a \cdot c \cdot \Gamma_{\text{max}}}{k_a \cdot c + k_d} \right) \quad (6)$$

For the analyte concentration c (mol/l), the highest tested concentration for each silane was used. The dissociation rate constant k_d (M⁻¹s⁻¹) was set to 0 with no apparent dissociation for each experiment. The time t (s) was assigned to the endpoint of the timer interval used for fitting the curve and t_0 (s) the starting point, respectively. RI was the bulk refractive index effect.

In Figure 34, the results for the DMDCS and OTS can be seen.

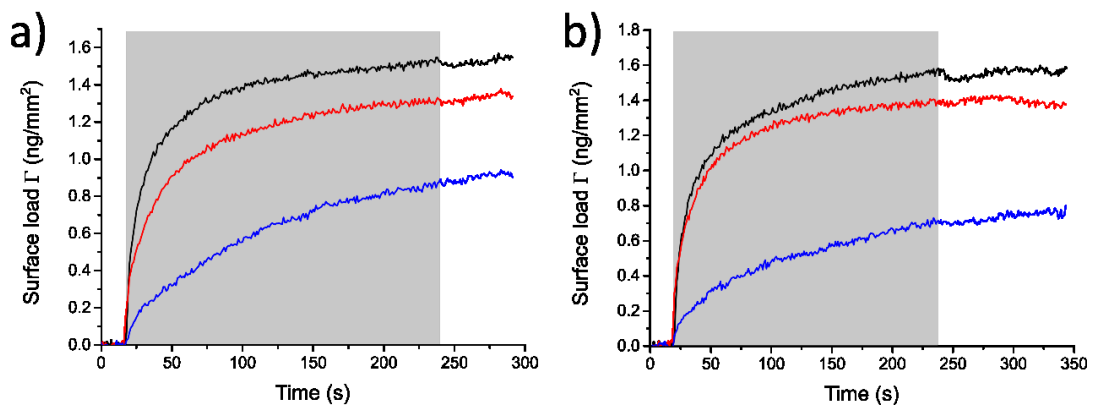


Figure 34: RfS spectra of differently aliphatic-hydrophobic silane coated surfaces with BSA injection (grey bar) and subsequent washing step. a) DMDCS spectrum with different BSA concentrations (1 μM : blue, 5 μM : red, 10 μM : black). b) OTS spectrum with different BSA concentrations (1 μM : blue, 5 μM : red, 10 μM : black).

Both silanes showed similar behavior in their measurements, with a surface load Γ for the highest BSA concentration at ≈ 1.5 ng/mm². The obtained $t_{1/2}$ value for DMDCS was 12 s and 10 s for OTS at the maximum BSA concentration. To put these values into context, a standard

stamping procedure takes $\approx 3-5$ s. Although a precise patterning result is not only reliant on the adsorption speed, since surface properties (*e.g.*, hydrophobicity) certainly play a significant role, faster adsorption is desired to maintain feature sizes and limit unwanted diffusion into the free space between each dot. The fitted k_a value for DMDCS was $1.05 \cdot 10^4 \text{ M}^{-1} \text{ s}^{-1}$ and $9.75 \cdot 10^3 \text{ M}^{-1} \text{ s}^{-1}$ for OTS.

It should be noted that the non-covalent interactions between both of the silanized surfaces and the analyte were strong enough to bind the protein successfully even during the washing step.

The same conditions were chosen for the second silane and the reference. DPDCS had similar results compared to the alkyl silanes with lower loading of 1.2 ng/mm^2 , a slight loss of mass during the washing step (Figure 35b) and a k_a value of $1.44 \cdot 10^4 \text{ M}^{-1} \text{ s}^{-1}$. NMTS proved to be a substantial improvement over the previously tested silanes, see Figure 35a.

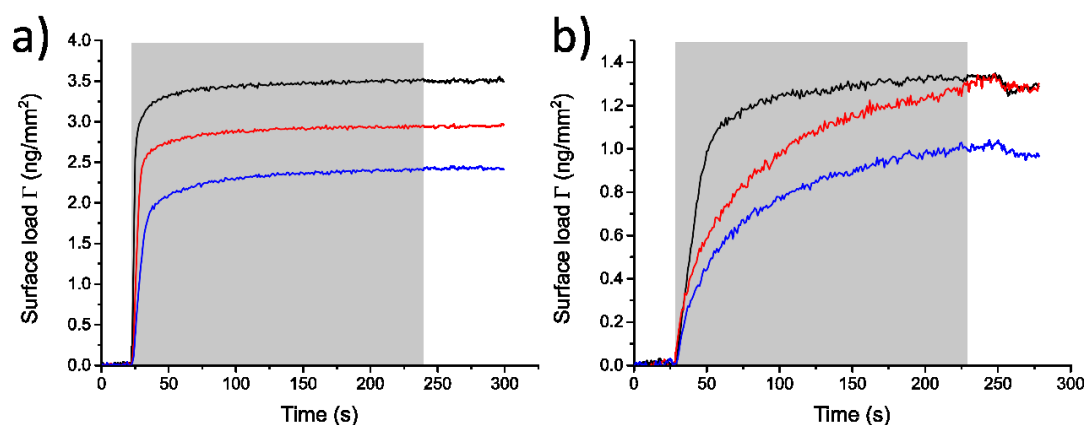


Figure 35: RfS spectra of differently aromatic-hydrophobic silane coated surfaces with BSA injection (grey bar) and subsequent washing step. a) NMTS spectrum with different BSA concentrations ($0.5 \mu\text{M}$: blue, $1 \mu\text{M}$: red, $3 \mu\text{M}$: black). b) DPDCS spectrum with different BSA concentrations ($1 \mu\text{M}$: blue, $3 \mu\text{M}$: red, $5 \mu\text{M}$: black).

The loading capacity of NMTS modified surfaces amounted to 3.5 ng/mm^2 , strikingly at a lower BSA concentration of $3 \mu\text{M}$. The adsorption speed increased drastically and lowered $t_{1/2}$ to ≈ 2.5 s and the k_a value of $2.73 \cdot 10^5 \text{ M}^{-1} \text{ s}^{-1}$ was one order of magnitude higher than any other tested silanized surface. The washing step with HBS did also not lead to any detachment of adsorbed proteins. In Table 7, the $t_{1/2}$ and loading capacities for all measurements can be seen.

Table 7: Summary of $t_{1/2}$, loading capacity Γ and used concentration for tested silanes.

| Name | $t_{1/2}$ | Loading capacity Γ | k_a | Concentration c |
|--------|-----------|---------------------------|---|-------------------|
| DMDCS | 12 s | 1.5 ng/mm ² | $1.05 \cdot 10^4 \text{ M}^{-1} \text{ s}^{-1}$ | 10 μM |
| OTS | 10 s | 1.5 ng/mm ² | $9.75 \cdot 10^3 \text{ M}^{-1} \text{ s}^{-1}$ | 10 μM |
| DPDCS | 13 s | 1.2 ng/mm ² | $1.44 \cdot 10^4 \text{ M}^{-1} \text{ s}^{-1}$ | 5 μM |
| NMTS | 2.5 s | 3.5 ng/mm ² | $2.73 \cdot 10^5 \text{ M}^{-1} \text{ s}^{-1}$ | 3 μM |
| MPEGES | -- | -- | -- | 10 μM |

The NMTS modified surface improved adsorption times. It also gained higher loading capacity at lower concentrations. In comparison, the amount of $\approx 3.5 \text{ ng/mm}^2$ is more than doubled and significantly more than the theoretically calculated value. Stamping benefited from the improvement of both parameters, faster adsorption times lead to more precise patterns and an increase in loading capacity provides more binding sites for future applications.

Since NMTS displayed the most promising results, a binding test was carried out with 10 μM BSA-HTL, 2 μM tagless-mEGFP and 2 μM HaloTag-mEGFP as individual injections separated by washing steps with HBS.

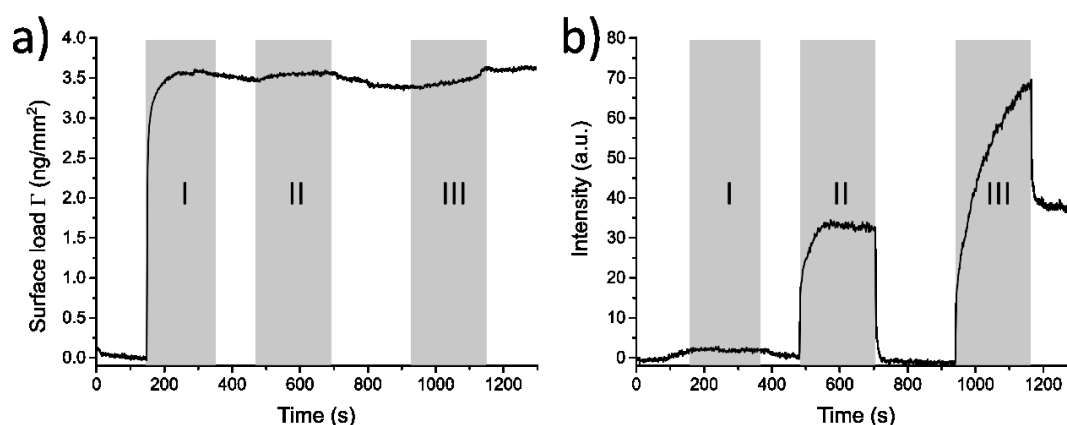


Figure 36: TIRF-RfS analysis of NMTS coated surface with corresponding 10 μM BSA-HTL injection (I) mEGFP injection (II) and mEGFP-HTL injection (III) separated by a washing step with HBS a) RfS spectrum. b) TIRF spectrum.

After the injection of BSA-HTL ($t = 225 \text{ s}$), fast adsorption onto the surface with a surface load of 3.5 ng/mm^2 was visible (see Figure 36a). Compared to the previous RfS measurement on the NMTS modified surface, no apparent difference between unlabeled BSA and BSA-HTL was detected, suggesting similar behavior, which applied for the following washing step with HBS as well. The binding of Halo-Tag fused proteins to BSA-HTL was investigated by injecting

tagless-mEGFP and Halo-Tag-mEGFP sequentially (Figure 36b). With the addition of tagless-mEGFP at $t = 480$ s, a fluorescence signal in the TIRF channel was detected, which immediately dropped to its original value as soon as the injection was stopped ($t = 700$ s). As tagless-mEGFP is not able to bind to BSA-HTL, the obtained signal is washed away with the following HBS washing step. HaloTag-mEGFP was injected at $t = 940$ s, which was accompanied by another spike in fluorescence intensity. The difference in maximum intensity can be attributed to the binding of fused HaloTag-mEGFP to BSA-HTL combined with the background intensity from the solution. During the following washing step, bound HaloTag-mEGFP could not be removed, which is apparent by the remaining fluorescence.

As a reference, the hydrophilic 6-9-pegylated silane was treated in the same way with $3 \mu\text{M}$ and $10 \mu\text{M}$ solutions of BSA. With the injection at $t = 25$ s, there is no detectable rise in the surface load signal. The protein-repellent properties of PEG successfully prevent any adsorption to the surface (see Figure 37).

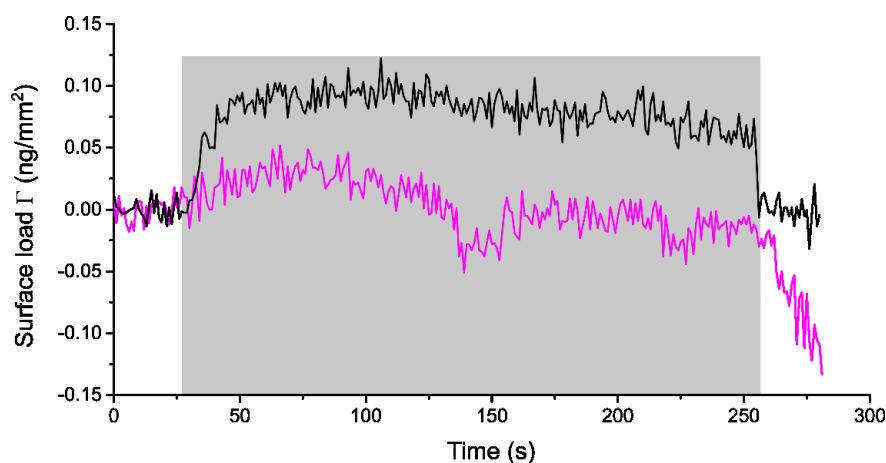


Figure 37: RfS spectrum of MPEGPS coated surface with BSA injection (grey bar) at different concentrations ($3 \mu\text{M}$: magenta, $10 \mu\text{M}$: black) and a subsequent washing step.

4.2.2.2 Stamping of BSA-HTL

Because of the TIRF-RfS results in chapter 4.2.2.1, NMTS was adapted as the standard silanization for any following experiment with BSA-HTL. For stamping, HTL was attached to BSA *via* NHS-Chemistry and a functionalization degree of ≈ 13 HTLs per BSA protein was reached (see Chapter 3.3.5). Water infiltrated mesoporous silica stamps were immersed into a BSA-HTL

solution in HBS and then used to stamp onto NMTS modified glass slides according to chapter 3.3.1. (Figure 38c)

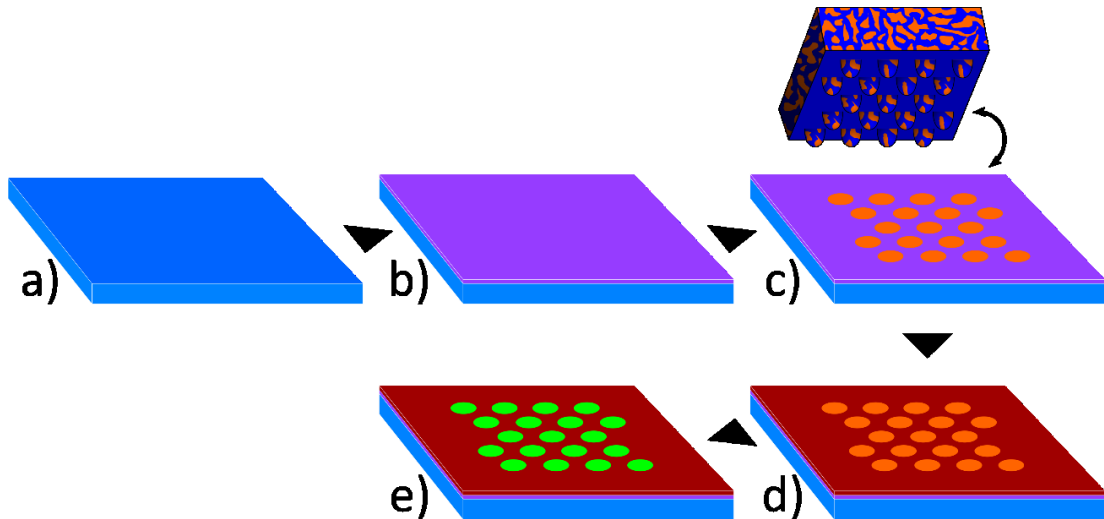


Figure 38: Schematic of processing and patterning NMTS coated glass slides with BSA-HTL a) bare glass substrate b) silanization with NMTS c) stamping of BSA-HTL with porous silica stamps soaked in HBS/BSA-HTL mixture. d) backfilling with 100 % FCS e) staining of the dot array with HaloTag-mEGFP.

As a backfilling reagent, 100 % FCS was used (Figure 38d), as it contains BSA as a major component alongside similar proteins. It sticks to hydrophobic surfaces very well and blocks it for other proteins or dyes. BSA-HTL patterns were then stained with HaloTag-mEGFP and visualized with TIRFM (Figure 39).

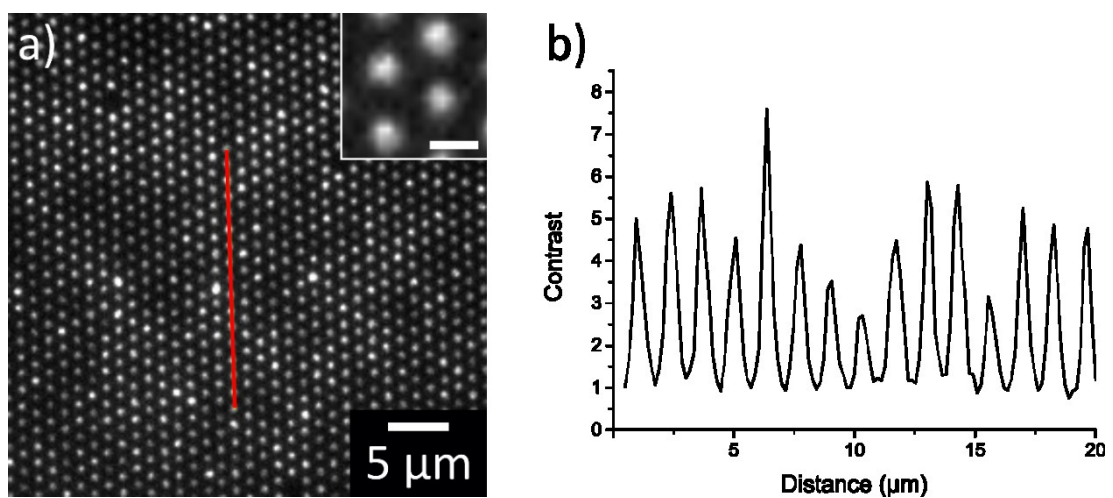


Figure 39: Contrast measurements of BSA-HTL patterned surface. a) TIRFM image (inset scale bar 1 μm). b) Plotted contrast, measurement taken from the red line in panel (a).

The measured contrast amounted to ≈ 4 with a very good pattern fidelity over a large area. Several stamping cycles with this experimental setup resulted in a loss of contrast and pattern fidelity after the first cycle. Due to the hydrophobic nature of the stamp, the BSA protein adsorbs onto the stamp, similar to the adsorption on the hydrophobic silanized glass surfaces, although with a stokes radius of 34 Å BSA is still capable of entering the ≈ 44 nm pores of the silica structure.

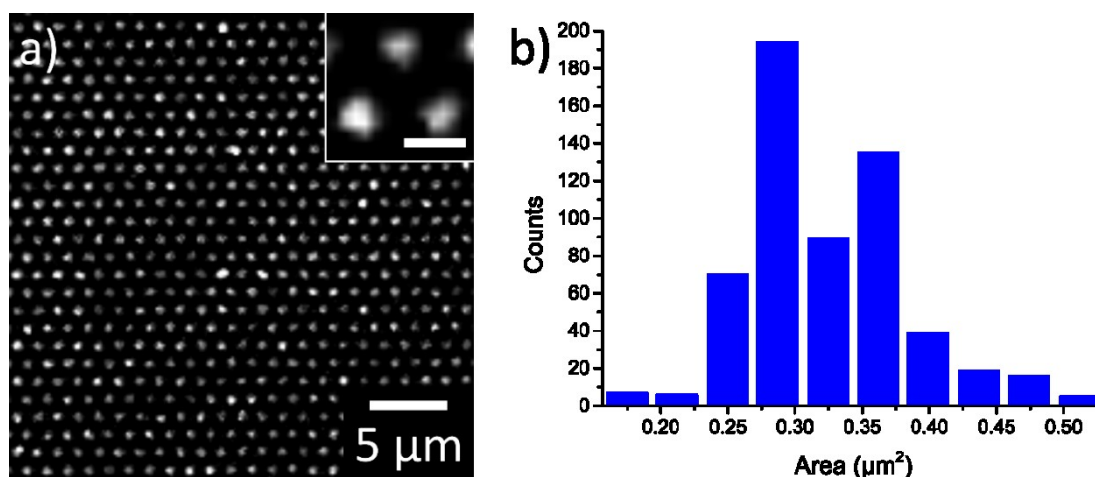


Figure 40: Dot analysis of BSA-HTL patterned surface. a) deconvolved TIRFM image (inset scale bar 1 μm). b) Frequency density of dot areas of BSA-HTL.

The image was deconvolved and analyzed with a watershed algorithm (Chapter 3.2.6). The mean dot area gathered from Figure 40 amounted to $0.346 \mu\text{m}^2 \pm 0.06 \mu\text{m}^2$ with a circularity of 0.96 ± 0.07 and an aspect ratio of 1.27 ± 0.18 . BSA-HTL patterns showed an increase in dot size but almost similar values in circularity and aspect ratio compared to the SAV-protein dot arrays described in chapter 4.2.1. The introduction of the biorthogonal HTL-motif, however, made it possible to test this setup in *in vitro* cell experiments.

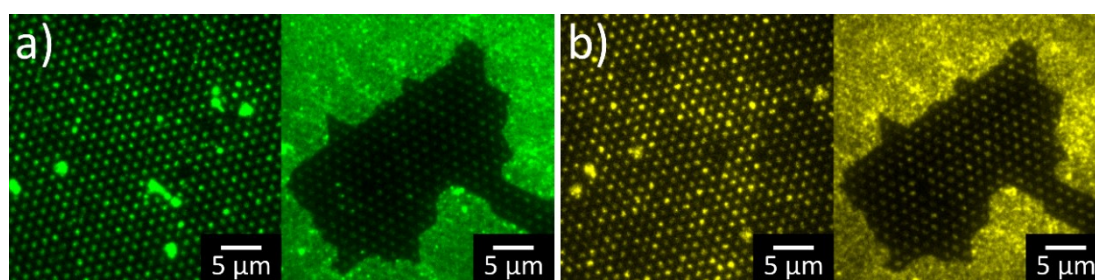


Figure 41: TIRFM image of the same patterned area with two differently modified BSA proteins stamped simultaneously. a) HTL-mEGFP stained dot array and area with overflow ink. b) simultaneously stamped BSA TexasRed array and area with overflow ink.

Within an additional experiment, 1 μl of dye-labeled BSA (BSA TexasRed) was mixed into the ink and stamped with BSA-HTL simultaneously. Therefore, two different dyes were imaged with different laser wavelengths, both showing the same dot array (see Figure 41). On a stamped area of $5 \times 5 \text{ mm}^2$, defects in the pattern by the manual stamping process occurred. Usually, too much ink was transferred to the substrate covering the whole surface. The introduction of a second color to monitor the dot array helped to find suitable patterned areas at the fluorescence microscope when the main functionality, *e.g.*, the BSA-HTL motif, was occupied for live-cell imaging and only featured spots underneath transfected cell. Therefore, BSA was coupled to a variety of different fluorescent dyes covering the common wavelengths (BSA ATTO 488, BSA TexasRed, BSA ATTO 647, BSA ATTO 647N).

To further investigate the organization of BSA on each spot, super-resolution imaging *via* dSTORM was employed^[143]. BSA was labeled with the STORM suitable dye ATTO 647N and directly printed onto an NMTS functionalized glass surface(Chapter 3.4.4)^[144]. The imaging buffer consisted of an oxygen scavenger cocktail and a reducing agent (β -mercaptoethanol), necessary to push the dye into a prolonged dark state, was added to TRIS buffer at pH 8.5. A 405 nm laser was used to recover the dye from the dark state into the excitable ground state. The dot array was bleached for 120 s before the recording to ensure a suitable density of dyes in the dark state for single-molecule localization. For reconstruction of the dot array, a video with 40 fps was recorded over a time of about 12,5 min.

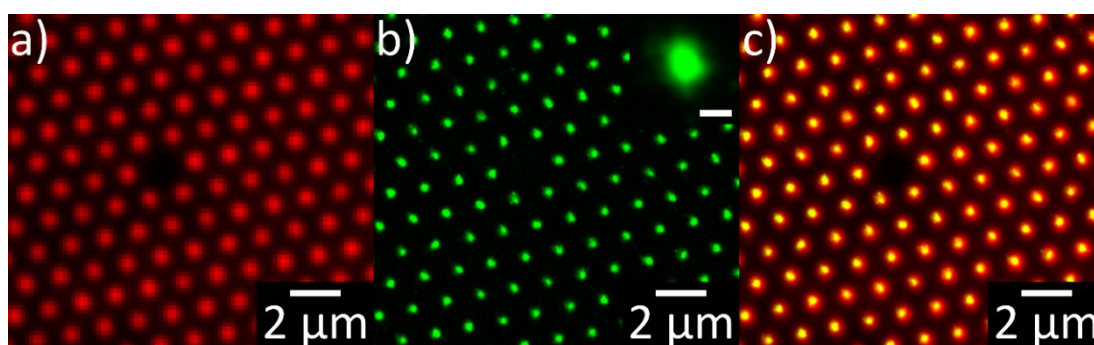


Figure 42: dSTORM analysis of BSA ATTO 647N dot array. a) diffraction-limited image b) reconstructed super-resolution image, inset shows a magnified dot (scale bar: 250 nm) c) composite of the images a) and b)

The diffraction-limited pattern revealed a homogeneous fluorescence intensity across the dot array with a contrast of ≈ 3 (Figure 42a). The super-resolved image, reconstructed with a mean localization precision of approximately 18,3 nm, showcased a precise pattern usually with only one intensity maximum per dot (Figure 42b), suggesting a densely clustered dot with a high

concentration of BSA. Merging the diffraction-limited and the super-resolution image revealed the expected overlap between both imaging conditions (Figure 42c). The subsequent watershed analysis of the super-resolution image can be seen in Figure 43.

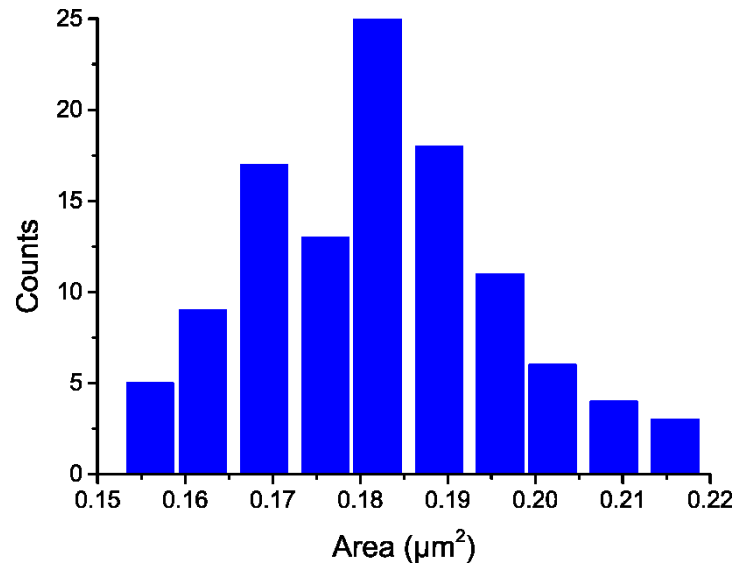


Figure 43: Frequency density of dot areas of dSTORM BSA ATTO 647N.

The calculated mean dot area amounted to $0.185 \mu\text{m}^2 \pm 0.014 \mu\text{m}^2$ with a circularity of 0.84 ± 0.09 and an aspect ratio of 1.18 ± 0.20 .

4.2.3 Modification of BSA-HTL patterns with Designed Ankyrin Repeat Proteins

Designed Ankyrin Repeat Proteins (DARPin) are artificial proteins that can be utilized like an antibody, which entails high affinities and fast reaction times towards specific proteins^[145]. Two DARPin motifs designed to bind GFP were fused with a HaloTag to create an adaptor protein, which will be referred to as double-DARPin (dDARPin). The protein was used in combination with the BSA-HTL patterns due to its fast binding kinetics and multiplying effect towards available bindings sites (see Figure 44).

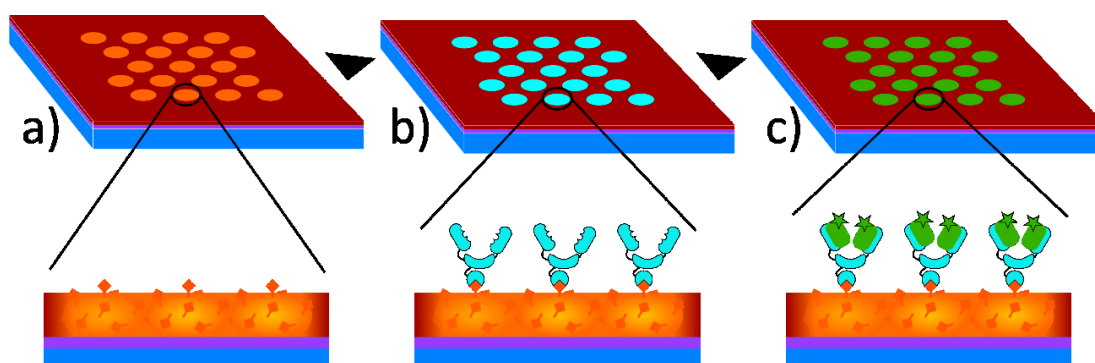


Figure 44: Schematic of further functionalization of BSA-HTL patterned samples. a) patterned BSA-HTL surface. b) functionalization with DARPin-Halo fusion protein. c) staining of the dot array with HaloTag-mEGFP.

Due to its structure, one dDARPin protein can theoretically bind two GFP molecules, thus enhancing the fluorescence intensity by multiplying the fluorophore. With several BSA-HTL molecules per spot, the gained fluorescence could be increased drastically. A linker of 15 aminoacids in between the two DARPin motifs ensured the necessary flexibility to avoid steric hindrance. RlFS measurements confirmed the fast binding of tagless-mEGFP to the DARPin motif (Figure 44). The association constant ($k_a = 7.59 \cdot 10^5 \text{ M}^{-1}\text{s}^{-1}$) to mEGFP is about 70x faster than the Halo-Tag binding to mEGFP^[146]. A similar protein with only one DARPin motif was tested successfully but proved to be worse in terms of contrast than its counterpart and was therefore not considered any further.

BSA-HTL dot arrays were prepared as reported in chapter 4.2.2.2. The resulting samples were then incubated with a high concentration of dDARPin (14 μM) for 1 h. After washing, the BSA-HTL dot arrays were stained with a 200 nM mEGFP solution with 10 % FCS to prevent unspecific binding additionally. The resulting images can be seen in Figure 45.

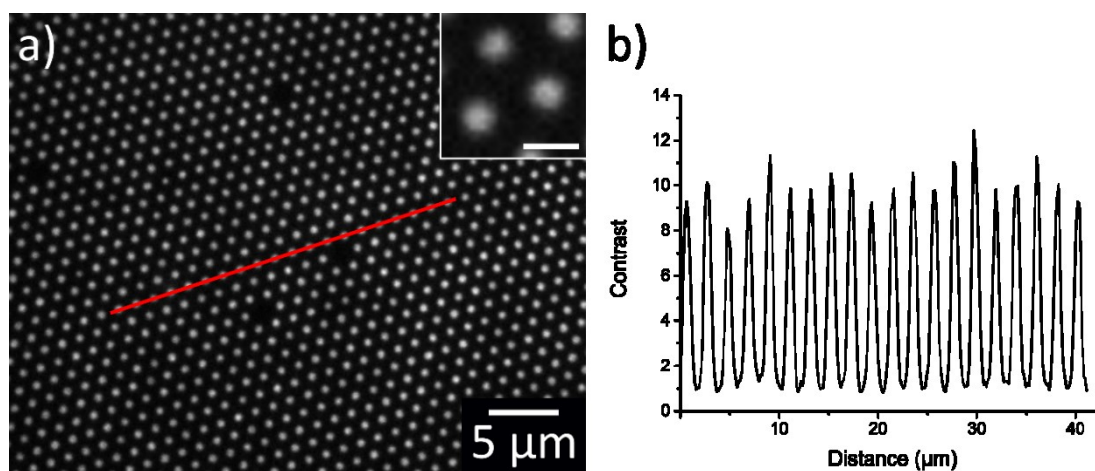


Figure 45: Contrast measurements of BSA-HTL-dDARPin patterned surface. a) TIRFM image (inset scale bar 1 μm). b) Plotted contrast, measurement taken from the red line in panel (a).

The dDARPin functionalization proved to be a substantial improvement in terms of contrast and pattern fidelity. In Figure 45b, the measured contrast amounts to ≈ 9 , which is about a two-fold increase compared to BSA-HTL stained patterns.

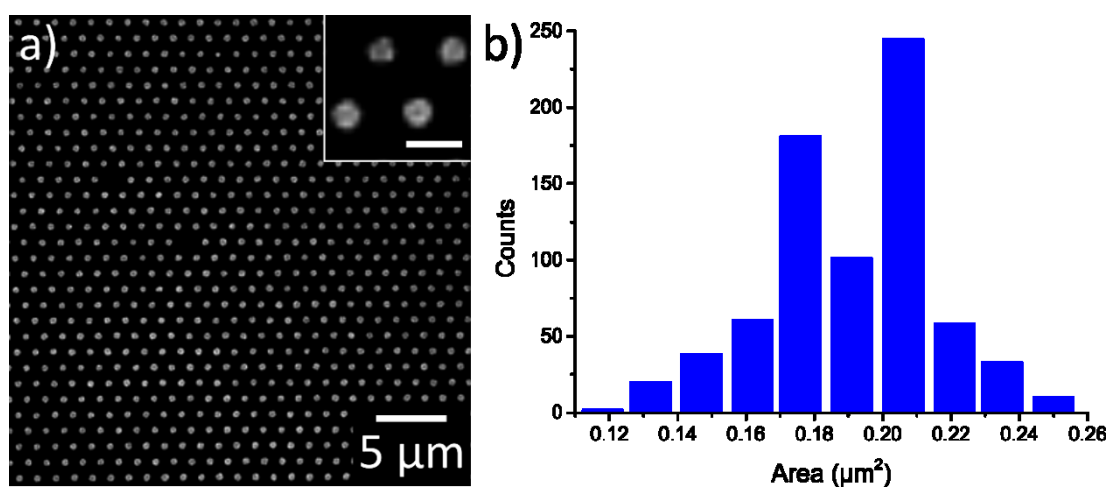


Figure 46: Dot analysis of BSA-HTL-dDARPin patterned surface. a) deconvolved TIRFM image (inset scale bar 1 μm). b) Frequency density of dot areas of BSA-HTL-dDARPin.

The mean dot area gathered from Figure 46 amounted to $0.196 \mu\text{m}^2 \pm 0.024 \mu\text{m}^2$ with a circularity of 0.99 ± 0.02 and an aspect ratio of 1.14 ± 0.09 .

4.2.4 Stamping of BSA-HTL on graphene

Graphene is subject to various research interests because of its unique properties^[147,148]. It also found applications as a substrate for biosensors^[149]. Similar to metals, it is able to engage in an energy transfer mechanism. Therefore, it is utilized to study conformational changes in proteins

due to the quenching of fluorophores in relation to the distance between protein and graphene^[150]. The 2D-hexagonally ordered carbon atoms in graphene are sp^2 -hybridized and therefore exhibit an extensive delocalized electron system. Graphene is suitable for *in vitro* cell experiments and was therefore tested as a suitable patterning substrate for possible biosensing applications.

Since the BSA-HTL-dDARPin approach showed the best results, it was adapted for stamping on graphene as well. After deposition of a graphene layer on a glass slide, the samples were patterned with BSA-HTL as described and subsequently functionalized with dDARPin proteins. For imaging purposes, the dot arrays were labeled with mEGFP.

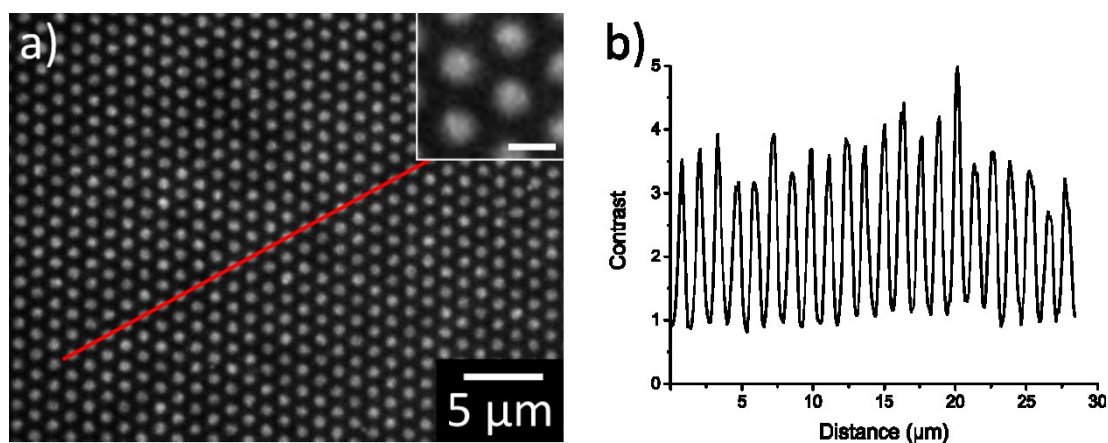


Figure 47: Contrast measurements of BSA-HTL-dDARPin patterned graphene surface. a) TIRFM image (inset scale bar 1 μm). b) Plotted contrast, measurement taken from the red line in panel (a).

The contrast gained from graphene patterned surfaces was ≈ 3.5 (see Figure 47) and is slightly higher than the contrast obtained by the purely BSA-HTL stamped surfaces (Chapter 4.2.2.2). This value would be enough to proceed with *in vitro* experiments. The quenching effect on the fluorescence was not further investigated, but its possible applications in distance measurements *via* graphene-induced energy transfer could be promising. The dot arrays also showed little to no defects over large areas comparable with dot arrays on NMTS surfaces.

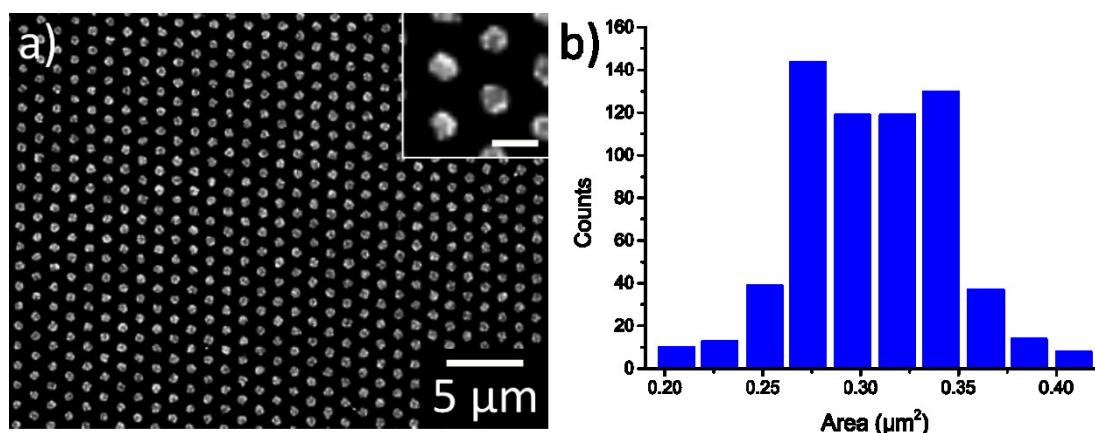


Figure 48: Dot analysis of BSA-HTL-dDARPin patterned graphene surface. a) deconvolved TIRFM image (inset scale bar 1 μm). b) Frequency density of dot areas of BSA-HTL-dDARPin on graphene.

The mean area gathered from Figure 48 amounted to $0.317 \mu\text{m}^2 \pm 0.038 \mu\text{m}^2$ with a circularity of 0.96 ± 0.05 and an aspect ratio of 1.14 ± 0.08 . The closest comparison to the obtained values was again the purely BSA-HTL patterned surfaces. This underlines the assumption that graphene behaves similarly in terms of adsorption potential towards BSA.

4.3 Comparison of stamped dot arrays

As a comparison, every histogram of the dot area distribution was summarized in Figure 49.

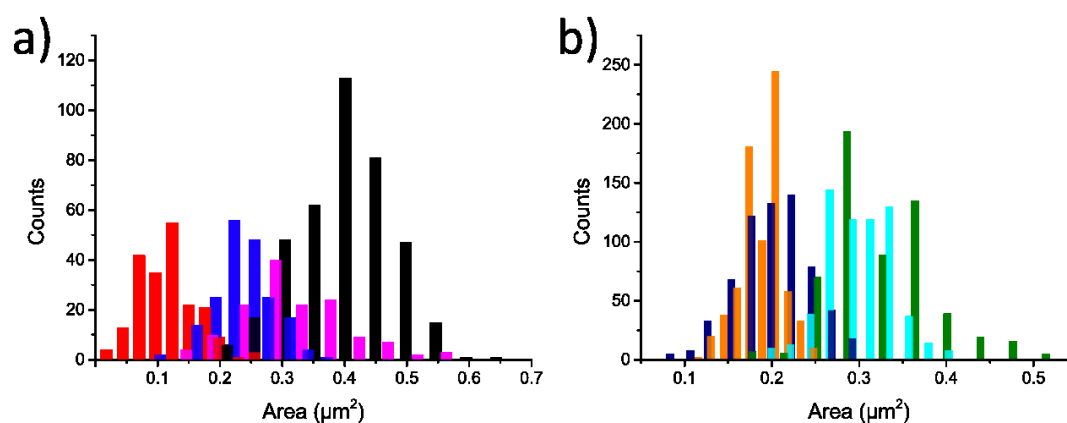


Figure 49: Area-histogram of all analyzed stamping experiments. a) Stamping of cyclic silanes (Red: Cycloazasilane-HTL; Magenta: Cyclothiosilane-ATTO 655; Blue: Cycloazasilane-ATTO 647; Black: PS-brush-Cy5). b) Stamping of proteins (Dark blue: PEG-bt-SAV-Cy5; Orange: BSA-HTL-dDARPin; Green: BSA-HTL; Cyan: BSA-HTL-dDARPin on graphene).

The dDARPin modified BSA-HTL spot size is with an average of $0.196 \mu\text{m}^2$, the smallest achieved dot size with an excellent pattern fidelity. The area, which can roughly be converted into a diameter of $\approx 500 \text{ nm}$, strikes a good compromise between miniaturization and optical

resolution restrictions. While fluorescence-based super-resolution microscopy techniques are well established, diffraction-limited microscopy is still very much prevalent. Dots slightly below the 1 μm range are desirable because they can be imaged by conventional light-based microscopy. Since every tested system exhibits sizes above the diffraction limit, the ideal system is the one with the smallest dot sizes, which can be reliably stamped. Although the HTL modified cycloazasilane arrays displayed a smaller area of 0.134 μm^2 , their skewed shape (circularity: 0.70, aspect ratio: 2.38) combined with a bad pattern fidelity made them an inferior system compared to BSA-HTL (circularity: 0.96, aspect ratio: 1.28) or BSA-HTL-dDARPin (circularity: 0.99, aspect ratio: 1.14) (see Table 8). The PEG-OMe/PEG-bt functionalized surface almost matched the dDARPin results in both categories but fell short in a contrast comparison. Despite the fact that patterning with BSA could not be done in a successive manner and re-loading the stamp with ink in between cycles was necessary, similar average dot areas compared to the cycloazasilane patterned surfaces could be achieved. With a conversion from the area into diameter, values in the range of \approx 500-650 nm can be calculated. The size of one contact element on the stamp equals \approx 400 nm. Assuming that the stamp tips deform slightly upon contact with the surface due to its elastic material, the calculated diameters are within a reasonable agreement to expectable values. However, the dot array based on fluorescently labeled cyclosilanes displayed a less uniform dot shape. Because the silanes had to be stamped from water-free toluene, the spreading of the ink on the sample surface is the most likely explanation of these results. The contact angle of toluene on glass is 0°. Complete ink spreading is only inhibited by the quick reaction between silane and surface and the subsequent change in contact angle. In comparison, water exhibits a contact angle of 53,3° on NMMS-functionalized surfaces. Post-functionalizations based on cycloazasilane patterned surfaces (*e.g.*, click-HTL, PS-brush) lead to even larger shifts in every parameter, with an additional drop in contrast. For live-cell imaging, a high contrast is desirable because due to unspecific binding, autofluorescence of cells and free dye, a further decrease in contrast is inevitable, making analysis impossible for low contrast systems. The highest contrast gained amounted to \approx 10 with the BSA-HTL-dDARPin system. This feature can be explained by the multiplying effect of the dDARPin protein. Other protein-based stamping approaches also gained values in the 4-5 range, thus improving over the silane patterning approach.

The generated pattern size generally varied from cycle to cycle, which can be primarily attributed to the alignment of the stamp to the surface. The PDMS layer underneath the stamp helped to mitigate some alignment problems but could not entirely prevent different results. Similarly, different dot sizes and areas where too much ink was transferred to the surface occurred for almost every patterned sample. Since this is a manual process without precise

control over contact pressure, time and alignment, that can be expected. Nonetheless, dot arrays with an area of several hundreds of micrometers could reliably be stamped for every sample. A total failure to generate patterns was rarely observed as soon as the method was established.

Table 8: Summary of Circularity, aspect ratio and contrast for each stamping experiment.

| Name | Area | Circularity | Aspect ratio | Contrast |
|---|-------------------------------|--------------|--------------|----------|
| Cycloazasilane (4th stamping cycle) | 0.250 ± 0.044 μm ² | 0.92 ± 0.080 | 1.39 ± 0.25 | ≈ 3.2 |
| Cyclthiosilane (4th stamping cycle) | 0.323 ± 0.086 μm ² | 0.78 ± 0.10 | 1.57 ± 0.40 | ≈ 1.3 |
| PS-brush-Cy5 | 0.440 ± 0.076 μm ² | 0.86 ± 0.12 | 1.24 ± 0.17 | ≈ 1.3 |
| Cycloazasilane-HTL | 0.134 ± 0.046 μm ² | 0.70 ± 0.18 | 2.38 ± 0.72 | ≈ 1.5 |
| PEG-bt-SAV-Cy5 | 0.207 ± 0.039 μm ² | 0.96 ± 0.056 | 1.22 ± 0.14 | ≈ 4.5 |
| BSA-HTL | 0.346 ± 0.060 μm ² | 0.96 ± 0.072 | 1.28 ± 0.18 | ≈ 5 |
| BSA-HTL-dDARPin | 0.196 ± 0.024 μm ² | 0.99 ± 0.022 | 1.14 ± 0.086 | ≈ 10 |
| BSA-HTL-dDARPin (on graphene) | 0.317 ± 0.038 μm ² | 0.96 ± 0.051 | 1.14 ± 0.080 | ≈ 4 |

4.4 Cellular interactions – proof of principle

4.4.1 Reorganization of membrane associated IFNAR2-receptor

Type I Interferons (IFNs) are important cytokines for innate immunity against viruses and cancers^[151]. The IFN receptor comprises two subunits, IFNAR1 and IFNAR2. IFNAR1 and IFNAR2 are dimerized by simultaneous interaction with IFN *via* independent binding epitopes^[152]. IFNAR2 binds IFNα2 with an equilibrium dissociation constant of ≈ 5 nM and a complex lifetime of ≈ 100 s, whereas the affinity toward IFNAR1 is three orders of magnitude lower^[153]. Formation of ternary IFN/IFNAR2/IFNAR1 signaling complex at the plasma membrane initiates downstream signaling pathways (*e.g.*, JAK/STAT, MAPK)^[154,155]. In this work, the IFN signaling pathway was used to demonstrate the ability to recruit target membrane proteins to the dot arrays. For this purpose, BSA-HTL patterned slides were prepared as described in chapter 4.2.2.2. After the modification, HeLa cells were transfected with HaloTag-mEGFP-IFNAR2 and seeded on a BSA-HTL

patterned coverslip overnight. The HaloTag fusion protein is expressed extracellularly and can interact with the BSA-HTL dots. mEGFP, also expressed extracellularly, acts as the fluorescent label to monitor the spatial resolved IFNAR2 receptor reorganization and aggregation onto the dot arrays. Figure 50 presents the corresponding schematic and the expected reorganization of HaloTag-mEGFP-IFNAR2.

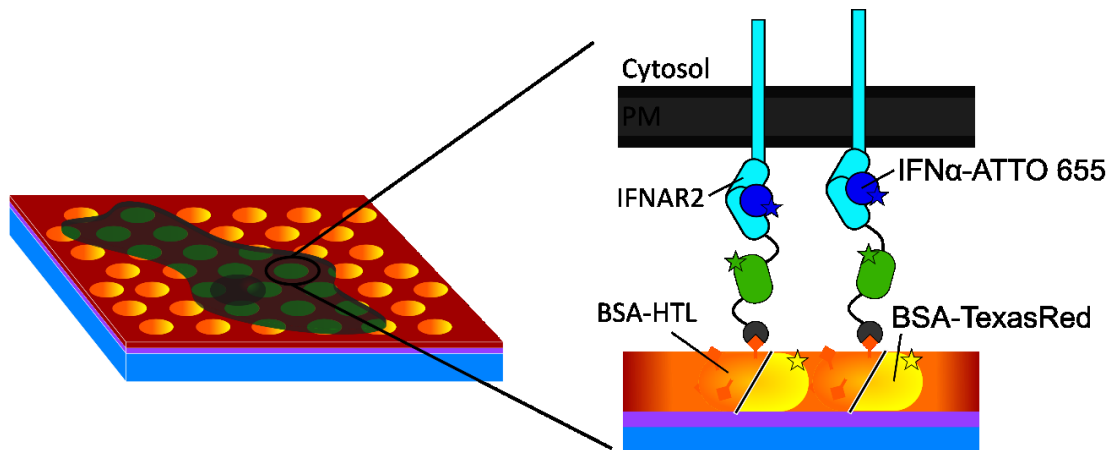


Figure 50: Schematic of BSA-HTL/BSA-TexasRed patterned surface with HaloTag-mEGFP-IFNAR2 transiently transfected HeLa cells. The IFNAR2 receptor binds to the dot array *via* the HaloTag protein and is reorganized in the plasma membrane, adapting the patterned structure. BSA-TexasRed was added to the ink to visualize the printed dot array. IFN α -ATTO 655, added during the recording, binds selectively to the spatially arranged IFNAR2 receptor.

In this experiment, TexasRed-BSA was also added to the ink solution and used to find patterned areas with high contrast and a low number of defects.

In Figure 51, the live-cell TIRFM images are shown.

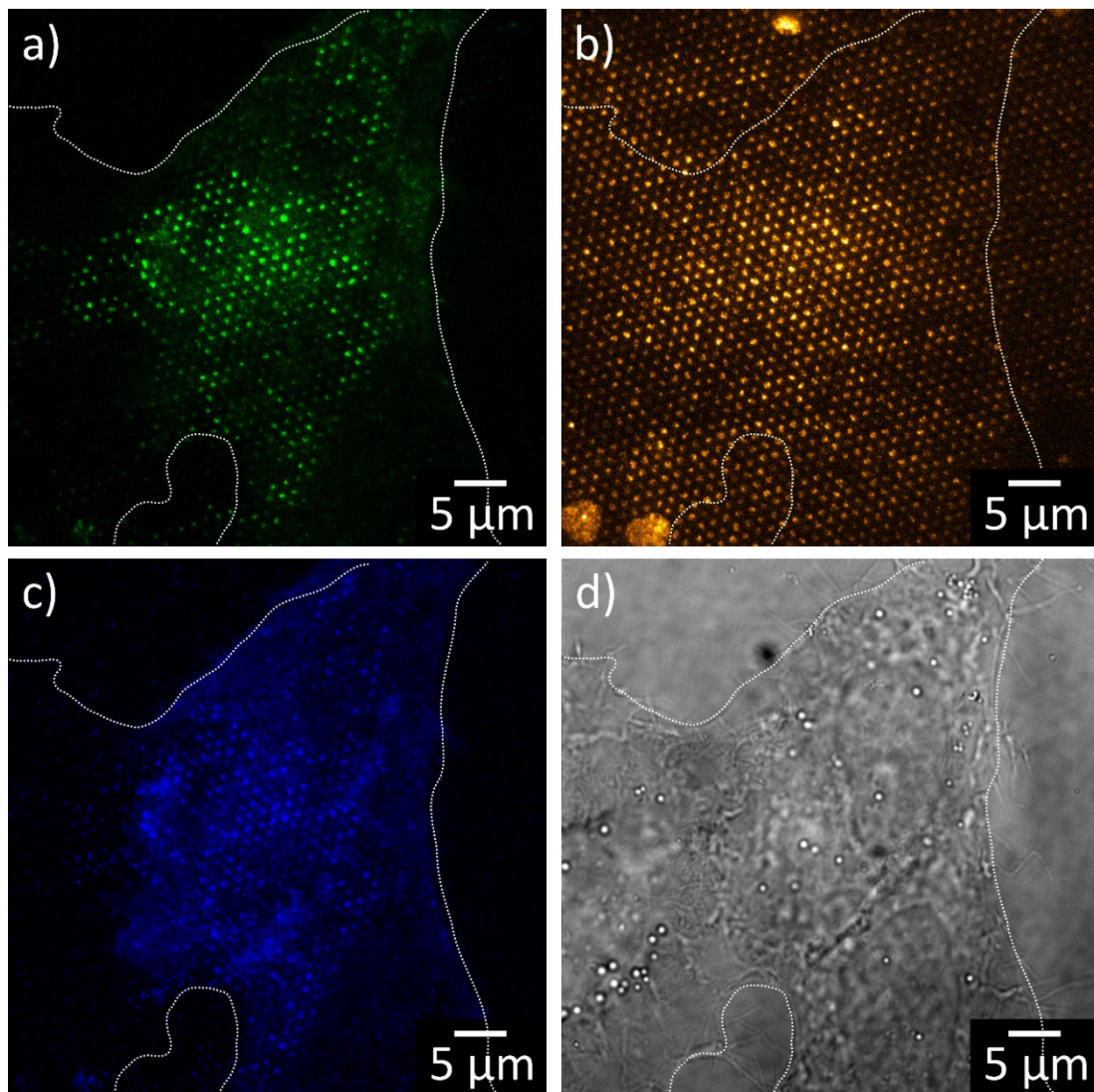


Figure 51: TIRFM images of HaloTag-mEGFP-IFNAR2 transfected cells seeded on BSA-HTL patterned surface. a) reorganized IFNAR2 receptors visible by mEGFP fluorescence. b) BSA TexasRed fluorescence shows the dot array. c) fluorescence of ATTO 655 labeled Interferon. d) DIC image.

The 562 nm channel monitoring the BSA TexasRed displayed a well-patterned area with discrete dots. In the GFP channel (488nm), the dot array was clearly visible and confirmed the reorganization of the membrane proteins. To further complement the results, 10 nM ATTO 655 labeled Interferon was added on site. The corresponding signaling protein is bound to the accumulated receptor in a short amount of time, making the same pattern visible in the 642 nm channel. This demonstrated the still intact functionality of the IFNAR2 receptor.

4.4.2 Live-cell analysis of dDARPin modified HTL-BSA dot arrays

The BSA-HTL dDARPin system was tested *in vitro* by transfecting HeLa cells with mEGFP-Lrp6. Lrp6 is one of the four proteins involved in the canonical Wnt signaling pathway. Together with Fzd8, it forms the membrane-bound part of the pathway, while Dvl2 and Axin1 are only intracellularly present^[106]. mEGFP is expressed extracellularly with Lrp6 and can bind to the dDARPin fixed on the stamped dot arrays, thus reorganizing the membrane-bound Lrp6 receptors. In Figure 52, a schematic image of the reorganization of Lrp6 can be seen.

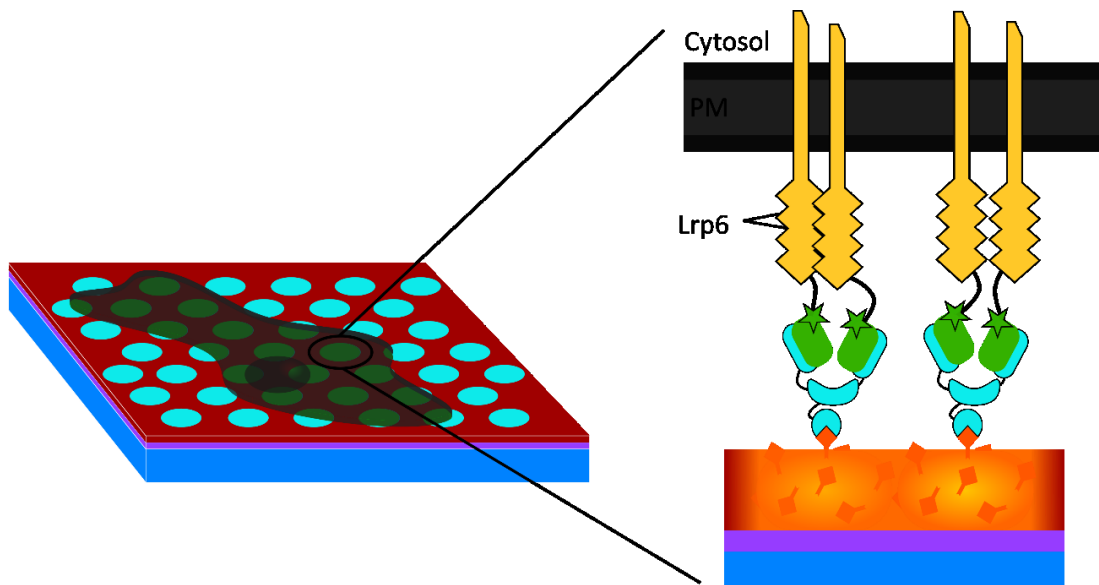


Figure 52: Schematic of BSA-HTL-dDARPin patterned surface with mEGFP-Lrp6 transiently transfected HeLa cells. BSA-HTL is functionalized with dDARPin after surface patterning and then used as a substrate for transfected HeLa cells. mEGFP selectively binds to the dDARPin protein and recruits the Lrp6 receptor to the dot array.

The samples were patterned with BSA-HTL, backfilled with FCS and combined with the dDARPin protein as described in chapter 4.2.3. The mEGFP-Lrp6 transfected HeLa cells were seeded onto the slides in a petri dish and cultured for \approx 6-7 h. The selected time frame gives the cells enough time to attach themselves and adapt to the stamped pattern. The slides were then transferred into suitable holders for TIRFM and imaged with cell culture medium without indicator at 25 °C.

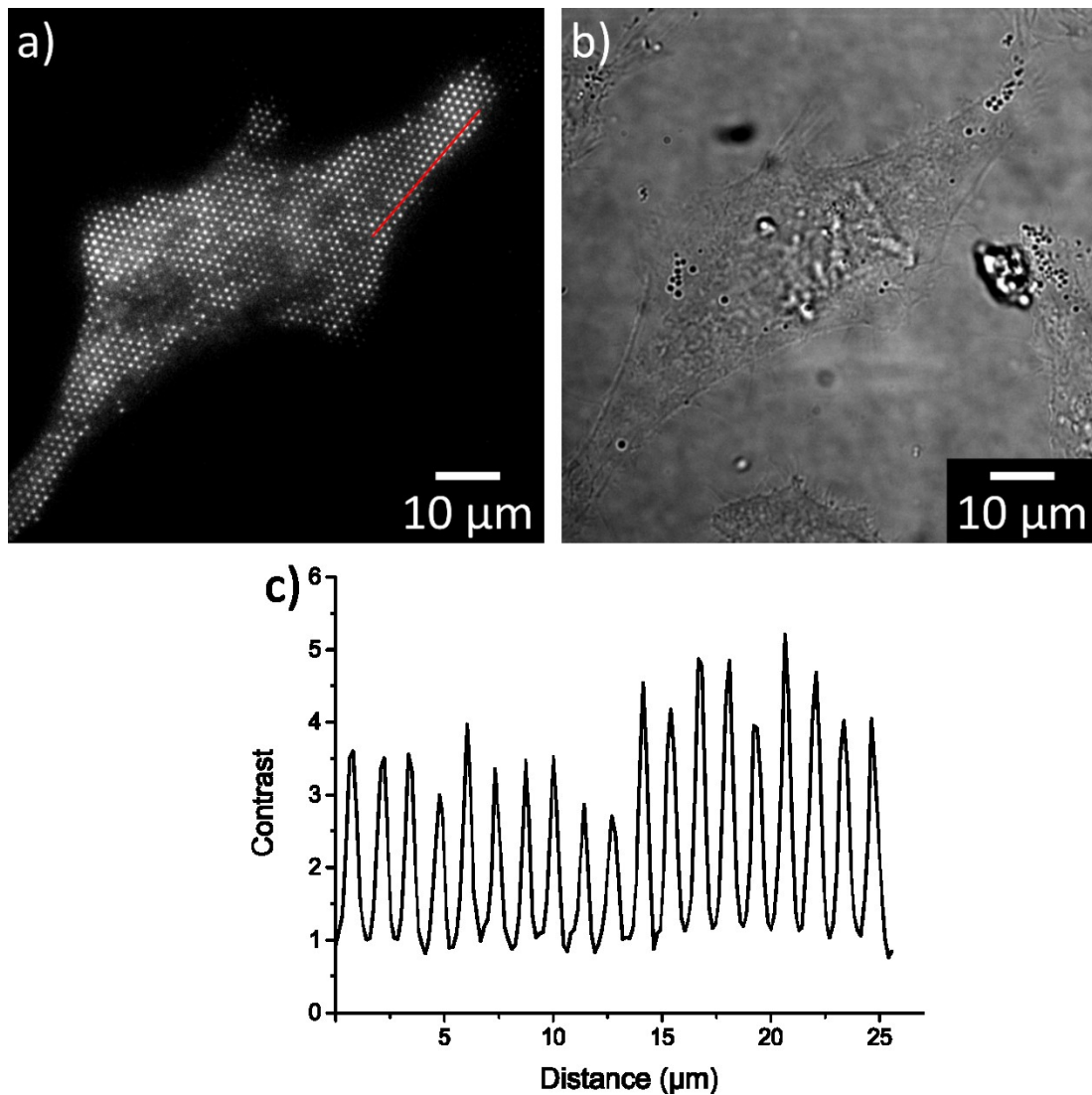


Figure 53: TIRFM images of mEGFP-Lrp6 transfected cells seeded onto a BSA-HTL-dDARPin patterned glass slide. a) TIRFM image of the transfected cell. b) DIC image. c) Plotted contrast, measurement taken from the red line in panel (a).

The images in Figure 53 show the adapted pattern by the labeled Lrp6 receptor within the cell boundaries. Although there is a visible background intensity from not attracted Lrp6, a contrast up to a maximum of ≈ 5 could be reached. The high contrast suggests a dense aggregation of mEGFP and, in conclusion, a high concentration of Lrp6 receptors. This was vital for the investigation of the Wnt pathway since it is stimulated by the assembly of dense receptor clusters. The BSA-HTL-dDARPin system was utilized to get further insight into the interactions between the involved receptors in the canonical Wnt-signaling pathway.

4.4.3 Protein binding on BSA-HTL-dDARPin patterns manipulated by optogenetics

Optogenetics was introduced as a powerful tool to investigate various biological processes^[156]. For applications of manipulating protein-protein interactions, optogenetic methods can initiate

protein dimerization, introducing an acute ‘on’ and ‘off’ state. Most prominently, proteins of interest fused to optogenetic tags can be recruited spatiotemporally. This allows a well-defined localization and timing to active protein-protein interactions. The optogenetic system used here was the iLID system with its corresponding binding protein SspB. Upon irradiation with blue light, e.g., 488nm laser, iLID enables binding of SspB. Due to the low binding affinity in the dark state, the iLID/SspB photo-induced protein dimerization holds until the end of the illumination and dissociates at the dark state. With an optimized dose of light for illumination, the iLID optogenetic system can be activated multiple times and perform several recruitment cycles. As a proof-of-concept, the iLID protein was fused to an extracellular mEGFP and consequently recruited to the dot arrays *via* interaction with the dDARPin (Figure 54).

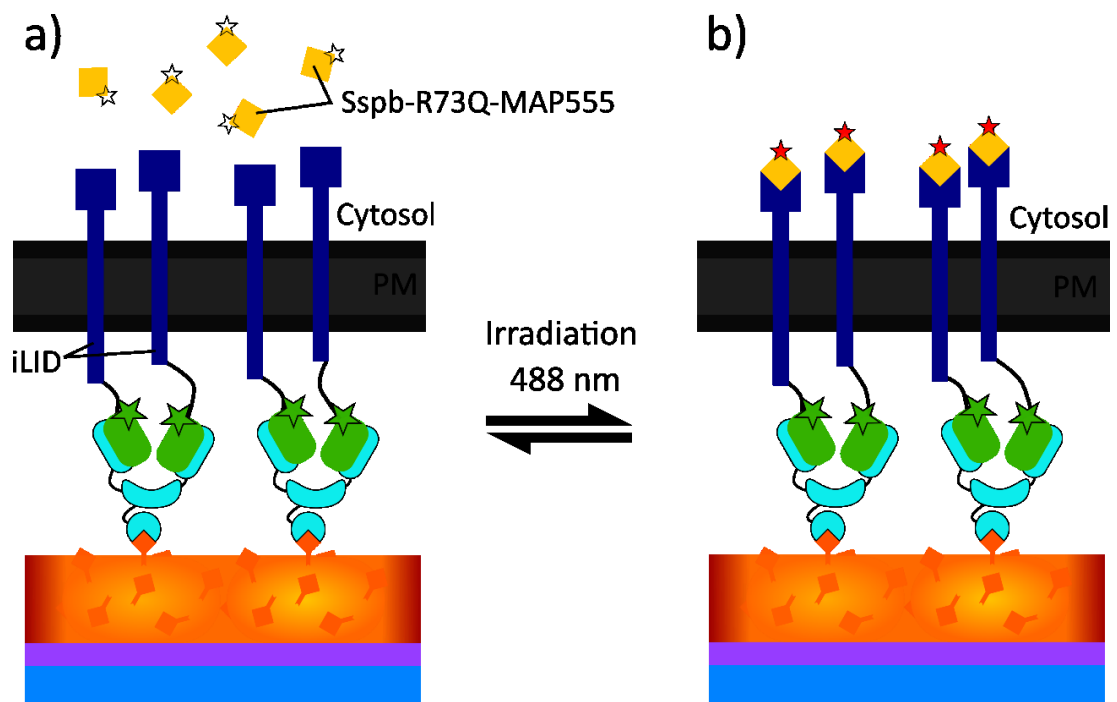


Figure 54: Schematic of the optogenetic system applied to the BSA-HTL-dDARPin patterned surface. HeLa cells are transiently transfected with mEGFP-iLID and steadily clustered onto the dot array by the mEGFP-dDARPin interaction. Cells are also stained with Sspb-R73Q-MAP555. a) Without the irradiation with 488 nm light, the cytosolic part of the iLID receptor remains in an OFF-state and is not capable of binding Sspb-R73Q-MAP555. b) Upon irradiation with 488 nm light, the iLID receptor changes conformation and binds the Sspb protein and, therefore, recruits the fluorogenic MaP555 dye to the printed array.

For the SspB protein, two mutants were developed to broaden the effective binding affinity range, the native SspB, termed SspB nano, performs in the nM-range while SspB micro shows an effective range in μM concentrations^[157]. According to the results of pre-tests, the SspB micro with a mutation at R73Q was used in the experiment. For the identification of nanodot arrays, mEGFP-TMD-iLID fusion was used as bait protein in patterned cells (Figure 54). The SspB micro was labeled *via* Snap-Tag with MaP-555. MaP-555 is a cell-permeable fluorogenic dye that shifts

its two-state equilibrium from the low fluorescent form to its high fluorescent form upon binding to its targets^[158]. The dye was introduced to replace Snap-SiR since previous results showed poor contrast, presumably by the strong interaction between Snap-SiR and the silanized surface.

Transfected cells were seeded onto patterned glass slides and left in the incubator overnight. Before imaging with TIRFM, cells were stained with 50 nM MaP-555. Light-induced binding of SspB micro to iLID was initiated by irradiation with a 488 nm laser. Because of its sensitivity and possible photodestruction of FMN in iLID by overexposure to high light intensities, the 488 nm laser was set to the lowest output value of 1 % and further dimmed with a 5 % transmission filter. The pattern was illuminated for ten consecutive cycles, each cycle with an activation time of 30 s and 90 s of decay time. In the decay timeframe, only the MaP-555 channel was imaged with one frame per second.

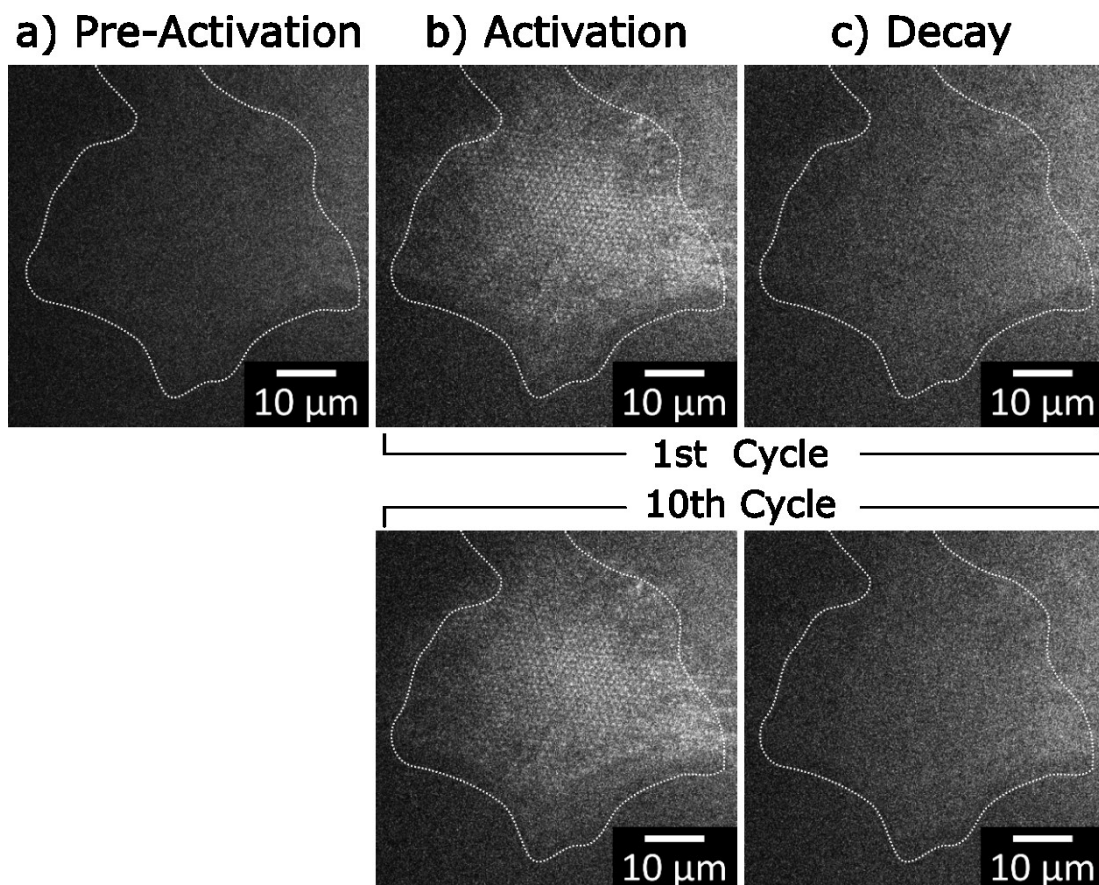


Figure 55: TIRFM images extracted from activation/decay cycles of HeLa cells transfected with optogenetic iLID-system. a) image pre-activation. b) activation with 488 nm laser, image taken from the last frame of each cycle, top: 1st cycle; bottom: 10th cycle. c) decay with no illumination, the image was taken from the last frame of each cycle, top: 1st cycle; bottom: 10th cycle.

In Figure 55b, images of the 1st and 10th activation cycles are shown. For each cycle, the last frame of the activation and the last frame of the decay was used. Even though the contrast is

poor with less than 1, a pattern can be seen after illumination with blue light. After the 90 s without activation, the pattern is not visible anymore and the overall fluorescence level drops to similar levels compared to the 1st cycle. It should be noted that the residual fluorescence after each cycle is higher compared to the intensity before the 1st activation. A complete graph of the average intensity measured within the pattern through all cycles can be seen in Figure 56.

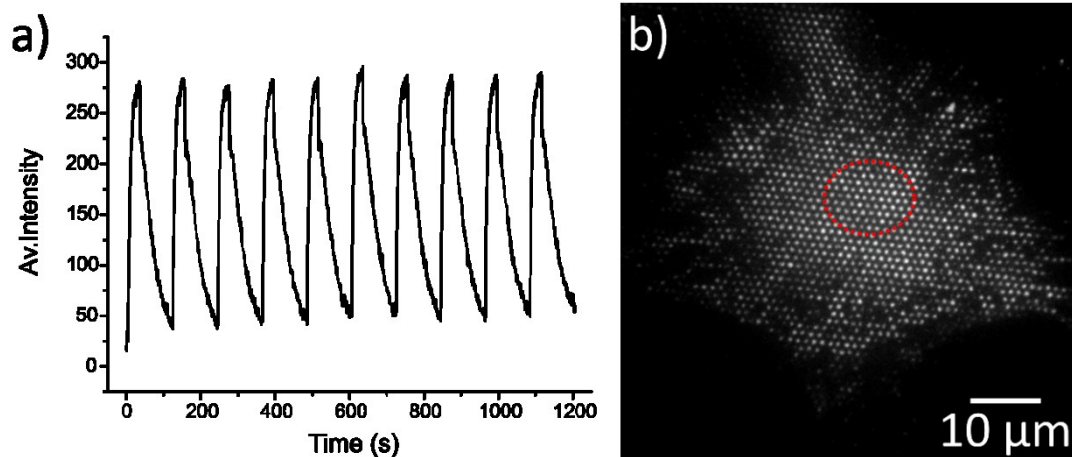


Figure 56: Time series analysis over activation cycles, area of interest marked with a red circle. a) Time series analysis diagram with 10 consecutive activation/decay cycles (Activation: 30 s; Decay: 90 s). b) Image of the cell after the analysis with higher laser power.

The graph in Figure 56a shows recruitment to consistent intensity values for each cycle alongside a fall off to similar dark-state values. Once the measurement was done, an image of the mEGFP pattern with higher laser power was taken, which confirms the reorganization of the membrane-anchored iLID protein (Figure 56b).

4.4.4 Reorganization of signaling proteins complexes in the Wnt signaling pathway

The canonical Wnt signaling pathway is vital for the maintenance and differentiation of stem cells. As introduced in section 2.3, the canonical Wnt signaling involves four key proteins for signal transduction at the plasma membrane. These are the low-density lipoprotein receptor-related protein 6 (Lrp6) and its co-receptor Frizzled 8 (Fzd8) located at the plasma membrane, and Axin1 and Dishevelled 2 (Dvl2) in the cytosol^[106]. One way to activate the canonical Wnt signaling pathway is the hetero-dimerization between Lrp6 and Fzd8 by a Wnt ligand. This leads to the binding and recruitment of cytosolic Dvl2 and Axin1 into multiprotein complexes termed Wnt signalosomes. The functional consequence is inhibition of the destruction complexes, which eventually leads to an increase in β -catenin levels in cytosol and

nucleus for canonical Wnt signaling. Of note, Axin1 and Dvl2 act as the core scaffold proteins in the destruction complex to mediate proteasomal destruction of β -Catenin.

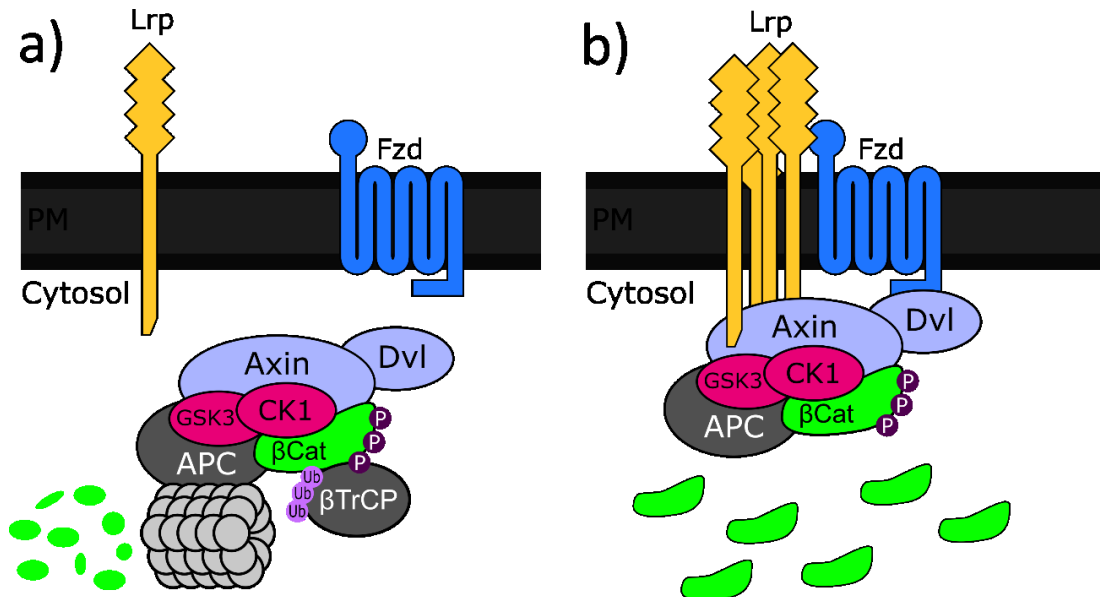


Figure 57: Schematic representation of canonical Wnt pathway activation by clustering of Lrp6 without Wnt ligand. a) In the absence of the Wnt ligand, Lrp6 and Fzd8 do not dimerize and the destruction complex around the scaffold proteins Axin1 and Dvl2 are not inhibited in their function to degrade β -catenin. b) Clustering of Lrp6 on the dot array leads to the formation of the Wnt signalosome and the accumulation of β -catenin by inhibiting the function of the destruction complex.

Reorganization of signaling protein complexes in the canonical Wnt signaling pathway of live cells was carried out on the nanodot arrays. During these experiments, BSA-HTL was stamped *via* capillary stamping and combined with the dDARPin functionalization. Cells were transfected with mEGFP-Lrp6 and seeded onto patterned substrates as previously described. It was reported previously that the Wnt signaling pathway could also be activated by clustering the Lrp6 receptor^[115] (Figure 57). Therefore, the recruitment of Lrp6 to the nanodot array and the accompanied enrichment effect of the co-receptors has the potential for initiating Wnt signaling at a high receptor density with a certain threshold.

4.4.4.1 Triple transfection of HeLa cells with Wnt pathway relevant proteins

HeLa cells were co-transfected with Wnt signaling relevant proteins on the bifunctional nanodots to test whether canonical Wnt signaling occurs on the nanodot arrays. First, Lrp6 was found to be recruited to the dot array by the established interaction between mEGFP and the dDARPin protein. In order to test if the increased concentration of Lrp6 on the dot arrays was enough to co-recruit other relevant proteins, HeLa cells were co-transfected to express three

different Wnt relevant proteins. Those were mEGFP-Lrp6, td-mCherry-Dvl2 and Fzd8, which was labeled with DY-647 *via* fused SNAP-Tag (Figure 58f).

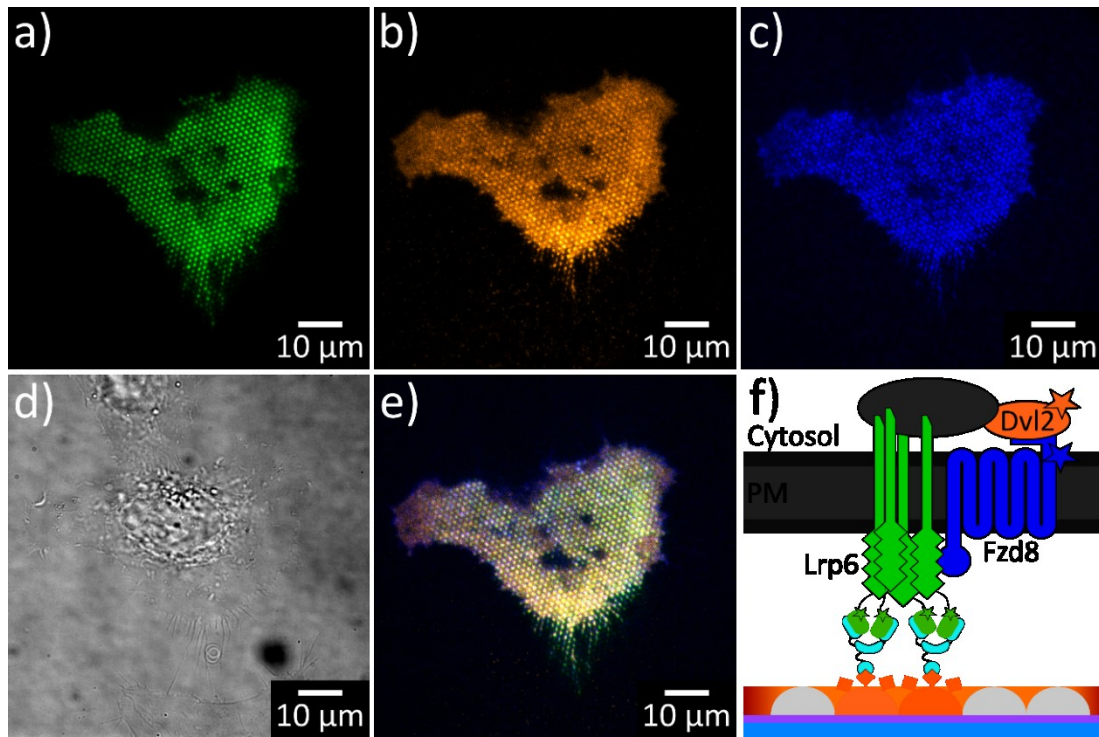


Figure 58: TIRFM of triple transfected HeLa cells exhibiting spatial reorganization of membrane-bound Lrp6 receptor and co-recruitment of Dvl2 and Fzd8. a) mEGFP-Lrp6 b) td-mCherry-Dvl2 c) Fzd8-DY 647 d) DIC image. e) Merged image of all three channels a-c). f) Schematic visualization of the triple color experiment with mEGFP-Lrp6 (green), Fzd8-DY647 (blue) and Dvl2 (orange) on the BSA-HTL-dDARPin patterned surface.

The images in Figure 58 show a sharp patterning in the green channel, which is consistent with previous results of recruiting mEGFP-fusion proteins to the dDARPin nanodots. The membrane-bound Fzd8 receptor also adapted to the nanodot arrays suggesting a successful co-recruitment and reorganization of the Wnt co-receptors at the membrane. In the orange channel, the cytosolic td-mCherry-fused Dvl2 protein matched the dot arrays very well. The merged image of all three colors in Figure 58e showed a good correlation between the dot array of each channel.

To determine the effect of the spatial reorganization of Lrp6, Fzd8 and Axin1, triple-color TIRF microscopy imaging was performed to explore the co-patterning of mEGFP-Lrp6, td-mCherry-Axin1 and Snap-Tag-Fzd8 (Figure 59f).

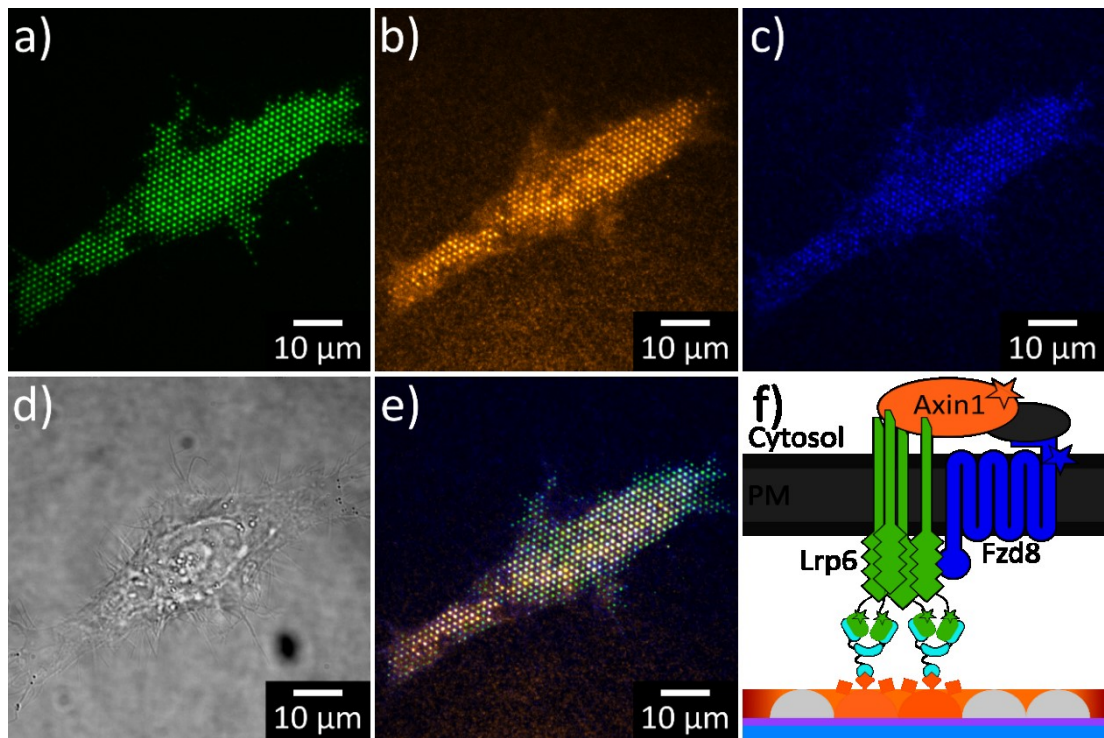


Figure 59: TIRFM of triple transfected HeLa cells exhibiting spatial reorganization of membrane-bound Lrp6 receptor and co-recruitment of Axin1 and Fzd8. a) mEGFP-Lrp6 b) td-mCherry-Axin1 c) Fzd8-DY647 d) DIC image. e) Merged image of all three channels a-c). f) Schematic visualization of the triple color experiment with mEGFP-Lrp6 (green), Fzd8-DY647 (blue) and Axin1 (orange) on the BSA-HTL-dDARPin patterned surface.

Similar to the triple color experiment for Lrp6/Fzd8/Axin1, both Fzd8 and Axin1 could be recruited significantly to the same dot array (Figure 59a-c). The merged image shows strong overlapping of all monitored channels (Figure 59e).

To obtain a quantitative understanding of the protein assembly, the fluorescence intensities of individual dots were picked *via* a particle localization algorithm (Chapter 3.2.6). After image deconvolution, the protein nanodots in each channel were located and the fluorescence contrast of each dot was calculated by comparing the intensity in the dot to the proximity. The

logarithm of the contrasts of Axin1 and Fzd8 was plotted against the logarithm of the Lrp6 contrast, respectively.

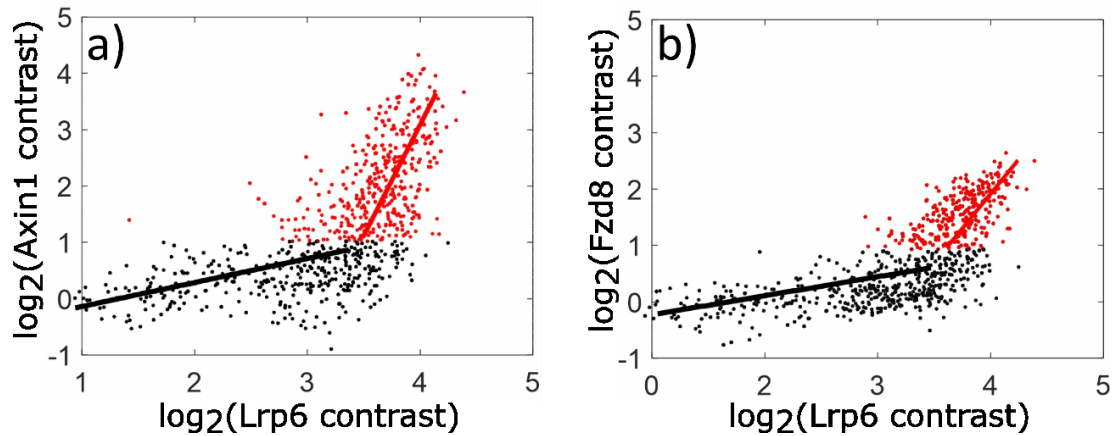


Figure 60: Colocalization and activation threshold analysis of mEGFP-Lrp6 with mCherry-Axin1 or Fzd8-DY647 a) Contrast plot of colocalized dots between mEGFP-Lrp6 and mCherry-Axin1 (black: correlation fit of values below threshold; red: correlation fit of values above the threshold of Axin1, fixed at 2) b) Contrast plot of colocalized dots between mEGFP-Lrp6 and Fzd8-DY647 (black: correlation fit of values below threshold; red: correlation fit of values above the threshold of Fzd8, fixed at 2)

This analysis revealed a two-phase correlation between the contrasts of the Lrp6 receptor and Axin1/Fzd8. It shows Axin1 and Fzd8 were slightly recruited to the Lrp6 spot at low contrast of Lrp6 (Figure 60a). Strikingly, above a contrast threshold of ≈ 10 for Lrp6, the co-recruitment of Axin1 and Fzd8 to Lrp6 gets more pronounced. The slope of the red log-log plots was 3.8 for Axin1 vs. Lrp6 and 2.2 for Fzd8 vs. Lrp6 when the critical value was set to 2 (see the boundary of the black and red dots in Figure 60). For comparison, the slopes of the black log-log plots showed values below 1. The concentration dependency is more drastic for Axin1 than Fzd8, which could be attributed to Axin1 oligomers by Axin1 polymerization during liquid-liquid phase separation^[159]. The lower slope for Fzd8 could be explained by the fact that Fzd8 was recruited indirectly by hetero-polymerization of Axin1 and endogenous Dvl2. The same analysis was employed to calculate the contrast dependency of Dvl2/Lrp6 and Fzd8/Lrp6 for the triple color Lrp6/Dvl2/Fzd8 experiment. However, the determination of thresholds was not straightforward as no significant difference was identified due to a deteriorated contrast of Dvl2 and Fzd8. Further investigations are required to reveal the exact reason for this behavior. For example, the endogenous expression level of Axin1/2 and Dvl1/2/3 in HeLa cells shall be taken into account.

It was already known that Axin1 binds to the phosphorylated intracellular domain (ICD) of Lrp6 in the canonical Wnt signaling. Our attempts of immunofluorescence (IF) staining of phosphorylated Lrp6 were not successful, most likely due to the process of IF staining and the

poor specificity of the primary dye-labeled anti-pLrp6 antibody. To determine whether the Axin1 recruitment to Lrp6 nanodots was depended on the phosphorylation of Lrp6, we designed a control experiment by using ICD-truncated Lrp6 (Lrp6 Δ ICD) in a triple-color TIRFM imaging of mEGFP-Lrp6 Δ ICD, td-mCherry-Axin1 and Snap-Tag-Fzd8. Since the 5 intracellular PPPSPxS/T motifs for phosphorylations are located in the intracellular domain of Lrp6, the Lrp6 Δ ICD nanodot in the control experiment was anticipated to show no recruitment of Axin1 and Fzd8.

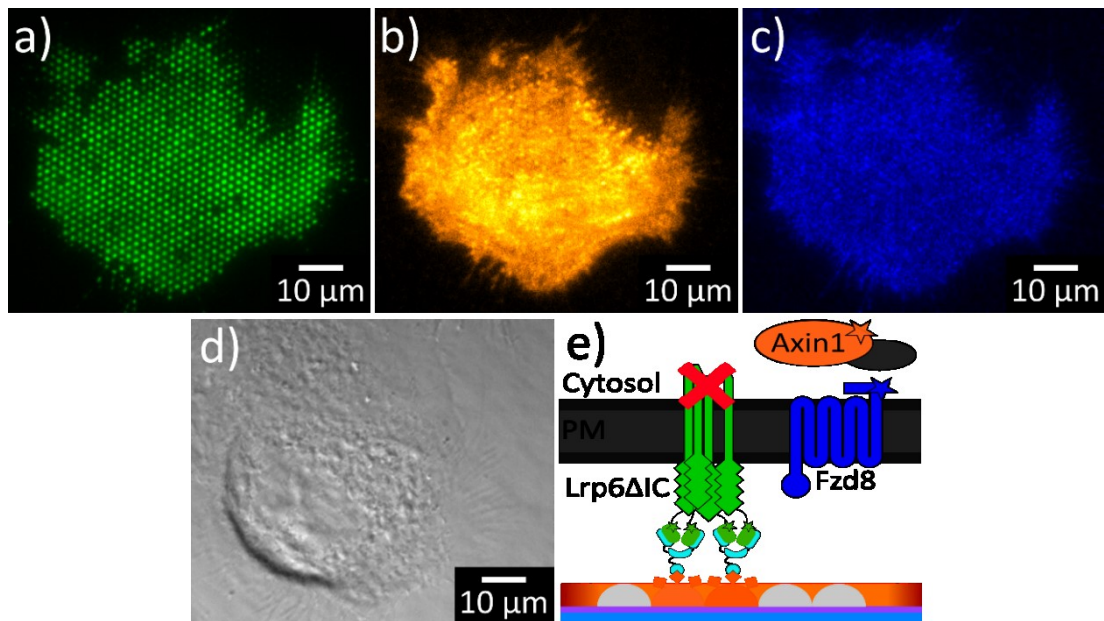


Figure 61: TIRFM of triple transfected HeLa cells exhibiting spatial reorganization of membrane-bound Lrp6 Δ ICD receptor but lacking the co-recruitment of Axin1 and Fzd8. a) mEGFP-Lrp6 b) td-mCherry-Axin1 c) Fzd8-DY647 d) DIC image. e) Schematic visualization of the triple color experiment with mEGFP-Lrp6 Δ ICD (green), Fzd8-DY647 (blue) and Axin1 (orange) on the BSA-HTL-dDARPin patterned surface.

The results in Figure 61 clearly show that the recruitment of Axin1 and Fzd8 to Lrp6 Δ ICD was strongly disrupted by the deletion of the intracellular domain of Lrp6. Only a faint pattern between the dots was visible in the Axin1 and Fzd8 channels due to deformations in the membrane induced by capturing the membrane-bound Lrp6 receptor. For all 16 analyzed cells, no significant contrast was determined with the colocalization analysis.

4.4.4.2 Immunofluorescence measurements of β -Catenin levels

In order to test the effectiveness of the patterned surfaces towards the activation of the Wnt pathway, β -catenin expression levels in HeLa cells were explored by immunofluorescence staining (IF). β -Catenin was stained with a dye-labeled primary antibody (Alexa Fluor 647) and analyzed with TIRFM under various conditions. In Figure 62, a HeLa cell transfected with Lrp6 and Fzd8 seeded onto a patterned coverslip can be seen.

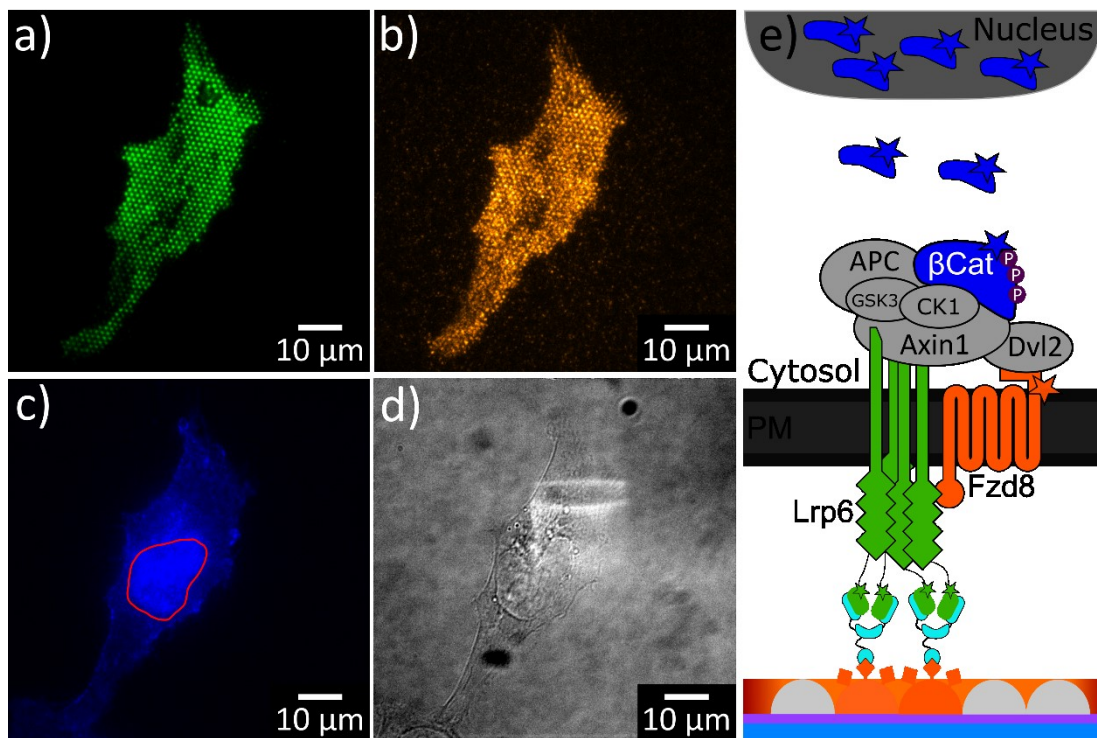


Figure 62: TIRF and widefield microscopy images of double transfected HeLa cells for IF staining of β -catenin on BSA-HTL-dDARPin functionalized surfaces. a) TIRFM image of mEGFP-Lrp6 b) TIRFM image of Fzd8-DY549. c) Widefield image of Alexa Fluor 647 labeled β -catenin. The marked area (red) shows the nucleus, adapted from the DIC image and used for IF measurements of the nucleus d) DIC image. e) Schematic visualization of IF measurements of β -catenin levels (blue) in double transfected HeLa (green: mEGFP-Lrp6; orange: Fzd8-DY549) cells. Wnt signaling stimulated by ligand-free clustering of Lrp6 on the dot array with an increase in β -catenin concentrations in the cytosol and nucleus.

The fluorescence intensities shown in the representative Figure 62c were compared to each other with respect to two positive controls, which were known for efficiently activating the Wnt signaling pathway. All results were normalized towards untransfected HeLa wild-type cells as a reference. HeLa cells were treated either with a GSK3-inhibitor (6-bromoindirubin-3'-oxime, BIO) or the next generation surrogate Wnt ligand (NGS) for positive controls. Treatment with the GSK3-inhibitor increased the β -catenin levels by inhibiting the phosphorylation of β -catenin and, as a consequence, ubiquitylation-mediated proteasomal degradation^[160]. The NGS was obtained from K.C. Garcia's lab and used as a potent Wnt surrogate ligand to induce the canonical Wnt signaling with low concentrations down to the nM range^[104].

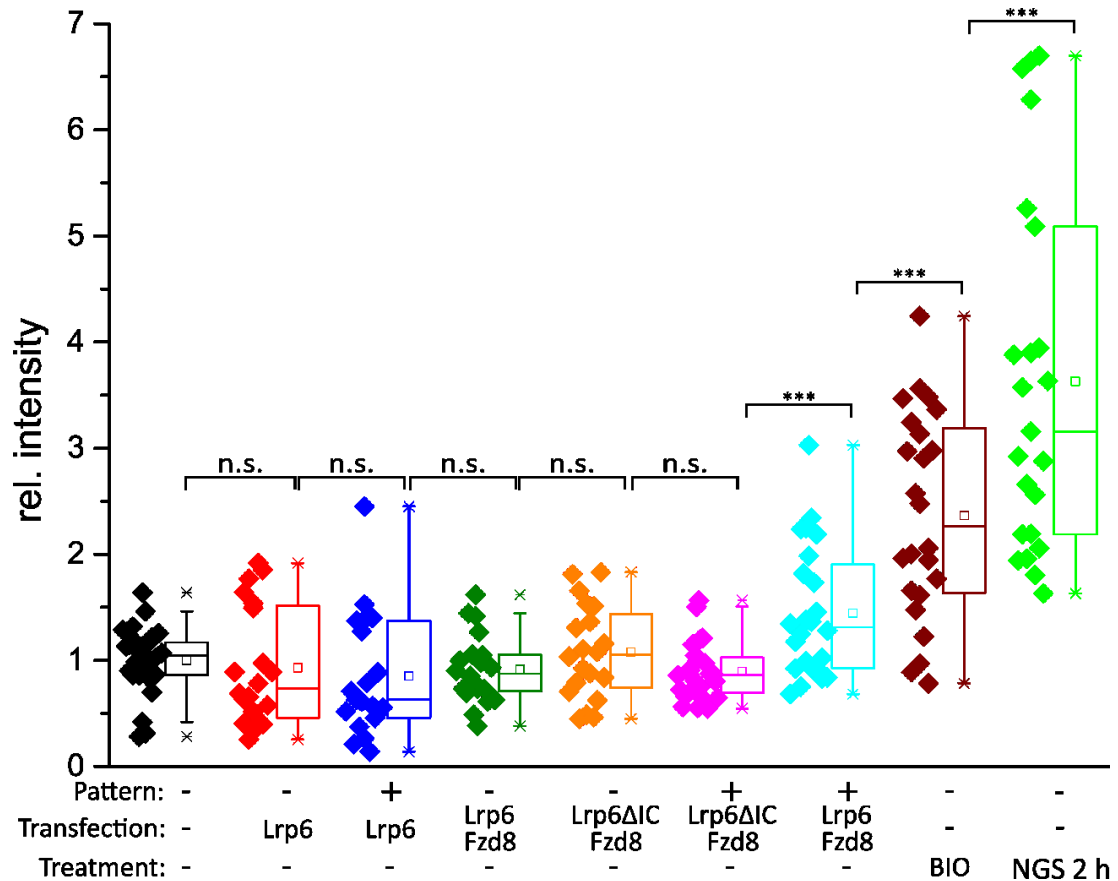


Figure 63: Intensity measurements taken from the whole-cell were normalized against the untransfected, unpatterned HeLa wt (black). Marks indicate how the cells and substrate were treated for each experiment separately (red: transfection with Lrp6, no pattern; blue: transfection with Lrp6, patterned; green: transfection with Lrp6 and Fzd8, no pattern; orange: transfection with Lrp6ΔIC and Fzd8, no pattern; magenta: transfection with Lrp6ΔIC and Fzd8, patterned; cyan: transfection with Lrp6 and Fzd8, patterned; brown: no transfection and no patterning, treatment with GSK3-inhibitor BIO; light green: no transfection and no patterning, treatment with NGS).

For the first set of measurements, the immunofluorescence of the whole cell was taken into account (Figure 63). HeLa cells transfected only with the Lrp6 receptor, either unpatterned or patterned (red, blue), did not show a significant increase in fluorescence intensity compared to the untransfected HeLa negative control. The broad distribution of the individual intensities, however, was comparably more significant, indicating subtle changes induced by Lrp6 transfection. These results showed that even though clustered Lrp6 could activate the Wnt signaling as reported previously, enrichment of higher levels of Lrp6 receptor in the nanodot arrays did not necessarily lead to downstream signaling without implementing the right conditions. Further control experiments with unpatterned but double transfected HeLa cells (dark green) and truncated Lrp6 (Lrp6ΔIC; orange, magenta) showed no significant increase in β -catenin levels. For the truncated version of Lrp6, the phosphorylation motif and, therefore, the binding site for Axin1 was removed.

To explore suitable conditions for Wnt signaling activation on nanodot arrays, a double transfection of the membrane-bound receptors Lrp6 and Fzd8 was employed (cyan). Under this circumstance, a noticeable increase in β -Catenin levels of 1.5 ± 0.6 fold (N=24) compared to the reference could be measured, suggesting a successful stimulation. However, the broad distribution of the fluorescence intensity showed that about half of the analyzed cells, even though featured with well-reorganized Lrp6 receptors on the nanodots, exhibited the same β -Catenin level as the negative control. This indicates that certain conditions, most likely a concentration threshold of the signaling relevant proteins, must be surpassed for successful signaling activation. Compared to the positive control measurements, which show an increase in the intensity of 2.4 ± 1.0 fold (N=24) for the GSK3 inhibited cells (brown) and 3.6 ± 1.9 fold (N=23) for the NGS treated cells (light green), the results of the β -Catenin level of the whole cell for Lrp6/Fzd8 co-expressed cells show a slightly lower intensity.

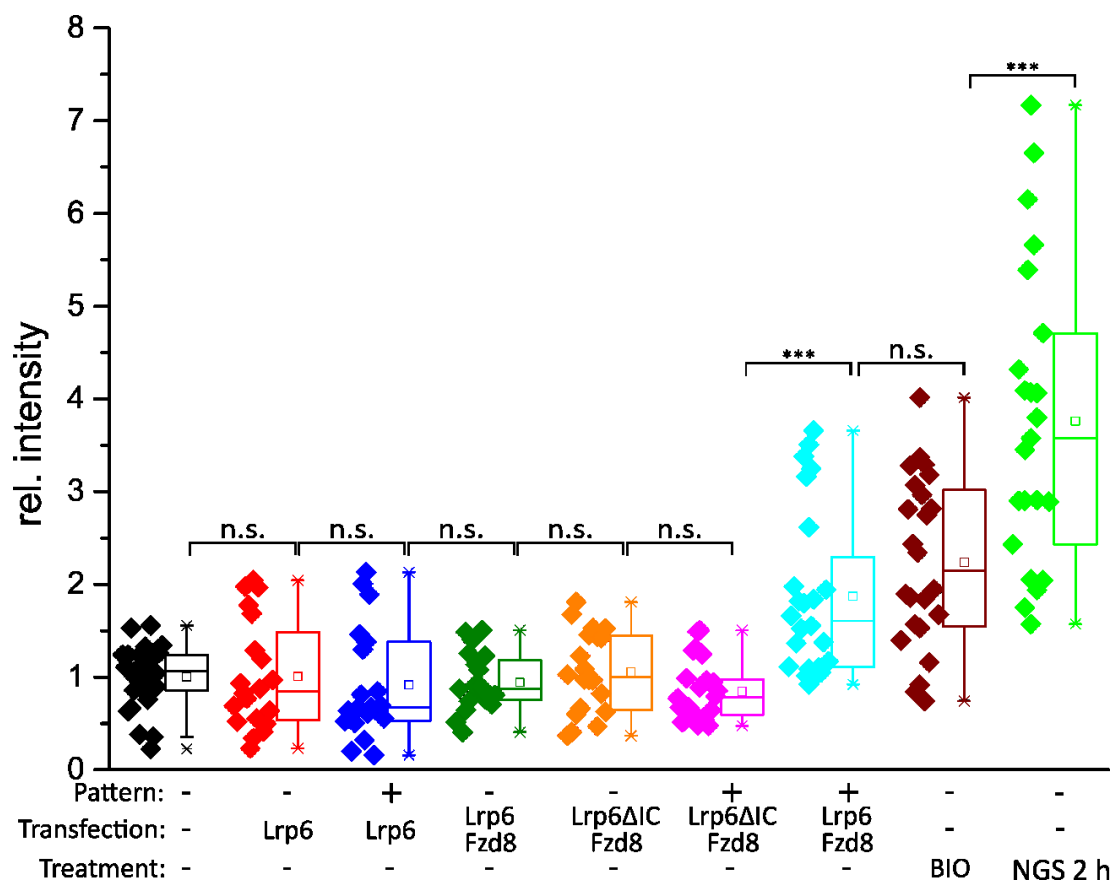


Figure 64: Intensity measurements are taken from the nucleus of each analyzed cell and are normalized against the untransfected, unpatterned HeLa wt (black). Marks indicate how the cells and substrate were treated for each experiment separately (red: transfection with Lrp6, no pattern; blue transfection with Lrp6, patterned; green: transfection with Lrp6 and Fzd8, no pattern; orange: transfection with Lrp6ΔICD and Fzd8, no pattern; magenta: transfection with Lrp6ΔICD and Fzd8, patterned; cyan: transfection with Lrp6 and Fzd8, patterned; brown: no transfection and no patterning, treatment with GSK3-inhibitor BIO; light green: no transfection and no patterning, treatment with NGS).

Because β -catenin translates into the nucleus to activate Wnt reporter genes, a higher concentration of β -catenin could be expected. Therefore, the fluorescence intensity of the same images was measured only within the boundaries of the nucleus based on DIC images (Figure 64). Every control experiment (red, dark green, orange, magenta) showed no significant difference compared to the cytosolic measurement. For the Lrp6/Fzd8 double transfected patterned cells, an intensity increase of 1.8 ± 0.9 fold (N=24, cyan) compared to the reference was observed. These values also showed no longer a significant difference to the GSK3-inhibited cells with 2.2 ± 0.9 (n=24, brown), even though they are still lower than the intensities from the Wnt surrogate NGS with 3.8 ± 1.6 fold (N=23, light green). Together, these results confirm the successful formation of Wnt signalosomes and activation of its downstream signaling by clustering of Lrp6 on the printed dot array in the presence of Fzd8. Based on the results from the control experiments, the ligand-free Wnt/ β -catenin signaling on nanodot arrays is triggered by immobilization of full-length Lrp6 and dependent on co-clustering of Fzd8.

5 Conclusion and outlook

Capillary stamping with mesoporous silica stamps is a newly developed technique that allows surface patterning below the one-micron range. The continuous pore system of the stamp with pores of ≈ 44 nm is synthesized *via* sol-gel chemistry of a trifunctional silica compound with a methyl residue. The pore system acts as an ink reservoir during stamping and allows consecutive patterning cycles under ambient conditions without reloading of the ink. In this work, the already diverse range of inks and the solvent range was extended further to print proteins out of an aqueous solution. Every patterned substrate exhibited features below one micron and was analyzed with regard to characteristic parameters. Patterned protein dot arrays were used to capture and concentrate proteins of choice at the cell membrane. This method was used to study protein-protein interactions and activation of downstream signaling of the canonical Wnt-signaling pathway.

The class of heterocyclic silanes, which undergo a ring-opening mechanism upon reaction with hydroxyl groups, was stamped from toluene. The reaction renders a functional group determined by the heteroatom of the silane exposed on the surface, which was then used for further modifications. Dye labeling of the heterocyclic silane dot array and analysis with TIRFM revealed that up to ten consecutive patterning cycles were possible without deterioration of the pattern quality. The best performing silane, the cycloazasilane, generated a pattern with an average area of $0.250 \mu\text{m}^2$ and a contrast of ≈ 3.2 in fluorescence images. The array was also post-functionalized with the biorthogonal HTL and utilized as a starting point for the polymerization of styrene. Although the polymerization of styrene and the resulting PS brushes only served as a model system, the polymerization technique (ATRP) is suitable for a wide range of monomers. Therefore, more intricate brush designs are imaginable. The introduction of the HTL and possible biological applications of the functional dot array proved the versatility and effectiveness of the stamping procedure in combination with heterocyclic silanes.

With the switch from organic solvents to water-based inks, direct stamping of proteins to the target substrate became available, paving the way for a broad application in biological studies. However, the switch of mediums also raises challenges. Most prominently, the wettability of the stamps and ink spreading on the substrate must be well controlled to support efficient ink loading of the stamps and maintain a high spatial resolution of the printed dots on the substrate. The optimizations were focused on these two aspects. As a proof of concept, dye-labeled SAV was patterned onto biotinylated glass slides with promising results. The average area of $\approx 0.207 \mu\text{m}^2$ for an SAV dot combined with a high circularity of ≈ 0.96 already demonstrated better values compared to dot arrays generated from organic solvents, which usually showed

less uniform and larger dot structures. For further improvements, BSA modified with HTL was printed onto various hydrophobically silanized glass surfaces in order to obtain the maximum surface loading of BSA with rapid adsorption, which jointly increased the contrast and spatial resolution of the nanodot arrays. Strikingly, the NMMS functionalized surface, modified by simple immersion into a 2 % naphthylmethyltrichlorosilane solution in toluene, showcased the fastest protein adsorption and the highest surface loading. Thus, it provides sufficient binding sites for future protein binders, which eventually will improve the contrast in fluorescence microscopy images. Patterning experiments on the NMMS silanized surfaces compared to the bare glass surfaces highlighted the beneficial impact of the hydrophobic coating on reducing dot size and pattern fidelity. In a following live-cell experiment, BSA-HTL patterns were able to recruit the HaloTag fused receptor IFNAR2 to the dot array by HaloTag/HTL interaction. Even though the membrane-anchored receptor protein was immobilized on the dot array, it was still functional and could specifically bind IFN α 2 as the ligand. In this thesis, capillary printing on hydrophobically treated surfaces was furthermore extended as a generic nanolithography method. BSA-HTL was also patterned onto a graphene monolayer-coated glass and subsequently labeled with a fluorescence dye. Graphene-induced energy transfer (GIET) has emerged recently as a unique method to measure axial distances in an extended 30 nm range^[150,161]. The spatially resolved protein capturing obtained by capillary stamping combined with GIET could be a powerful tool for future investigations of protein-protein interactions and protein structural dynamics. By fusing the HaloTag to two anti-GFP DARPin, the engineered protein binder improved binding capacity drastically and exhibited the best pattern quality in this work. Notably, the contrast increased to ≈ 10 . The dot size decrease to $0.196 \mu\text{m}^2$ combined with a low standard deviation of $\pm 0.024 \mu\text{m}^2$, a circularity of ≈ 0.99 and an aspect ratio of ≈ 1.14 underlines the effectiveness of this modification. The DARPin was designed to have a high affinity towards the β -barrel of GFP protein, and itself is very robust under cell culture conditions at 37°C . This property was exploited to promote high contrast fluorescence microscopy imaging of GFP fused to proteins of interest in live cells. For instance, the activation of the canonical Wnt signaling in live cells by the nanodot arrays. HeLa cells transfected with mEGFP-Lrp6 exhibited significant spatial reorganization of the transmembrane receptor Lrp6 via the extracellular mEGFP with the HaloTag-dDARPin.

After establishing the capillary nanostamping methodologies, the system was combined with the optogenetic iLID toolbox to demonstrate the manipulation of protein organizations in live cells. The iLID-based optogenetic approach yielded patterns switchable between an OFF state in the darkness and an ON state by illumination with 488 nm light for at least ten consecutive

cycles. Strikingly, each cycle displayed a full recovery of its intensity signal, although with a modest contrast between the two states.

Next, the capillary stamping method was employed to investigate the canonical Wnt signaling pathway. Using the HaloTag-dDARPin nanodot arrays, reorganizations of the Wnt signaling relevant proteins in the plasma membrane of live cells were carried out. These experiments were set to provide molecular insight into the spatial reorganization of four key proteins during Wnt signaling. They are Lrp6, Fzd8 as the transmembrane co-receptors located in the plasma membrane and Axin1, Dvl2, which are the cytosolic scaffold proteins of the destruction complex for degradation of the transcription factor β -catenin. According to the known diagram for Wnt signaling activation, Axin1 and Dvl2 are supposed to be recruited to the Wnt ligand-induced heterodimers of Lrp6 and Fzd8 at the plasma membrane. The results on the nanodot arrays support the as-depicted signaling pathway in a ligand-free manner. By enriching Lrp6 in the nanodots, the co-receptor Fzd8 and the cytosolic effector proteins of Dvl2 or Axin1 were recruited to the nanodot array in the absence of Wnt ligand. Triple-color imaging also showed overlapping of Lrp6/Fzd8/Dvl2 and Lrp6/Fzd8/Axin1. Colocalization intensity analyses of these triple-color images revealed stronger recruitment of Axin1 than Fzd8, suggesting a major role played by Axin1 for recruitment of the destruction complex to the plasma membrane. By immunofluorescence staining of β -Catenin, significantly increased β -Catenin levels, especially in the nucleus, were detected for Lrp6/Fzd8 double transfected HeLa cells on patterned surfaces. These results unambiguously confirmed the formation of canonical Wnt signalosome on the nanodot arrays with a defined spatial arrangement. Recent reports emphasized that liquid-liquid phase separations (LLPS) of Axin1 and Dvl2 in cytosol play essential roles during Wnt signaling^[159,162]. The spatially resolved Wnt signalosome nanodot array established here could be a very useful platform for exploring molecular mechanisms about the interplay between protein phase separations in the cytosol and the plasma membrane. Future work in this direction will contribute to an in-depth understanding of 3-D phase separation of proteins in the cytosol with 2-D phase separation of transmembrane receptors and lipids at the plasma membrane for Wnt signaling.

In summary, capillary stamping with mesoporous silica stamps has been proved to be a versatile large-scale nanolithography platform using different kinds of inks. Combined with the fast development of protein binders such as ALFA-tag, Spy-Tag, etc., different protein-based inks could be engineered for multiplex stamping with orthogonal binding specificity. These developments would meet the requirements needed for in-depth analysis of cell signaling pathways and the high throughput analysis of protein-protein interactions.

6 References

- [1] G. E. Moore, *IEEE Solid-State Circuits Soc. Newsl.*, **2006**, *11*, 3, 33.
- [2] S. X. Jin, J. Li, J. Z. Li, J. Y. Lin, H. X. Jiang, *Appl. Phys. Lett.*, **2000**, *76*, 5, 631.
- [3] T. Heyduk, *Biophys. Chem.*, **2010**, *151*, 3, 91.
- [4] I. M. Miron, K. Garello, G. Gaudin, P.-J. Zermatten, M. V. Costache, S. Auffret, S. Bandiera, B. Rodmacq, A. Schuhl, P. Gambardella, *Nature*, **2011**, *476*, 7359, 189.
- [5] M. M. Bellah, S. M. Christensen, S. M. Iqbal, *J. Nanomater.*, **2012**, *2012*, 1.
- [6] Y. Xia, G. M. Whitesides, *Angew. Chem. Int. Ed.*, **1998**, *37*, 5, 550.
- [7] S. Hashioka, M. Saito, E. Tamiya, H. Matsumura, *J. Vac. Sci. Technol. B*, **2003**, *21*, 6, 2937.
- [8] S. Cabrini, A. Carpentiero, R. Kumar, L. Businaro, P. Candeloro, M. Prasciolu, A. Gosparini, C. Andreani, M. de Vittorio, T. Stomeo, E. Di Fabrizio, *Microelectron. Eng.*, **2005**, *78-79*, 11.
- [9] T. Kaufmann, B. J. Ravoo, *Polym. Chem.*, **2010**, *1*, 4, 371.
- [10] B. Olander, A. Wirsen, A.-C. Albertsson, *J. Appl. Polym. Sci.*, **2004**, *91*, 6, 4098.
- [11] E. Delamarche, C. Donzel, F. S. Kamounah, H. Wolf, M. Geissler, R. Stutz, P. Schmidt-Winkel, B. Michel, H. J. Mathieu, K. Schaumburg, *Langmuir*, **2003**, *19*, 21, 8749.
- [12] C. D. James, R. C. Davis, L. Kam, H. G. Craighead, M. Isaacson, J. N. Turner, W. Shain, *Langmuir*, **1998**, *14*, 4, 741.
- [13] D. C. Trimbach, H. Stapert, J. van Orselen, K. D. Jandt, C. W. M. Bastiaansen, D. J. Broer, *Adv. Eng. Mater.*, **2007**, *9*, 12, 1123.
- [14] F. Huo, Z. Zheng, G. Zheng, L. R. Giam, H. Zhang, C. A. Mirkin, *Science*, **2008**, *321*, 5896, 1658.
- [15] Piner, Zhu, Xu, Hong, Mirkin, *Science*, **1999**, *283*, 5402, 661.
- [16] M. Schmidt, M. Philippi, M. Münzner, J. M. Stangl, R. Wieczorek, W. Harneit, K. Müller-Buschbaum, D. Enke, M. Steinhart, *Adv. Funct. Mater.*, **2018**, *28*, 23, 1800700.
- [17] D. Kim, J. M. Zuidema, J. Kang, Y. Pan, L. Wu, D. Warther, B. Arkles, M. J. Sailor, *J. Am. Chem. Soc.*, **2016**, *138*, 46, 15106.
- [18] S. Reyntjens, R. Puers, *J. Micromech. Microeng.*, **2001**, *11*, 4, 287.
- [19] C. M. Kolodziej, H. D. Maynard, *Chem. Mater.*, **2012**, *24*, 5, 774.
- [20] G. Liu, S. H. Petrosko, Z. Zheng, C. A. Mirkin, *Chem. Rev.*, **2020**, *120*, 6009.
- [21] Y. Li, B. W. Maynor, J. Liu, *J. Am. Chem. Soc.*, **2001**, *123*, 9, 2105.
- [22] P. E. Sheehan, L. J. Whitman, W. P. King, B. A. Nelson, *Appl. Phys. Lett.*, **2004**, *85*, 9, 1589.
- [23] N. A. Amro, S. Xu, G. Liu, *Langmuir*, **2000**, *16*, 7, 3006.
- [24] K. Salaita, S. W. Lee, X. Wang, L. Huang, T. M. Dellinger, C. Liu, C. A. Mirkin, *Small*, **2005**, *1*, 10, 940.

- [25] N. J. Wilkinson, M. A. A. Smith, R. W. Kay, R. A. Harris, *Int. J. Adv. Manuf. Technol.*, **2019**, *105*, 11, 4599.
- [26] B. Derby, *Annu. Rev. Mater. Res.*, **2010**, *40*, 1, 395.
- [27] Z. Hu, Y. Yin, M. U. Ali, W. Peng, S. Zhang, D. Li, T. Zou, Y. Li, S. Jiao, S.-J. Chen, C.-Y. Lee, H. Meng, H. Zhou, *Nanoscale*, **2020**, *12*, 3, 2103.
- [28] T.-C. Wu, J. Dai, G. Hu, W.-B. Yu, O. Ogbeide, A. de Luca, X. Huang, B.-L. Su, Y. Li, F. Udreă, T. Hasan, *Sens. Actuators B Chem.*, **2020**, *321*, 128446.
- [29] X. Cui, T. Boland, D. D. D'Lima, M. K. Lotz, *Recent Pat. Drug. Deliv. Formul.*, **2012**, *6*, 2, 149.
- [30] M. Y. Teo, L. Stuart, K. C. Aw, J. Stringer, *MRS Adv.*, **2018**, *3*, 28, 1575.
- [31] J. B. Delehanty, F. S. Ligler, *Anal. Chem.*, **2002**, *74*, 21, 5681.
- [32] Z. Yin, Y. Huang, N. Bu, X. Wang, Y. Xiong, *Chin. Sci. Bull.*, **2010**, *55*, 30, 3383.
- [33] J. H. Pikul, P. Graf, S. Mishra, K. Barton, Y.-K. Kim, J. A. Rogers, A. Alleyne, P. M. Ferreira, W. P. King, *IEEE Sensors J.*, **2011**, *11*, 10, 2246.
- [34] Y. Shi, W. Wang, *Mater. Lett.*, **2020**, *261*, 127131.
- [35] D. Graf, S. Burchard, J. Crespo, C. Megnin, S. Gutsch, M. Zacharias, T. Hanemann, *Polymers*, **2019**, *11*, 4, 633.
- [36] A. Perl, D. N. Reinhoudt, J. Huskens, *Adv. Mater.*, **2009**, *21*, 22, 2257.
- [37] A. Kumar, G. M. Whitesides, *Appl. Phys. Lett.*, **1993**, *63*, 14, 2002.
- [38] V. Santhanam, J. Liu, R. Agarwal, R. P. Andres, *Langmuir*, **2003**, *19*, 19, 7881.
- [39] T. Granlund, T. Nyberg, L. Stolz Roman, M. Svensson, O. Inganäs, *Adv. Mater.*, **2000**, *12*, 4, 269.
- [40] F. Zhou, Z. Zheng, B. Yu, W. Liu, W. T. S. Huck, *J. Am. Chem. Soc.*, **2006**, *128*, 50, 16253.
- [41] H. Hillborg, M. Sandelin, U. W. Gedde, *Polymer*, **2001**, *42*, 17, 7349.
- [42] S. A. Lange, V. Benes, D. P. Kern, J. K. H. Hörber, A. Bernard, *Anal. Chem.*, **2004**, *76*, 6, 1641.
- [43] P. M. St John, R. Davis, N. Cady, J. Czajka, C. A. Batt, H. G. Craighead, *Anal. Chem.*, **1998**, *70*, 6, 1108.
- [44] J. Chalmeau, L. Salomé, C. Thibault, C. Severac, C. Vieu, *Microelectron. Eng.*, **2007**, *84*, 5-8, 1754.
- [45] D. Qin, Y. Xia, G. M. Whitesides, *Nat. Protoc.*, **2010**, *5*, 3, 491.
- [46] H. Schmid, B. Michel, *Macromolecules*, **2000**, *33*, 8, 3042.
- [47] G. Csucs, T. Künzler, K. Feldman, F. Robin, N. D. Spencer, *Langmuir*, **2003**, *19*, 15, 6104.
- [48] S.-J. Choi, P. J. Yoo, S. J. Baek, T. W. Kim, H. H. Lee, *J. Am. Chem. Soc.*, **2004**, *126*, 25, 7744.
- [49] X. Liao, A. B. Braunschweig, C. A. Mirkin, *Nano Lett.*, **2010**, *10*, 4, 1335.

- [50] H. Noh, G.-E. Jung, S. Kim, S.-H. Yun, A. Jo, S.-J. Kahng, N.-J. Cho, S.-J. Cho, *Small*, **2015**, *11*, 4526.
- [51] F. Brinkmann, M. Hirtz, A. M. Greiner, M. Weschenfelder, B. Waterkotte, M. Bastmeyer, H. Fuchs, *Small*, **2013**.
- [52] Z. Xie, Y. Shen, X. Zhou, Y. Yang, Q. Tang, Q. Miao, J. Su, H. Wu, Z. Zheng, *Small*, **2012**, *8*, 17, 2664.
- [53] X. Zhong, N. A. Bailey, K. B. Schesing, S. Bian, L. M. Campos, A. B. Braunschweig, *J. Polym. Sci. A Polym. Chem.*, **2013**, *51*, 7, 1533.
- [54] J. L. Hedrick, K. A. Brown, E. J. Kluender, M. D. Cabezas, P.-C. Chen, C. A. Mirkin, *ACS Nano*, **2016**, *10*, 3144.
- [55] A. Angelin, U. Bog, R. Kumar, C. M. Niemeyer, M. Hirtz, *Polymers*, **2019**.
- [56] U. Bog, A. de Los Santos Pereira, S. L. Mueller, S. Havenridge, V. Parrillo, M. Bruns, A. E. Holmes, C. Rodriguez-Emmenegger, H. Fuchs, M. Hirtz, *ACS Appl. Mater. Interfaces*, **2017**.
- [57] H. Xu, X. Y. Ling, J. van Bennekom, X. Duan, M. J. W. Ludden, D. N. Reinhoudt, M. Wessling, R. G. H. Lammertink, J. Huskens, *J. Am. Chem. Soc.*, **2009**, *131*, 2, 797.
- [58] M. Runge, H. Hübner, A. Grimm, G. Manoharan, R. Wieczorek, M. Philippi, W. Harneit, C. Meyer, D. Enke, M. Gallei, M. Steinhart, *Adv. Mater. Interfaces*, **2021**, *8*, 5, 2001911.
- [59] P. Hou, R. Kumar, B. Oberleiter, R. Kohns, D. Enke, U. Beginn, H. Fuchs, M. Hirtz, M. Steinhart, *Adv. Funct. Mater.*, **2020**, *30*, 25, 2001531.
- [60] J. Zhu, J. Hiltz, U. M. Tefashe, J. Mauzeroll, R. B. Lennox, *Chem. Eur. J.*, **2018**, *24*, 35, 8904.
- [61] E. P. Yalcintas, K. B. Ozutemiz, T. Cetinkaya, L. Dalloro, C. Majidi, O. B. Ozdoganlar, *Adv. Funct. Mater.*, **2019**, *29*, 51, 1906551.
- [62] C. Buten, S. Lamping, M. Körsgen, H. F. Arlinghaus, C. Jamieson, B. J. Ravoo, *Langmuir*, **2018**, *34*, 5, 2132.
- [63] M. Ermis, E. Antmen, V. Hasirci, *Bioact. Mater.*, **2018**, *3*, 3, 355.
- [64] E. Phizicky, P. I. H. Bastiaens, H. Zhu, M. Snyder, S. Fields, *Nature*, **2003**, *422*, 6928, 208.
- [65] C. You, J. Piehler, *Expert Opin. Drug Discov.*, **2016**, *11*, 1, 105.
- [66] M. Schena, D. Shalon, R. W. Davis, P. O. Brown, *Science*, **1995**, *270*, 5235, 467.
- [67] H. A. Rothan, T. C. Teoh, *Mol. Biotechnol.*, **2021**, *63*, 3, 240.
- [68] L. Casalino, D. Magnani, S. de Falco, S. Filosa, G. Minchiotti, E. J. Patriarca, D. de Cesare, *Mol. Biotechnol.*, **2012**, *50*, 3, 171.
- [69] V. Lecault, M. Vaninsberghe, S. Sekulovic, D. J. H. F. Knapp, S. Wohrer, W. Bowden, F. Viel, T. McLaughlin, A. Jarandehi, M. Miller, D. Falconnet, A. K. White, D. G. Kent, M. R. Copley, F. Taghipour, C. J. Eaves, R. K. Humphries, J. M. Piret, C. L. Hansen, *Nat. Methods*, **2011**, *8*, 7, 581.

- [70] A. A. Popova, S. M. Schillo, K. Demir, E. Ueda, A. Nesterov-Mueller, P. A. Levkin, *Adv. Mater.*, **2015**, *27*, 35, 5217.
- [71] A. I. Neto, C. A. Custódio, W. Song, J. F. Mano, *Soft Matter*, **2011**, *7*, 9, 4147.
- [72] W. Feng, L. Li, E. Ueda, J. Li, S. Heißler, A. Welle, O. Trapp, P. A. Levkin, *Adv. Mater. Interfaces*, **2014**, *1*, 7, 1400269.
- [73] B. Chang, O. Kivinen, I. Pini, P. A. Levkin, R. H. A. Ras, Q. Zhou, *Soft Matter*, **2018**, *14*, 36, 7500.
- [74] R. J. Jackman, D. C. Duffy, E. Ostuni, N. D. Willmore, G. M. Whitesides, *Anal. Chem.*, **1998**, *70*, 11, 2280.
- [75] M. Tutkus, T. Rakickas, A. Kopu Stas, Š. N. Ivanovaitė, O. Venckus, V. Navikas, M. Zaremba, E. Manakova, R. N. Valiokas, *Langmuir*, **2019**, *35*, 17, 5921.
- [76] T. Fazio, M.-L. Visnapuu, S. Wind, E. C. Greene, *Langmuir*, **2008**, *24*, 18, 10524.
- [77] L. C. Kam, K. Shen, M. L. Dustin, *Annu. Rev. Biomed. Eng.*, **2013**, *15*, 305.
- [78] T. Satav, J. Huskens, P. Jonkheijm, *Small*, **2015**, *11*, 39, 5184.
- [79] T. Wedeking, S. Löchte, C. P. Richter, M. Bhagawati, J. Piehler, C. You, *Nano Lett.*, **2015**, *15*, 5, 3610.
- [80] L. F. Stancato, M. David, C. Carter-Su, A. C. Lerner, W. B. Pratt, *J. Biol. Chem.*, **1996**, *271*, 8, 4134.
- [81] A. Jain, R. Liu, B. Ramani, E. Arauz, Y. Ishitsuka, K. Ragunathan, J. Park, J. Chen, Y. K. Xiang, T. Ha, *Nature*, **2011**, *473*, 7348, 484.
- [82] S. Löchte, S. Waichman, O. Beutel, C. You, J. Piehler, *J. Cell Biol.*, **2014**, *207*, 3, 407.
- [83] M. Schwarzenbacher, M. Kaltenbrunner, M. Brameshuber, C. Hesch, W. Paster, J. Weghuber, B. Heise, A. Sonnleitner, H. Stockinger, G. J. Schütz, *Nat. Methods*, **2008**, *5*, 12, 1053.
- [84] E. Sevcsik, M. Brameshuber, M. Fölser, J. Weghuber, A. Honigmann, G. J. Schütz, *Nat. Commun.*, **2015**, *6*, 6969.
- [85] C. Dirscherl, R. Palankar, M. Delcea, T. A. Kolesnikova, S. Springer, *Small*, **2017**, *13*, 15, 1602974.
- [86] C. S. Chen, M. Mrksich, S. Huang, G. M. Whitesides, D. E. Ingber, *Science*, **1997**, *276*, 5317, 1425.
- [87] C. J. Bettinger, R. Langer, J. T. Borenstein, *Angew. Chem. Int. Ed.*, **2009**, *48*, 30, 5406.
- [88] V. Fitzpatrick, L. Fourel, O. Destaing, F. Gilde, C. Albigès-Rizo, C. Picart, T. Boudou, *Sci. Rep.*, **2017**, *7*, 41479.
- [89] Z. Chen, D. Oh, K. H. Biswas, C.-H. Yu, R. Zaidel-Bar, J. T. Groves, *Proc. Natl. Acad. Sci. USA*, **2018**, *115*, 25, E5696-E5705.

- [90] M. Arnold, V. C. Hirschfeld-Warneken, T. Lohmüller, P. Heil, J. Blümmel, E. A. Cavalcanti-Adam, M. López-García, P. Walther, H. Kessler, B. Geiger, J. P. Spatz, *Nano Lett.*, **2008**, *8*, 7, 2063.
- [91] E. H. Schwab, T. L. M. Pohl, T. Haraszti, G. K. Schwaerzer, C. Hiepen, J. P. Spatz, P. Knaus, E. A. Cavalcanti-Adam, *Nano Lett.*, **2015**, *15*, 3, 1526.
- [92] X. Wang, S. Li, C. Yan, P. Liu, J. Ding, *Nano Lett.*, **2015**, *15*, 3, 1457.
- [93] T. C. Rao, V. P.-Y. Ma, A. Blanchard, T. M. Urner, S. Grandhi, K. Salaita, A. L. Mattheyses, *J. Cell. Sci.*, **2020**, *133*, 13, jcs238840.
- [94] A. Klaus, W. Birchmeier, *Nat. Rev. Cancer*, **2008**, *8*, 5, 387.
- [95] B. T. MacDonald, K. Tamai, X. He, *Dev. Cell*, **2009**, *17*, 1, 9.
- [96] Y. Komiya, R. Habas, *Organogenesis*, **2008**, *4*, 2, 68.
- [97] M. V. Semenov, R. Habas, B. T. MacDonald, X. He, *Cell*, **2007**, *131*, 7, 1378.
- [98] R. Takada, Y. Satomi, T. Kurata, N. Ueno, S. Norioka, H. Kondoh, T. Takao, S. Takada, *Dev. Cell*, **2006**, *11*, 6, 791.
- [99] K. Willert, J. D. Brown, E. Danenberg, A. W. Duncan, I. L. Weissman, T. Reya, J. R. Yates, R. Nusse, *Nature*, **2003**, *423*, 6938, 448.
- [100] H. F. Farin, I. Jordens, M. H. Mosa, O. Basak, J. Korving, D. V. F. Tauriello, K. de Punder, S. Angers, P. J. Peters, M. M. Maurice, H. Clevers, *Nature*, **2016**, *530*, 7590, 340.
- [101] H.-C. Huang, P. S. Klein, *Genome Biol.*, **2004**, *5*, 7, 234.
- [102] Z. Cheng, T. Biechele, Z. Wei, S. Morrone, R. T. Moon, L. Wang, W. Xu, *Nat. Struct. Mol. Biol.*, **2011**, *18*, 11, 1204.
- [103] C. Y. Janda, L. T. Dang, C. You, J. Chang, W. de Lau, Z. A. Zhong, K. S. Yan, O. Marecic, D. Siepe, X. Li, J. D. Moody, B. O. Williams, H. Clevers, J. Piehler, D. Baker, C. J. Kuo, K. C. Garcia, *Nature*, **2017**, *545*, 7653, 234.
- [104] Y. Miao, A. Ha, W. de Lau, K. Yuki, A. J. M. Santos, C. You, M. H. Geurts, J. Puschhof, C. Pleguezuelos-Manzano, W. C. Peng, R. Senlice, C. Piani, J. W. Buikema, O. M. Gbenedio, M. Vallon, J. Yuan, S. de Haan, W. Hemrika, K. Rösch, L. T. Dang, D. Baker, M. Ott, P. Depeille, S. M. Wu, J. Drost, R. Nusse, J. P. Roose, J. Piehler, S. F. Boj, C. Y. Janda, H. Clevers, C. J. Kuo, K. C. Garcia, *Cell Stem Cell*, **2020**, *27*, 5, 840-851.e6.
- [105] T. Valenta, G. Hausmann, K. Basler, *EMBO J.*, **2012**, *31*, 12, 2714.
- [106] R. Nusse, H. Clevers, *Cell*, **2017**, *169*, 6, 985.
- [107] D. V. F. Tauriello, I. Jordens, K. Kirchner, J. W. Sloodstra, T. Kruitwagen, B. A. M. Bouwman, M. Noutsou, S. G. D. Rüdiger, K. Schwamborn, A. Schambony, M. M. Maurice, *Proc. Natl. Acad. Sci. USA*, **2012**, *109*, 14, E812-20.
- [108] L. Fenno, O. Yizhar, K. Deisseroth, *Annu. Rev. Neurosci.*, **2011**, *34*, 389.

- [109] K. Deisseroth, G. Feng, A. K. Majewska, G. Miesenböck, A. Ting, M. J. Schnitzer, *J. Neurosci.*, **2006**, *26*, 41, 10380.
- [110] K. Zhang, B. Cui, *Trends Biotechnol.*, **2015**, *33*, 2, 92.
- [111] K. Zhang, L. Duan, Q. Ong, Z. Lin, P. M. Varman, K. Sung, B. Cui, *PLoS One*, **2014**, *9*, 3, e92917.
- [112] M. Yazawa, A. M. Sadaghiani, B. Hsueh, R. E. Dolmetsch, *Nat. Biotechnol.*, **2009**, *27*, 10, 941.
- [113] C. Renicke, D. Schuster, S. Usherenko, L.-O. Essen, C. Taxis, *Chem. Biol.*, **2013**, *20*, 4, 619.
- [114] M. J. Kennedy, R. M. Hughes, L. A. Peteya, J. W. Schwartz, M. D. Ehlers, C. L. Tucker, *Nat. Methods*, **2010**, *7*, 12, 973.
- [115] L. J. Bugaj, A. T. Choksi, C. K. Mesuda, R. S. Kane, D. V. Schaffer, *Nat. Methods*, **2013**, *10*, 3, 249.
- [116] S. Shimizu-Sato, E. Huq, J. M. Tepperman, P. H. Quail, *Nat. Biotechnol.*, **2002**, *20*, 10, 1041.
- [117] A. Levskaya, O. D. Weiner, W. A. Lim, C. A. Voigt, *Nature*, **2009**, *461*, 7266, 997.
- [118] X. X. Zhou, H. K. Chung, A. J. Lam, M. Z. Lin, *Science*, **2012**, *338*, 6108, 810.
- [119] J. Hühner, Á. Ingles-Prieto, C. Neusüß, M. Lämmerhofer, H. Janovjak, *Electrophoresis*, **2015**, *36*, 4, 518.
- [120] S. M. Harper, L. C. Neil, K. H. Gardner, *Science*, **2003**, *301*, 5639, 1541.
- [121] G. Guntas, R. A. Hallett, S. P. Zimmerman, T. Williams, H. Yumerefendi, J. E. Bear, B. Kuhlman, *Proc. Natl. Acad. Sci. USA*, **2015**, *112*, 1, 112.
- [122] S. P. Zimmerman, R. A. Hallett, A. M. Bourke, J. E. Bear, M. J. Kennedy, B. Kuhlman, *Biochemistry*, **2016**, *55*, 37, 5264.
- [123] S. M. Bartelt, J. Steinkühler, R. Dimova, S. V. Wegner, *Nano Lett.*, **2018**, *18*, 11, 7268.
- [124] J. M. Hope, A. Liu, G. J. Calvin, B. Cui, *J. Mol. Biol.*, **2020**, *432*, 13, 3739.
- [125] M. Ovesný, P. Křížek, J. Borkovec, Z. Svindrych, G. M. Hagen, *Bioinformatics (Oxford, England)*, **2014**, *30*, 16, 2389.
- [126] N. Otsu, *IEEE Trans. Syst., Man, Cybern.*, **1979**, *9*, 1, 62.
- [127] M. Gavutis, S. Lata, J. Piehler, *Nat. Protoc.*, **2006**, *1*, 4, 2091.
- [128] J. Piehler, G. Schreiber, *Anal. Biochem.*, **2001**, *289*, 2, 173.
- [129] D. Lisse, V. Wilkens, C. You, K. Busch, J. Piehler, *Angew. Chem. Int. Ed.*, **2011**, *50*, 40, 9352.
- [130] Y. Pan, A. Maddox, T. Min, F. Gonzaga, J. Goff, B. Arkles, *Chem. Asian J.*, **2017**, *12*, 11, 1198.

- [131] L. Ju, N. C. Strandwitz, *J. Mater. Chem. C*, **2016**, *4*, 18, 4034.
- [132] R. G. Acres, A. V. Ellis, J. Alvino, C. E. Lenahan, D. A. Khodakov, G. F. Metha, G. G. Andersson, *J. Phys. Chem. C*, **2012**, *116*, 10, 6289.
- [133] K. M. R. Kallury, J. D. Brennan, U. J. Krull, *Anal. Chem.*, **1995**, *67*, 15, 2625.
- [134] Y. Araujo, P. G. Toledo, V. Leon, H. Y. Gonzalez, *J. Coll. Interf. Sci.*, **1995**, *176*, 2, 485.
- [135] T. L. Barr, S. Seal, *J. Vac. Sci. Technol. A*, **1995**, *13*, 3, 1239.
- [136] W. Jakubowski, K. Min, K. Matyjaszewski, *Macromolecules*, **2006**, *39*, 1, 39.
- [137] L. Mueller, K. Matyjaszewski, *Macromol. React. Eng.*, **2010**, *4*, 3-4, 180.
- [138] Y. Li, Q. Li, C. Zhang, P. Cai, N. Bai, X. Xu, *Chem. Eng. J.*, **2017**, *323*, 134.
- [139] R. F. Delgadillo, T. C. Mueser, K. Zaleta-Rivera, K. A. Carnes, J. González-Valdez, L. J. Parkhurst, *PLoS One*, **2019**, *14*, 2, e0204194.
- [140] T. Lloyd, M. A. Walega, *Anal. Biochem.*, **1981**, *116*, 2, 559.
- [141] D.-H. Tsai, F. W. DelRio, A. M. Keene, K. M. Tyner, R. I. MacCusprie, T. J. Cho, M. R. Zachariah, V. A. Hackley, *Langmuir*, **2011**, *27*, 6, 2464.
- [142] B. C. Bunker, R. W. Carpick, R. A. Assink, M. L. Thomas, M. G. Hankins, J. A. Voigt, D. Sipola, M. P. de Boer, G. L. Gulley, *Langmuir*, **2000**, *16*, 20, 7742.
- [143] M. Heilemann, S. van de Linde, M. Schüttpelz, R. Kasper, B. Seefeldt, A. Mukherjee, P. Tinnefeld, M. Sauer, *Angew. Chem. Int. Ed.*, **2008**, *47*, 33, 6172.
- [144] G. T. Dempsey, J. C. Vaughan, K. H. Chen, M. Bates, X. Zhuang, *Nat. Methods*, **2011**, *8*, 12, 1027.
- [145] M. Brauchle, S. Hansen, E. Caussin, A. Lenard, A. Ochoa-Espinosa, O. Scholz, S. G. Sprecher, A. Plückthun, M. Affolter, *Biol. Open*, **2014**, *3*, 12, 1252.
- [146] S. Hansen, J. C. Stüber, P. Ernst, A. Koch, D. Bojar, A. Batyuk, A. Plückthun, *Sci. Rep.*, **2017**, *7*, 1, 16292.
- [147] Y. Peng, B. Lu, S. Chen, *Adv. Mater.*, **2018**, *30*, 48, e1801995.
- [148] A. T. Lawal, *Biosens. Bioelectron.*, **2019**, *141*, 111384.
- [149] E. Cesewski, B. N. Johnson, *Biosens. Bioelectron.*, **2020**, *159*, 112214.
- [150] N. Füllbrunn, Z. Li, L. Jorde, C. P. Richter, R. Kurre, L. Langemeyer, C. Yu, C. Meyer, J. Enderlein, C. Ungermann, J. Piehler, C. You, *Elife*, **2021**, *10*, e62501.
- [151] G. P. Dunn, C. M. Koebel, R. D. Schreiber, *Nat. Rev. Immunol.*, **2006**, *6*, 11, 836.
- [152] C. Thomas, I. Moraga, D. Levin, P. O. Krutzik, Y. Podoplelova, A. Trejo, C. Lee, G. Yarden, S. E. Vleck, J. S. Glenn, G. P. Nolan, J. Piehler, G. Schreiber, K. C. Garcia, *Cell*, **2011**, *146*, 4, 621.
- [153] J. Piehler, G. Schreiber, *J. Mol. Biol.*, **1999**, *289*, 1, 57.
- [154] D. V. Kalvakolanu, E. C. Borden, in *Encyclopedia of Cancer*, Elsevier, **2002**, p. 511.

-
- [155] M. R. Capobianchi, E. Uleri, C. Caglioti, A. Dolei, *Cytokine Growth Factor Rev.*, **2015**, *26*, 2, 103.
- [156] E. Kwon, W. D. Heo, *Biochem. Biophys. Res. Com.*, **2020**, *527*, 2, 331.
- [157] R. A. Hallett, S. P. Zimmerman, H. Yumerefendi, J. E. Bear, B. Kuhlman, *ACS Synth. Biol.*, **2016**, *5*, 1, 53.
- [158] L. Wang, M. Tran, E. D'Este, J. Roberti, B. Koch, L. Xue, K. Johnsson, *Nat. Chem.*, **2020**, *12*, 2, 165.
- [159] J. Nong, K. Kang, Q. Shi, X. Zhu, Q. Tao, Y.-G. Chen, *J. Cell Biol.*, **2021**, *220*, 4, e202012112.
- [160] A.-S. Tseng, F. B. Engel, M. T. Keating, *Chem. Biol.*, **2006**, *13*, 9, 957.
- [161] A. Ghosh, A. Sharma, A. I. Chizhik, S. Isbaner, D. Ruhlandt, R. Tsukanov, I. Gregor, N. Karedla, J. Enderlein, *Nat. Photonics*, **2019**, *13*, 12, 860.
- [162] W. Kan, M. D. Enos, E. Korkmazhan, S. Muennich, D.-H. Chen, M. V. Gammons, M. Vasishtha, M. Bienz, A. R. Dunn, G. Skiniotis, W. I. Weis, *Elife*, **2020**, *9*, e55015.

7 Appendix

7.1 List of abbreviations

| | |
|---------------|---|
| μCP | Microcontact printing |
| ΔIC | Truncation of intracellular compartment |
| AB | Antibody |
| AFM | Atomic force microscopy |
| AJP | Aerosol jet printing |
| APC | Adenomatous polyposis coli |
| AR | Aspect ratio |
| ARGET | Activators regenerated by electron transfer |
| As | <i>Avena sativa</i> |
| ATRP | Atom transfer radical polymerization |
| Axin | Axis inhibition |
| BE | Binding energy |
| Bt | Biotin |
| CA | Contact angle |
| CIB1 | Calcium and integrin-binding |
| CK1 | Cryptochrome interaction basic helix-loop-helix |
| CMLE | Classic maximum likelihood estimation |
| COP1 | Constitutive photomorphogenic |
| CRD | Cysteine-rich domain |
| CRY2 | Cryptochrome |
| Cy5 | Cyanine 5 |
| DARPin | Designed ankyrin repeat proteins |
| DC | Destruction complex |
| DIC | Differential interference contrast |
| DNA | Deoxyribonucleic acid |
| DPN | Dip-pen nanolithography |
| dSTORM | direct stochastic optical reconstruction microscopy |
| Dvl | Dishevelled segment polarity protein |
| e.g. | For example |
| EDMA | Ethylene dimethacrylate |
| EDTA | Ethylenediaminetetraacetic acid |
| EtOH | Ethanol |
| FCS | Fetal cow serum |
| FFT | Fast Fourier transform |
| FIB | Focused ion beam |
| FMN | Flavin mononucleotide |
| Fps | Frames per second |
| FRAP | Fluorescence recovery after photobleaching |
| Fzd | Frizzled |

| | |
|--------------|---|
| GFP | Green fluorescent protein |
| GIET | Graphene induced energy transfer |
| GSK | Glycogen synthase kinase |
| HBS | Hepes buffered saline |
| HEMA | 2-hydroxyethyl methacrylate |
| HEPES | 2-[4-(2-hydroxyethyl)piperazin-1-yl]ethanesulfonic acid |
| HTL | HaloTag ligand |
| HTS | High-throughput screenings |
| ICD | Intracellular domain |
| IF | Immunofluorescence |
| iLID | Improved light induced dimer |
| IJP | Inkjet printing |
| IFNAR | Interferon alpha/beta receptor |
| IFN | Interferon |
| JAK | Janus kinase |
| LB | Lysogeny broth |
| LeF | Lymphoid enhancer-binding factor |
| LLPS | Liquid-liquid phase separation |
| LOV | light, oxygen and voltage domain |
| Lrp | low-density lipoprotein receptor-related protein |
| MALDI | Matrix-assisted laser desorption/ionization |
| MaP | Max-Planck |
| MAPK | Mitogen-activated protein kinase |
| mSi | Macroporous silicon |
| NGS | Next-generation surrogate |
| P2VP | Poly-2-vinylpyridine |
| PAF | Paraformaldehyde |
| PAS | Per-arnt-sim |
| PBS | Phosphate buffered saline |
| PCB | phycocyanobilin |
| PDMS | Poly(dimethoxysiloxane) |
| PEG | Poly(ethylene glycol) |
| PEI | Polyethylenimine |
| PES | Poly(ether sulfone) |
| PhyB | Phytochrome B |
| PIF | Phytochrome interaction factor |
| PLL | Poly(L-lysine) |
| PM | Plasma membrane |
| PPL | Polymer pen lithography |
| PS | Polystyrene |
| PSF | Point spread function |
| PVP | Poly(vinylpyrrolidone) |
| RGD | Arginine-Glycine-Aspartate |
| RIFS | Reflectance interference spectroscopy |

| | |
|----------------|--|
| RT | Room temperature |
| SAM | Self-assembled monolayer |
| SAV | Streptavidin |
| sDHB | Super-2,5-dihydroxybenzoic acid |
| SEM | Scanning electron microscope |
| SESI | secondary electron secondary ion |
| SiCPull | Single cell pull-down |
| SNR | Signal-to-noise ratio |
| SspB | Stringent starvation protein B |
| STAT | Signal transducers and activators of transcription |
| TCF | Transcription factor |
| td | tandem |
| TrCP | Transducin repeat-containing protein |
| TIRFM | Total internal reflection fluorescence microscopy |
| TMD | Trans-membrane domain |
| UVR8 | Ultraviolet resistance locus 8 |
| UV/VIS | Ultraviolet/visible |
| Wnt | Wingless-Int-1 |
| XPS | X-ray photoelectron spectroscopy |

7.2 Publication list

Parts of this work have been reported in the following references.

M. Philippi, Z. Li, M. Bhagawati, C. You, *Single Cell Pull-Down for Characterization of Protein Complexes*, in: T.S. Santra, F.-G. Tseng (Eds.), **Handbook of Single Cell Technologies**, Springer Singapore, Singapore, 2021, pp. 1–23.

Mercedes Runge, Hanna Hübner, Alexander Grimm, Gririraj Manoharan, René Wiczorek, Michael Philippi, Wolfgang Harneit, Carola Meyer, Dirk Enke, Markus Gallei, Martin Steinhart, *Capillary Stamping of Functional Materials: Parallel Additive Substrate Patterning without Ink Depletion*, **Adv. Mater. Interfaces**, 2021, 8, 2001911.

Michael Philippi, Changjiang You, Christian P. Richter, Mercedes Schmidt, Jannis Thien, Domenik Liße, Joachim Wollschläger, Jacob Piehler, Martin Steinhart, *Close-packed silane nanodot arrays by capillary nanostamping coupled with heterocyclic silane ring opening*, **RCS Advances**, 2019, 9, 43, 24742-24750.

Mercedes Schmidt, Michael Philippi, Maximilian Münzner, Johannes M. Stangl, René Wiczorek, Wolfgang Harneit, Klaus Müller-Buschbaum, Dirk Enke, Martin Steinhart, *Capillary Nanostamping with Spongy Mesoporous Silica Stamps*, **Adv. Funct. Mater.**, 2018, 28, 23, 1800700.

Weijia Han, Elzbieta Stepula, Michael Philippi, Sebastian Schluucker, Martin Steinhart, *Evaluation of 3D gold nanodendrite layers obtained by templated galvanic displacement reactions for SERS sensing and heterogeneous catalysis*, **Nanoscale**, 2018, 10, 44, 20671-20680.

Leiming Guo, Michael Philippi, Martin Steinhart, *Substrate Patterning Using Regular Macroporous Block Copolymer Monoliths as Sacrificial Templates and as Capillary Microstamps*, **Small**, 2018, 14, 34, 1801452.

Peilong Hou, Weijia Han, Michael Philippi, Helmut Schaefer, Martin Steinhart, *Nanostructured Submicron Block Copolymer Dots by Sacrificial Stamping: A Potential Preconcentration Platform for Locally Resolved Sensing, Chemistry, and Cellular Interactions*, **ACS Appl. Nano Mater.**, 2018, 1, 3, 1413-1419.

7.3 Curriculum vitae

- 03/2017 – 06/2021 **University of Osnabrueck**
Institute for chemistry of new materials
Doctoral thesis: Capillary stamping for bioanalytics and cell signaling
- 11/2013 – 11/2015 **University of Ulm**
Institute of macromolecular chemistry
Master thesis: Energy transfer in c_3 -symmetrical low molecular gelator as light harvesting complexes
Received Degree: **M.Sc.**
- 10/2010 – 11/2013 **University of Ulm**
Institute of macromolecular chemistry
Bachelor thesis: Synthesis of spin labeled amino acids and peptides
Received Degree: **B.Sc.**
- 09/2000 – 06/2009 **Illertal-Gymnasium Voehringen**
Received Degree: **General matriculation standard**

7.4 Declaration

I hereby declare that the presented thesis

Capillary stamping for bioanalytics and spatial manipulation of protein-protein interactions in live cells

was prepared entirely on my own. Outside sources were not used without an explicit declaration in the text. The following person attributed to this work as a collaboration partner or a student under my supervision:

- Andreas Stark conducted the TIRF-RfS experiments for the BSA adsorption on differently silanized glass substrates.
- Christian P. Richter provided the MatLab program used in the colocalization analysis of the Wnt signaling relevant proteins.
- Jannis Thien conducted the XPS measurements.
- Dr. Michael Holtmannspötter conducted the dSTORM experiments.
- Dr. Stefan Walter conducted the MALDI experiments.

I have not attempted a promotion before, and this work was not presented to any other institution before.

Osnabrück (19.6.2021)

Michael Philippi